THE EFFECT IN STRAIN PATH ON MECHANICAL BEHAVIOUR OF AN Al-Cu ALLOY

THE EFFECT OF A CHANGE IN STRAIN PATH ON THE MECHANICAL BEHAVIOUR OF AN Al-Cu ALLOY

BY

NICOLE DE WITT MARTIN, B.A.Sc.

A Thesis

Submitted to the School of Graduate Studies

in Partial Fulfilment of the Requirements

for the Degree

Master of Science ENGINEERING

McMaster University

September 1982

MASTER OF SCIENCE (1982) ENGINEERING
(Metallurgy)

McMASTER UNIVERSITY
Hamilton, Ontario

TITLE: The Effect of a Change in Strain Path on the Mechanical Behaviour of an Al-Cu Alloy

AUTHOR: Nicole De Witt Martin, B.A.Sc. (University of Toronto)

SUPERVISOR: Professor J.D. Embury

NUMBER OF PAGES: xiv, 152

ABSTRACT

The primary objective of the present study was to examine the effect of a 90° change in strain path, on the mechanical behaviour of an alloy, and its relation to the microstructure. In order to achieve this, the mechanical behaviour in uniaxial tension and compression of three different heat treatments of an Al 3.6 wt% Cu alloy and of pure aluminum were investigated. The heat treatments include a solid solution, a peak aged and an overaged condition. The results show a large 'Bauschinger' type effect in the overaged Al-Cu after 15% prestrain.

The differences in mechanical behaviour in the materials studied were rationalized with the aid of transmission electron microscopy observations, and work hardening models from the literature. A simple model which relates the work hardening behaviour to a measurable microstructural feature viz the initial obstacle spacing, is presented and compared with the experimental data.

The fracture behaviour of each of the materials was also observed. The results are documented in a generalized form of a plane stress map, and discussed in terms of the movement of the material's yield surface in stress space as it work hardens. The potential use of this type of map for

representing ductile fracture processes as well as intergranular surfaces (for a wide range of stress states) is discussed.

ACKNOWLEDGMENTS

First and foremost, I thank my husband Michael for his daily support and encouragement.

I would like to thank David Embury for his guidance, advice and especially his patience. Also I must thank the Metallurgy Department as a whole for offering Canadian students the oppurtunity to work with fellow students and scientists from all over the world.

Finally, I would like to acknowledge the financial support of Stelco Inc. for two years in the form of a Stelco Fellowship.

TABLE OF CONTENTS

		Page
ABSTRACT		iii
ACKNOWLEDGMENTS		v
TABLE OF CONTENTS		vi
LIST OF SYMBOLS		viii
LIST OF FIGURES		xi
LIST OF TABLES		xiv
CHAPTER 1:	INTRODUCTION	1
CHAPTER 2:	LITERATURE REVIEW	6
2.1	Al-Cu Precipitation Sequence	6
2.2	Forms of the Bauschinger Effect	8
2.3	Plasticity	13
2.4	Fracture	19
2.4.1	Fracture Maps	20
2.4.2	Ductile Fracture	22
2.4.3	Shear Failure	27
2.4.4	Intergranular Fracture	30
CHAPTER 3:	EXPERIMENTAL PROCEDURE	46
3.1	Material	46
3.2	Mechanical Testing	48
3.3	Metallography	53
3.4	Scanning Electron Microscopy	54
3.5	Transmission Electron Microscopy	55
3.6	Computer Work	56

		Page
CHAPTER 4:	RESULTS	
	4.1 Basic Mechanical Properties	63
	4.2 Work Hardening Characteristics	64
	4.3 Change in Strain Path	66
	4.4 Fracture	69
	4.5 Microscopy	71
SUMMARY OF RESULTS		77
CHAPTER 5:	DISCUSSION	105
	5.1 Monotonic Loading Behaviour	105
	5.2 Subsequent Yield Surfaces	123
	5.3 Fracture Characteristics	125
	5.4 Fracture Maps	131
CHAPTER 6:	CONCLUSIONS	148
REFERENCES		150
APPENDIX A		A1

LIST OF SYMBOLS

α	strength parameter
β	arrangement factor
γ	shear strain
μ	shear modulus
λ	slip distance
ε	true strain
ε_A	true strain in the A direction
ε_B	true strain in the B direction
ε_f	true strain to fracture
σ	true stress
$\sigma_1, \sigma_2, \sigma_3$	principal stresses
σ_b	back stress defined in the text
$\sigma_b^{A:B}$	back stress measured in the B direction after prestrain in the A direction
$\sigma_b^{-A:-B}$	back stress measured in compressive B direction after compressive prestrain in the A direction
$\sigma_b^{-B:-C}$	back stress measured in compressive C direction after compressive prestrain in the A and B directions
$\sigma_b^{A:-A}$	back stress measured from a tension - compression test
σ_f	true fracture stress
σ_o	initial flow stress
σ_s	saturation stress (defined in text)
σ_y	yield stress
ν	Poisson's ratio

LIST OF SYMBOLS (cont.)

ρ	dislocation density
ρ^S	statistically stored dislocation density
ρ^G	geometrically necessary dislocation density
θ, $\frac{\partial\sigma}{\partial\varepsilon}$	instantaneous work hardening rate
A	cross sectional area of a specimen
A_o	initial cross sectional area of a specimen
a	minimum radius of a tensile specimen
b	Burger's vector
D	initial obstacle spacing
D_i	damage function
E	Young's modulus
I	moment of inertia
K	strength coefficient
l	particle size; $CuAl_2$ plates
L_R	dislocation line length removed per recovery event
P	pressure
R	radius of curvature at the neck of a tensile specimen
r_o	initial particle radius: $2r_o = l$ is assumed for the present study
n	strain hardening exponent
S_i	structure parameter

LIST OF SYMBOLS (cont.)

t	time
V_f	volume fraction of precipitates

LIST OF FIGURES

		Page
FIGURE 2.1	Al-Cu Phase Diagram	37
FIGURE 2.2	Initial Work Hardening Rate versus Ageing Time	38
FIGURE 2.3	The Bauschinger Effect	39
FIGURE 2.4	The Bauschinger Effect in Al 4 wt% Cu	40
FIGURE 2.5	Magnitude of Back Stress versus Permanent Softening	41
FIGURE 2.6	Definitions of Terms Used in Equation [2.18]	42
FIGURE 2.7	Schematic Example of an Axisymmetric Fracture Map	43
FIGURE 2.8	Intergranular Fracture	44
FIGURE 2.9	Intergranular Fracture	44
FIGURE 2.10	Mechanism of Grain Boundary Crack Initiation	45
FIGURE 3.1	Test Specimen Dimensions	57
FIGURE 3.2	Definition of Yield Stress	58
FIGURE 3.3	$\frac{a}{R}$ versus $\log_e \frac{A_o}{A}$	59
FIGURE 3.4	Typical Silhouette of Pure Aluminum Neck During a Tensile Test	60
FIGURE 3.5	Comparison of Different Compression Testing Procedures	61
FIGURE 3.6	Two Stage Tensile Test: Stage I	61
FIGURE 3.7	Two Stage Tensile Test: Stage II	62

LIST OF FIGURES (cont.)

		Page
FIGURE 4.1	Tensile Stress versus Strain Curves	79
FIGURE 4.2	Comparison of Results in Tension and Compression	80
FIGURE 4.3	Work Hardening Rate versus Strain	81
FIGURE 4.4	Work Hardening Rate versus Stress	83
FIGURE 4.5	Stress versus Strain: Aluminum	85
FIGURE 4.6	Stress versus Strain: Al 3.6% Cu Solid Solution	86
FIGURE 4.7	Stress versus Strain: Al 3.6% Cu Peak Aged	87
FIGURE 4.8	Stress versus Strain: Al 3.6% Cu Over Aged	88
FIGURE 4.9	Fracture Surface: Aluminum	89
FIGURE 4.10	Fracture Surface: Solid Solution	90
FIGURE 4.11	Fracture Surface: Peak Aged	91
FIGURE 4.12	Fracture Surface: Over Aged	92
FIGURE 4.23	Pure Aluminum: $\varepsilon_A = 0.38$	93
FIGURE 4.25	Pure Aluminum: $\varepsilon_A = 0.45$	93
FIGURE 4.26	Pure Aluminum: $\varepsilon_A = 0.45$ plus $\varepsilon_B = 0.45$	94
FIGURE 4.35	Al-Cu Solid Solution: $\varepsilon_A = 0.45$	95
FIGURE 4.36	Al-Cu Solid Solution: $\varepsilon_A = 0.45$ plus $\varepsilon_B = 0.45$	95
FIGURE 4.41	Peak Aged Al-Cu: Prior to Deformation	96
FIGURE 4.43	Peak Aged Al-Cu: $\varepsilon_A = 0.38$	97
FIGURE 4.45	Peak Aged Al-Cu: $\varepsilon_A = 0.45$	98
FIGURE 4.46	Peak Aged Al-Cu: $\varepsilon_A = 0.45$ plus $\varepsilon_B = 0.45$	98

LIST OF FIGURES (cont.)

		Page
FIGURE 4.51	Over Aged Al-Cu: Prior to Deformation	99
FIGURE 4.52	Over Aged Al-Cu: $\varepsilon_A = 0.18$	100
FIGURE 4.54	Over Aged Al-Cu: $\varepsilon_A = 0.54$	101
FIGURE 4.55	Over Aged Al-Cu: $\varepsilon_A = 0.45$	102
FIGURE 4.56	Over Aged Al-Cu: $\varepsilon_A = 0.45$ plus $\varepsilon_B = 0.45$	103
FIGURE 4.60	Over Aged Al-Cu	104
FIGURE 5.1	Yield Surface Movement: Aluminum	136
FIGURE 5.2	Yield Surface Movement: Al-Cu Solid Solution	137
FIGURE 5.3	Yield Surface Movement: Peak Aged Al-Cu	138
FIGURE 5.4	Yield Surface Movement: Over Aged Al-Cu	139
FIGURE 5.5	Fracture Profile of Al-Cu Solid Solution Solution	140
FIGURE 5.6	Fracutre Profile of Peak Aged Al-Cu	141
FIGURE 5.7	Central Cross Section of the Fractured Peak Aged Al-Cu	142
FIGURE 5.8	Fracture Profile of Over Aged Al-Cu	143
FIGURE 5.9	Fracture Surface of Peak Aged Al-Cu: Two Stage Tensile Test	144
FIGURE 5.10	Microcracks in Compressed Peak Aged Al-Cu	145
FIGURE 5.11	The Effect of Grain Size on the Fracture Surface of an Al-Mg-Si Alloy	146

LIST OF TABLES

		Page
TABLE 2.1	Typical Strains to Fracture	23
TABLE 2.2	Typical Fracture Stresses of Several Aluminum Alloys	32
TABLE 3.1	Heat Treatments	48
TABLE 4.1	Material Tensile Properties	64
TABLE 4.2	Compressive Yield and 'Back' Stresses	67
TABLE 4.3	'Back' Stress Values for the Bauschinger Effect and for the Present Study	68
TABLE 4.4	'Back' Stress Values from Two Stage Tensile Tests	69
TABLE 4.5	Fracture Data	70
TABLE 4.6	Micrograph Figures	72
TABLE 4.7	Summary of Results	77
TABLE 4.8	Summary of Results	77
TABLE 5.1	σ_s Values	117
TABLE 5.2	Fracture Stress Variation with Grain Size	134

CHAPTER 1

INTRODUCTION

During the past thirty years an excellent basic understanding of the relationships between the structural and mechanical properties of metals and their alloys has been developed. This has proved useful for improving the efficiency of alloy design. From a knowledge of grain size, particle size, and volume fraction of particles, an approximate calculation of the yield stress of an alloy can be made. However for the practical utilization of complex materials it is not only properties such as the yield stress which are of importance but also the less well understood features of plasticity, such as the large strain behaviour and fracture.

During service, varying amounts of plastic strain, imposed in one or more directions at various temperatures and frequencies, will be sustained by the material and may cause fracture. Thus, the mode of fracture and the likely criteria for fracture also influence the choice of material. The processes of both work hardening due to plastic flow and fracture, and the dependence of these processes on microstructure are much more difficult to model from first principles than the initial yield stress.

In an effort to classify the mechanical behaviour of metals, a large number of parameters have been utilized. Parameters such as yield stress, fracture stress, true strain to fracture or ductility, toughness and hardness are often specified as a basis for the comparison of materials. Elastic properties such as Young's modulus are related solely to the bonding properties of the material. In contrast, the plastic properties of materials are more difficult to elucidate. The difference between elastic and plastic deformation is that plastic flow results in permanent, rather than reversible, changes in the material's dimensions. The yield stress of a material serves to separate purely elastic and elastic-plastic behaviour. It is at this critical stress that large numbers of dislocations become mobile, resulting in general yielding. As the material work hardens, the dislocations multiply and interact. Plastic properties and fracture processes depend on the stress state and the strain history of the material. These dependences can be ascribed, on a structural level, to

- the movement of the dislocations within the material
- the results of local interactions of dislocations with particles and grain boundaries
- the accumulation of dislocations
- the accumulation of microstructural damage in the material.

To model the material, its work hardening, and subsequent fracture, it is necessary to relate the local stresses and strains to idealized dislocation configurations and local events such as decohesion.

Because of its complexity, the traditional approach to the study of large strain plasticity has been empirical rather than based on detailed physical models. An example of this empirical approach would be the construction of a yield surface to describe the transition from elastic to plastic behaviour. The value of this approach is that the yield surface for all stress states is derived from a mathematical formalism related simply to data derived in uniaxial tension. From an empirical basis, once the yield surface is established, strain hardening can be described by the subsequent changes in the position of the yield surface. Since the hardening is not sufficiently well understood for a generalized hardening rule to be formulated, several hardening theories have been proposed. For instance, the theories may involve the expansion, change in shape, or translation of the yield surface. However this empirical approach does not relate to the actual mechanisms or microstructural processes of deformation which are involved.

To understand, rather than simply describe, the complex processes of plastic flow it is necessary to understand the physical mechanisms underlying the empirical

phenomena. Physical models must be developed which describe processes at the microstructural or atomistic level and which in turn, can be related to the various macroscopic empirical models. These physical models should predict behaviour for a variety of stress states and strain histories. The current work will focus on one segment of this larger problem, namely to examine the effect of changes in strain path on the mechanical response of several materials.

To minimize the complexity of the study a simple, well characterized system has been chosen. The influence of strain path on a single phase material, pure aluminum, is compared with that observed for an aluminum copper alloy.

Several ageing conditions for the alloy have been considered: a solid solution; a matrix-soft particle system; and a matrix-hard particle system. The soft particles will be sheared by the dislocations during plastic flow. The hard particles behave as elastic rigid inclusions in a plastic matrix. The microstructural differences between the four materials were found to reflect marked changes in the influence of strain path changes during plastic flow. Fracture behaviour as a function of heat treatment was studied in order to determine which empirical criteria might be used to predict failure modes.

In order to better understand the effects of strain path two approaches were considered. Materials were plasti-

cally deformed to large tensile and compressive strains in order to document the monotonic plastic response. The effect of the deformation on the internal structure was observed by transmission electron microscopy. In addition, samples were deformed in a sequence of three mutually perpendicular directions to determine the influence of strain path. A simple diagram was formulated to illustrate the competition between fracture and plastic flow and how changes in strain path influence this competition. It is hoped that the results of this study will further the understanding of the physical mechanisms underlying plastic flow and fracture. The results do not represent a complete treatment of the influence of strain path but do provide a basis for further work using more complex stress states relevant to the technological applications of materials.

CHAPTER 2

LITERATURE REVIEW

Due to the scope of this thesis it is necessary to limit the extent of the literature review and, where possible, to indicate major reviews already available in the literature. For the sake of clarity, this chapter has been separated into the following four sections; Al-Cu Precipitation Sequence, Forms of the Bauschinger Effect, Plasticity and finally Fracture.

2.1 Al-Cu Precipitation Sequence

This study is concerned with how the presence or absence of obstacles in a material affects its mechanical properties. Therefore, a brief description of the precipitates, which form in Al-Cu is given in this section. The Al rich section of the Al-Cu phase diagram is shown in Figure 2.1. The diagram includes both the metastable boundaries for the GPI and GPII zones, as well as the stable boundaries indicating the formation of the θ phase.

The precipitation sequence in Al-Cu alloys is well established. Several reviews of this subject have been written (Kelly and Nicholson, 1963 and Lorimer, 1961).The sequence was first studied by Guinier and Preston independently (Guinier,

1938, Preston, 1938). Since then their work has been confirmed and extended. The sequence is as follows:

GPI zones	metastable phases
GPII zones or θ"	
θ'	
θ	stable phase

GPI zones are plate-like in shape and form on the {100} planes of the aluminum matrix. The plates are only a few atomic planes thick. The GPII zones (Guinier, 1942) are coherent precipitates of $CuAl_2$. These zones are an ordered tetragonal arrangement of Al and Cu, five planes thick, forming a $CuAl_2$ plate. The habit plane of the GPII zones is $\{100\}_{Al}$, similar to the GPI zones.

It is agreed that the θ' precipitates have a tetragonal unit cell (Silcock et al, 1954). Silcock et al have measured the lattice parameters and obtained similar results to Guinier; a = 4.04 Å and c = 5.8 Å. The axes of the unit cell are parallel to the $\langle 100 \rangle_{Al}$ directions.

The θ structure is similar to the θ', both have a tetragonal unit cell. The θ phase lattice parameters are different to those of θ', a = 6.066 Å and c = 4.874 Å. (Silcock et al, 1953).

Two or more of the above structures may be present in the matrix at once, depending on the ageing treatment. A description of the ageing schedules followed in this study and the resulting microstructures is given in a later

chapter.

The influence of second phase particles on the mechanical properties can be summarized as follows. Figure 2.2 shows the relationship of the initial work hardening rate to ageing time for a typical Al-Cu alloy (Kelly and Nicholson, 1963). The particles may be sheared as the material is deformed (the left part of the curve). In the case of the overaged material (the right section of the curve in Figure 2.2) the particles play a direct load bearing role as elastic inclusions in a plastic matrix. This gives rise to the Bauschinger effect, and other forms of anisotropy that are the subject of the present study.

2.2 Forms of the Bauschinger Effect

The Bauschinger effect is generally defined as the process of plastic deformation in a given direction causing a loss of strength upon reversal of the direction of deformation. The effect is illustrated schematically in Figure 2.3 which shows a stress strain hysteresis loop for tension and compression.

The reverse deformation can be considered in terms of the magnitude of reverse strain required to reach the final forward flow stress. It can also be described in terms of the stress at which reverse yielding, as compared

to yielding in the forward direction, occurs. Though both these methods are used, for the purpose of the present study the Bauschinger effect and related anisotropies will be measured in terms of stress parameters.

There is no unique stress parameter to describe the Bauschinger effect. Depending on the experimental method used, different parameters can be generated. In order to facilitate the comparison of the data from the present study with those in the literature, the method due to Moan (1977) was followed. Moan used the following definition of back stress σ_b (equation [2.1]) to classify his results.

$$\sigma_b = \frac{1}{2}(\sigma_{final}^{forward} - \sigma_y^{reverse}) \qquad [2.1]$$

To quantify the back stress in terms of prior strain, equation [2.2] was used

$$\frac{\sigma_b}{\%\ \text{work hardening}} = \frac{1}{2}\left(\frac{\sigma_{final}^{forward} - \sigma_y^{reverse}}{\sigma_{final}^{forward} - \sigma_y^{forward}}\right) \qquad [2.2]$$

Since this study is concerned with differences in flow stress in the A and B directions (90° apart), "forward" has been replaced by "A", and "reverse" by "B". Since the material exhibits continuous yielding, the yield stress has been defined as the proof stress at ε = .002. As is evident from Figure 2.3 there are two major differences between the

continued curve in the forward direction, and the curve in the reverse direction. The initial drop in yield upon strain reversal is the most striking feature. The reverse yield stress is not as well defined as it is in the foward direction. The stress strain curve appears more rounded in the reverse direction. This is termed transient softening. This region of transient softening is said to increase with increasing prestrain (Washburn and Murty, 1965). As strain increases the reverse stress strain curve becomes parallel to the forward direction curve. The difference in their flow stress levels is termed permanent softening. This distinction was made by Orowan (1959). Since the imposition of a recovery anneal will tend to remove the permament softening, Orowan attributed it to long range internal stresses i.e. elastic stress supported by some form of obstacle in the material. The transient softening is due simply to the fact that the dislocation moving forward confronts a harder array of obstacles than it does immediately after strain reversal.

Many microstructural features affect the Bauschinger effect. The presence of solute atoms, of precipitates, the type of precipitate, the crystal structure of the metal or the texture of the material, all change the characteristics of the hysteresis loop. The value of $\frac{\sigma_b}{\%wk\ hdg}$ is much larger for a material containing hard precipitates,

such as overaged Al-Cu, than either the solid solution or the pure metal matrix, (Moan, 1977)(Wilson, 1965).

In his study of reversible work hardening in alloys of cubic metals, Wilson (1965) measured the Bauschinger effect in Al 4% Cu. Figure 2.4 summarizes his results. The peak aged Al-Cu shows little decrease in flow stress upon strain path reversal, whereas the overaged material shows a very large decrease in flow stress. Wilson then went on to estimate the back stress from measurements of lattice strains in the matrix. Figure 2.5 shows that the magnitude of the back stress is proportional to the amount of permanent softening.

External parameters also affect the Bauschinger effect; an increase in test temperature will, in general, decrease the extent of the Bauschinger effect; and an increase in the amount of prestrain in the forward direction will increase the Bauschinger effect.

In the present study most of these parameters are held constant. The experiments were performed at room temperature. The prestrain in the A direction was 15% for each material. The only microstructural differences were due to the ageing treatments of the Al-3.6%Cu. The material has been examined in three different conditions; solid solution, a soft metal matrix containing small θ' precipitates, and the same metal matrix containing large, hard θ

precipitates.

The Bauschinger effect arises due to the presence of elastic back stresses, which aid the reverse flow, or flow in a newly imposed strain path. Hence, in the current work two methods of characterizing the elastic back stresses were used; the magnitude of σ_b which was measured by a change in strain path, and the local configuration at the hard θ particles in the overaged material. These local configurations, accummulated dislocations or lattice bending in the θ, reflect the fact that the elastic back stress must be supported by some form of obstacle such as second phase particles, cell walls or grain boundaries in order to contribute to the Bauschinger effect.

In order to discuss plasticity at large strains, it is necessary to consider three simultaneous processes. These three processes are work hardening, recovery, and the damage accumulation processes in the matrix. Damage accumulation, such as the nucleation and growth of voids, will in general, only occur at large strains. The plastic behaviour of metals at low strains has been reviewed previously. A brief outline of the constitutive equations available in the literature describing plastic behaviour at low and high strains, follows in the next section.

2.3 Plasticity

Plastic deformation causes a permanent shape change of the material. The volume (or density) of the material remains essentially constant even after very large amounts of plastic deformation. Only if there is a large number of voids or some other form of microstructural damage developed in the sample will there be a change in density. Such changes would be most significant near the fracture condition in the case of a tensile test.

The yield strength of a material marks the onset of general plastic deformation. It is therefore of use to be able to predict the yielding of a material for complex loading conditions, when choosing a specific material for use in industry. It is generally accepted that the yield strength of a material can be increased by alloying and heat treatment techniques. The presence of obstacles to dislocation movement, such as $CuAl_2$, precipitates, in a matrix will increase the yield stress. The simplest description of this strengthening effect is (Orowan, 1954),

$$\tau = \frac{\mu}{b\ell} \qquad [2.3]$$

where b is the burgers vector, ℓ is the obstacle spacing along the dislocation line, and μ is the shear modulus. This will give only an approximate value of the flow stress, since in a real material the obstacles are not evenly dis-

tributed and homogeneous in size. Equation [2.3] can be improved to give a predicted value of yield stress, within two times the experimental value (Kocks, 1977). This is done by taking into account; variations of ℓ, differences in particle size, interactions between dislocations, and direction of dislocation movement. However, in many cases the material is used, not in tension, but a far more complex stress state.

The yield strength for simple stress states can be measured experimentally. The tensile data is available for commercial alloys. However, the material will often have a strain history which may or may not affect its yield strength. The yield strength, for the more complex stress state, can be estimated empirically using a yield criterion.

Several criteria have been proposed which express the yield strength of a material, with regard to strain history, in more complex multiaxial stress states. These criteria can be expressed in terms of principal stresses. An example of this type of criterion, the von Mises yield criterion, is used in this study [2.4].

$$(\sigma_1-\sigma_2)^2 + (\sigma_2 -\sigma_3)^2 + (\sigma_3-\sigma_1)^2 = 2\sigma_y^2 \qquad [2.4]$$

This criterion is equivalent to assuming that yielding occurs when the shear strain energy reaches some critical value.

It is also of interest to be able to predict the

plastic behaviour after yielding. There are two approaches to this problem, a microstructural approach and a continuum approach. Examples of the continuum approach are described here.

Many constitutive laws have been proposed to describe the stress strain curve in the region of plasticity. The simplest are:

$$\sigma = K \varepsilon^{n} \qquad [2.5a]$$

$$\sigma = \sigma_0 + K \varepsilon^{n} \qquad [2.5b]$$

where K is a strength coefficient and n is a strain hardening exponent. This type of equation will fit the data in many cases, but only over a limited strain range.

Attempts to improve the capabilities of equations such as [2.5] have been made. Much work has been done, using computation and detailed tensile data, to improve the utility of this type of equation. One or more work hardening terms may be added to the equation to account for the material's behaviour.

Another, more versatile, example of this type of equation is one developed by Lloyd and Sang (1977),

$$\sigma = \sigma_s - (\sigma_s - \sigma_0)\exp[N\varepsilon^{P}] \qquad [2.6]$$

where σ is the flow stress at a strain ε, σ_0 is the yield stress, σ_s is the maximum stress that can be achieved and

N and P are constants. Data at low strains can be extrapolated to predict behaviour at higher strains with acceptable accuracy (Lloyd and Kenny, 1980). The equation represents well the alloys studied by Lloyd and Kenny, including a variety of heat treatable and non-heat treatable aluminum alloys.

This type of analysis gives an equation and constants valid for only a specific material under unique test conditions. The constants do not relate simply to the actual microstructural features of the material. The constitutive equation becomes far more complex if one attempts to describe directionality effects, such as the Bauschinger effect, or to predict failure.

In order to predict the behaviour of a material with a complex strain history, at strains approaching fracture as well as at low strains, it may be important to describe plastic flow in terms of both work hardening and of damage accumulation. Such an analysis is described next.

To describe the plastic deformation of a material we can, following Ashby (1982), begin with equations [2.7] and [2.8].

$$\frac{\partial \varepsilon}{\partial t} = f(\bar{\sigma}, T, S_i) \qquad [2.7]$$

$$\frac{\partial S_i}{\partial t} = g(\bar{\sigma}, T, S_i) \qquad [2.8]$$

S_i represents some structural aspect of the material such

as grain size or dislocation density. If during deformation there is no change in the structure $S_i = S_i$, one can assume the steady state condition; $\frac{\partial S_i}{dt} = 0$. Combining this with equations [2.7], [2.8] one obtains an expression for the strain rate as a function of $\bar{\sigma}$, and T for each mechanism i. An example of this type of equation is

$$\dot{\varepsilon} = \dot{\varepsilon}_o \left(\frac{\bar{\sigma}}{\sigma_o}\right)^n : \dot{\varepsilon}_o = A \exp\left[-\frac{Q}{RT}\right] \qquad [2.9]$$

which describes power law creep at high temperatures. A logical extension of this analysis is to add the function

$$\frac{dD_i}{dt} = h(\bar{\sigma}, \sigma_n, P, T, S_i, D_i) \qquad [2.10]$$

where D_i represents some type of damage accumulated in the material. This damage may be an increase in crack length, or in the areal fraction of voids. Again, assuming $\frac{dS_i}{dt} = 0$ and combining equations [2.7] and [2.8] and [2.10] one is left with:

$$\dot{\bar{\varepsilon}} = f(\bar{\sigma}, T, D_i) \qquad [2.11]$$

$$\dot{D}_i = h(\bar{\sigma}, \sigma_n, P, T, D_i) \qquad [2.12]$$

By integration of [2.11] and [2.12],

$$t_{failure} = \int_{D=0}^{D=D_f} \frac{dD}{h(\bar{\sigma},\sigma_n,P,T,D_i)} \qquad [2.13]$$

$$\varepsilon_{failure} = \int_{t=0}^{t=t_f} \frac{d\varepsilon}{f(\bar{\sigma},T,D_i)} \qquad [2.14]$$

one can determine the strain to failure. The more damage terms, D_i, included in this process the better the final value of ε_f will be. It is practical to use this analysis for each definitive mechanism independently, however the solution becomes a more complex if several S_i and D_i terms are considered simultaneously. This set of equations could be a powerful tool in determining the amount of damage accumulated, but it does not describe the distribution of damage, which may be of major significance when attempting to predict $\varepsilon_{failure}$ in commercial materials.

It is clear that including terms to describe processes such as damage accumulation in the constitutive equation describing plastic deformation, increases its complexity. In taking this approach each stage of the deformation process may be treated separately. Material behaviour is studied by considering geometrical representations of some of the events involved in flow and fracture. Directional differences in material properties, due to prior plastic deformation, are one of the major concerns of the present study. The initial yield surface and the yield surface subsequent to deformation are considered.

Having reviewed the formal descriptions of damage accumulation available, it is useful to consider criteria for various fracture modes. Fracture terminates plastic flow due to the deterioration of the metal matrix, indicated

by a decrease in the work hardening rate, to the accumulation of damage, or to a specific local event which nucleates fracture. The understanding of fracture processes is further complicated by the existence of various different failure modes, which may act separately or in parellel. These different fracture modes are described briefly in the next section.

2.4 Fracture

One important result of increasing the flow stress of materials is that, in general, the ductility decreases and a broad variety of fracture modes becomes possible. These fracture modes, can be considered in two ways. The first is to consider those modes which result from changes in the global properties of the material. An example is the occurrence of a decrease in work hardening rate combined with the onset of negative strain rate sensitivity, which may result in the occurrence of localized shear fracture.

The second category to consider is fracture modes of a more heterogeneous nature. These modes involve a nucleation step, which depends on a local event such as, the formation of a microcrack at a grain boundary, or decohesion at the interface of a second phase particle. Nucleation is followed by the propagation of a local fracture mode or the coalescence of microstructural damage.

Clearly, these two modes cannot be treated separately because both may contribute to the overall fracture process in complex events such as ductile fracture. However, this classification is still useful in the context of developing simplified criteria on which to base models of fracture processes.

For clarity, we can divide the fracture processes into the following categories for Al alloys:

(i) ductile fracture, in which voids initiate at second phase particles, grow and coalesce,

(ii) localized shear failure,

(iii) intergranular fracture.

These processes are reviewed in the various subsections which follow.

It must also be remembered that the controlling physical processes are dependent on both temperature and stress state. In an attempt to generalize the fracture processes and illustrate the range of test conditions over which they apply, a variety of fracture maps have been developed. Several of these types of maps are described briefly in the next section. Details of the theory and calculations used to construct the yield surfaces and fracture maps in the present study are given in Appendix A.

2.4.1 Fracture Maps

One type of map, developed by Ashby and Embury (1981),

illustrates brittle fracture surfaces in plane stress and in axisymmetry. The coordinates σ_1, σ_2 or σ_3 are the three principal stresses. The yield surface for the material in question can be drawn on the same map. In this way it can be compared to the surface representing fracture. If, as the material work hardens, the yield surface remains within the brittle fracture surface, failure is avoided. If enough data is collected, or a reliable quantitative model of work hardening processes is developed, the construction of these maps would be very useful for determining the fracture modes relevant to metal forming processes.

Another type of map is that used by Embury and Nes (1974), where fracture stress is plotted as a function of temperature. Each mode of failure, such as shear or grain boundary failure, has its own region on the map. The material is unique, and parameters, other than temperature, are not included. For instance, the boundaries of each region will shift, depending on the magnitude of the hydrostatic pressure and the differences in structural aspects of the material, such as grain size. The map serves as a pictorial representation and cannot, at this time, be used to predict failure modes.

A more general form of failure map was put forward by Ashby and his co-workers (1965, 1979). A normalized tensile stress is plotted against homologous temperature.

The stress used is not the fracture stress, but the critical stress at which the onset of various fracture mechanisms occurs. There are several variations of this type of map for which critical values of different parameters are used. This type of map was presented for Aluminum by Ashby, Gandhi and Taplin (1979) using experimental data. Contour lines of constant time to fracture can be superimposed onto the map. Until a map can be constructed using constitutive equations to describe parameters such as strain to fracture, this type of map will not be useful in the predictive sense.

2.4.2 Ductile Fracture

The ductility of a material is usually measured in terms of natural strain at fracture or percent reduction in area. These values are obtained from tension tests. Some typical values for several ductile materials are included in Table 2.1.

Ductile fracture can occur in two basic modes; a fibrous mode or a shear mode. Often a ductile fracture will exhibit both modes in a single fracture. Two such examples are, the well known cup and cone fracture of some materials in tension, and the surface of a ductile Charpy impact test piece. In both instances there is a central area which fails in the fibrous mode, and outer edges (shear lips) which have failed at a 35° angle to the stress axis by shear.

TABLE 2.1 Typical Strains to Fracture

Material	Strain to Fracture (true)	Reference
Copper 99.965% pure (.02 mm grain size)	1.00	French & Weinrich (1975)
Steel 1015	1.40	LeRoy et al (1981)
Steel 1045	0.910	LeRoy et al (1981)
Al 99.999% pure	2.6	this study
Al 3.6% Cu solid solution	0.91	this study

The mechanism for failure in the fibrous mode is well established, as it is widely accepted that some type of voiding mechanism leads to this type of failure. Many models have been generated to describe this mechanism, most of them starting with the same basic premise. (Brown and Embury, (1973), Thomason, (1968), McClintock, (1968)).

A sequence of three processes is said to occur: void nucleation at a second phase particle, void growth, which is then followed by void linkage, resulting in failure.

The final fracture strain for a fracture such as this can be written as a sum of the three.

$$\varepsilon_n + \varepsilon_g + \varepsilon_l = \varepsilon_f \qquad [2.15]$$

ε_n is the imposed macroscopic strain prior to nucleation, ε_l is the strain which contributes to void growth, and ε_p is the strain imposed after linkage begins up until failure of the sample is complete. The relative value of ε_l to the others will be very small since void linkage is generally a catastrophic event. This equation makes the assumption that the events are sequential and thus that these strains are additive.

Nucleation requires that a critical stress be reached at the matrix particle interface. This is a local condition, dependent on many factors, including particle size, shape and distribution. It is therefore a very complex process to model unless the second phase is assumed to be homogeneously distributed throughout the matrix. To use equation [2.15] one must also assume that all voids are nucleated at a unique value of ε_n and not over a range of strains.

The nucleation strain, ε_n, has been estimated by LeRoy et al (1981) for a spheroidized steel to be 0.5 true strain. The large value, is due to the high interfacial strength between the carbides and the matrix. Values of nucleation strain as low as .02 (Speich, 1977) have been measured at coarse, primary particles in steel.

Growth of the voids is dependent on the strain rate and stress state. Most workers have restricted themselves to modelling the voids in simple tension. The earlier models ignore interaction between voids as they grow and assume that their growth is homogeneous.

Thomason (1968) developed a plane strain model for ductile fracture by internal necking between cavities. His model accounts for the effects of second phase particles, of hydrostatic pressure, and of a triaxial stress system. The theory is in reasonable agreement with data showing the effect of volume fraction of cavities on strain to fracture, in copper and some of its alloys.

McClintock (1968) considered how stress states more complex than simple tension affect void growth. He determined a ductile fracture criterion for a plastic material containing three mutually perpendicular sets of cylindrical holes (with elliptical cross sections of major axis a and minor axis b). The cylindrical axis is labelled z. The chosen axes a and b are parallel to the directions of the principal stresses, σ_a and σ_b. The holes are small (length 2b), so that their interactions are not of concern (separation of voids is equal to $\ell_b > 2b$).

$$\varepsilon^f = \frac{(1-n)\ln(\ell_b/2b^o)}{\sinh[(1-n)(\sigma_a+\sigma_b)/(\frac{2\bar{\sigma}}{\sqrt{3}})]} \qquad [2.16]$$

n is the work hardening exponent from the well known equation [2.5a]. For cases of high triaxiality the above equation predicts the strain to fracture within 15% of the experimental value (McClintock, 1968).

LeRoy et al (1980) proposed a model to predict ductile fracture. Several major assumptions are made. First, there is a unique value of ε_n at which all nucleation sites become operative. Secondly, each void nucleated is of the same initial size. The basic premise, mentioned earlier, that void nucleation and growth are sequential processes must also be assumed for simplicity. For each different stress state for which a relationship between hydrostatic stress and strain can be determined it is then possible to predict the shape and size of voids at any strain ε ($\varepsilon > \varepsilon_n$). The equations for void growth used are a modified version of the Rice and Tracey (1969) equations.

To more completely describe the entire ductile failure process, it must be remembered that nucleation and growth can, and do occur simultaneously. There are many processes and effects to be considered. However, as the understanding of ductile failure improves and computer models become more refined, more phenomena can be successfully included in the model.

2.4.3 Shear Failure

Shear failure occurs in many different types of material systems. For example, a pure copper or nickel single crystal, will fail in pure shear on the {111} planes. Shear rupture is another form of failure. Voids are formed within the material and then linkage occurs, and a crack is formed. This type of crack can grow normal to the axis of maximum tensile stress (normal rupture) or along the plane of maximum shear stress (shear rupture). Rupture occurs in structural materials such as cold extruded steel (Cockcroft, 1967), high strength steels (Tanaka and Spretnak, 1973) and spheroidized steel (French and Weinrich, 1979). Tanaka and Spretnak (1973) measured the shear stress in local sheared regions of specimens deformed in torsion. Several heat treatments of 4340 steel were observed and values of shear stress, τ_ℓ, measured between $\mu/20$ and $\mu/35$, where μ is the shear modulus.

Shear failure is a less well understood form of ductile fracture. It is, in some sense, analogous to the necking phenomenon since it is a form of nonhomogeneous deformation. This type of failure can be considered in several ways. A nucleation event of some sort occurs causing shear strain to be localized, which causes the specimen to shear along a well defined macroscopic plane. The nucleation event may be due to a local strain softening of the

material, or may occur when a critical value of θ/σ is reached. Another possibility is, one or more areas of localized shear may be nucleated within the material and subsequently link. The large strains present in those regions may then initiate the nucleation of some other mode of failure.

Gurson (1977) has modelled ductile failure using plasticity theory as follows. He considers the process in two separate steps, the first step in which the nucleation and growth of voids occur, the second in which deformation localizes in a band, resulting in fracture by void linkage, due to void growth or growth of the area(s) of shear. The occurrence of the shear instability can be represented by a bifurcation in the flow field, which occurs when certain critical conditions are met. The influence of hydrostatic stress on the nucleation of voids, which may well affect the occurence of shear, was also investigated.

An alternative approach to describing a shear failure event, is to consider it in terms of the incremental change in flow stress, $\partial\sigma$. The critical condition for shear strain localization, proposed by Chung et al (1977), is the occurrence of either a negative strain rate sensitivity or strain softening. This can be expressed mathematically in terms of local properties such as $\partial\sigma/\partial\varepsilon$:

$$\left(\frac{\partial\sigma}{\partial\varepsilon}\,\partial\varepsilon + \frac{\partial\sigma}{\partial\dot{\varepsilon}}\,\partial\dot{\varepsilon}\right) < 0 \qquad [2.17]$$

Since it is very difficult to measure or approximate, on a microscopic level, dynamic properties such as $\partial\sigma/\partial\varepsilon$ or $\partial\sigma/\partial\dot{\varepsilon}$, and follow their subsequent development in a localized region of a sample undergoing deformation, practical use of this equation is limited.

Asaro (1979) formulated a model, in accord with the kinematic scheme of Asaro and Rice (1977), of a ductile single crystal undergoing symmetric double slip in tension. The constitutive laws he developed led to the following expression for a critical value of θ/σ at which shear bands may form. Asaro found that according to his field equations a negative work hardening rate is not necessary for shear bands to form.

$$\left(\frac{\frac{\partial\sigma}{\partial\varepsilon}}{\sigma}\right)_{crit} = \frac{\cos 2\theta - \cos^2 2\theta/\cos 2\phi}{(1-q)\cos^2 2\theta/\cos^2 2\phi + (1+q)\sin^2 2\theta/\sin^2 2\phi} \qquad [2.18]$$

The terms used in equation [2.18] are defined in Figure (2.6).

For most purposes it is easiest to assume that shear failure is governed by either a shear stress or a shear strain criterion. This approach is particularly useful for simplifying the graphical representation of shear failure. The critical shear stress is used to define a boundary line showing the limit of other possible forms of fracture. This is clearly illustrated by the example shown in Figure 2.7. It should be noted that as the yield stress increases, the stress required to nucleate and grow

voids increases relative to the critical shear stress. This implies that failure by shear may occur before conditions are met for fibrous ductile fracture, in very high strength materials, and for specific stress states. This observation is in accord with the experimental results of Tanaka and Spretnak (1973).

2.4.4 Intergranular Fracture

It is difficult to state categorically the difference between brittle and ductile fractures. Ductile fractures are a result of intense localized plastic deformation as a crack propagates across the specimen. In contrast, very little plastic deformation occurs during the propagation of a brittle crack. The two extremes may be distinguished. However difficulties arise in the description and prediction of failures which occur in mixed modes.

Intergranular fracture is typified by a faceted fracture surface. The size of the facets, which are easily recognizable by their ability to reflect light, is directly related to the grain size of the material. Clean intergranular fractures of aluminum and its alloys at room temperature and higher are unusual. Al-Cu alloys fail more frequently in a mixed mode. An example of a mixed mode fracture which initially appears to be brittle is shown in Figure 2.8. The fracture surface exhibits areas of clean

brittle fracture along the grain boundary. Dispersed throughout the surface are areas which have failed in the fibrous ductile mode. To classify this type of mixed mode failure one can measure the relative surface areas of brittle fracture and ductile fracture.

Another type of mixed mode intergranular failure is shown in Figure 2.9. The crack path has followed the grain boundaries therefore the fracture is intergranular and, one might assume, brittle. However, upon examining the surface with the scanning electron microscope one observes dimples, relatively homogeneous in distribution, on the grain boundary surfaces. Therefore there has been some degree of localized plastic deformation. The dimples may have caused, or been the result of crack growth. This leads to two conclusions. First, the term "intergranular fracture" should only be used to describe the fracture path, not to classify the fracture as brittle or ductile. Second, using the volume integral of total plastic deformation for the entire sample to classify the nature of the fracture can be misleading. It is the local volume integral near the fracture which may be of significance in identifying the fracture mechanism. Some typical values of σ_f, the fracture stress, for various aluminum alloys, which failed intergranularly, are given in the table below. The grain size will also affect the fracture stress, and the fracture

mechanism. The wide range of values supports the view that the fracture path is not always a good indication of which fracture mechanism caused the failure.

TABLE 2.2 Typical Fracture Stresses of Several Al Alloys

Material	Fracture Stress	Reference
peak aged Al-Mg-Si .62% Mg .39% Si	245 MPa (50°C)	Evensen, Ryum and Embury (1975)
commercial Al-Zn-Mg 5.17% Zn 1.19% Mg T6 condition	226 MPa	Embury and Nes (1974)
Al- 3.6% Cu peak aged	408 MPa	this study (intergranular plus shear)
Al 7075 T6	604 MPa	LeRoy and Embury (1977) report #115
Al 3.9% Cu superpure 4 days at 165°C	364 MPa	Ryder and Smale (1963)

The preceding section is a brief description of the physical characteristics and the classification of intergranular fracture, not the actual failure mechanism. Two conditions must be satisfied for intergranular failure to occur. In tension, the local tensile stress at the grain boundary must be greater than the grain boundary cohesive force, σ_{crit}. The second condition is that microcracks, once formed at the grain boundary, are able to grow along the grain boundary. The presence of grain boundary precipitates plays a major role in satisfying these two conditions.

Microcracks may form at the grain boundary by several different mechanisms. Zener (1947) proposed that if a grain boundary was subjected to the appropriate shear stress, a wedge shaped microcrack would form at the edge of the boundary. The stress concentration to form this type of crack must exceed the grain boundary cohesive forces.

Embury and Nes (1974) used a critical strain criterion to model the initiation of cracks at grain boundary precipitates. The mechanism is illustrated in Figure 2.10. The condition for fracture is dependent on the areal fraction of precipitates at the grain boundaries, f_a, the size of those precipitates, and the grain size. Using the symbols from the figure, one can define the following terms:

shear strain : $\gamma = \frac{x}{h}$

collapse condition : $x = \frac{s}{2}$

areal fraction of precipitates : $f_a = (\frac{h}{s+h})^2$

Therefore, the condition for fracture, γ_{crit}, can be written:

$$\gamma_{crit} \propto \frac{1}{2}(f_a^{-1/2} - 1) \qquad [2.19]$$

Evensen et al (1975) considered the competition between the transmission of slip, fracture initiation at a grain boundary and its propagation. The role of grain boundary precipitates is expressed in their model in terms of a resistance to plastic flow, σ_o. The fracture condition is given as

$$\sigma_{app} > \frac{\sigma_o + (\sigma_{crit}/\phi)}{1 + 1/\phi} \qquad [2.20]$$

where ϕ is the stress concentration at the head of a slip band of length L (the grain size) and width W. One can therefore relate, in very simple terms, the critical stress for fracture to the grain size and at the same time include the role of grain boundary precipitates, as follows:

$$\sigma_{app} > \sigma_o + \frac{1}{L^{1/2}}(\sigma_{crit}\ \omega^{1/2}) \qquad [2.21]$$

This model compares favourably with experimental results for a high purity Al-Si-Mg alloy in the under, peak and over-aged conditions.

One can approach the problem of defining a more detailed mechanism of intergranular fracture in the absence of grain boundary precipitates, through the thermodynamics of atomic segregation (Seah, 1981). This is not practical for the material being studied because of the presence of precipitates. The precipitates make the fracture much more complex on the atomic level due to possible void nucleation at the precipitates and the presence of precipitate free zones (PFZ).

Despite the absence of a unique physically based criterion for intergranular fracture, it is still possible to describe the fracture criterion on a σ_1-σ_2 diagram. For the purpose of simple illustration, the intergranular fracture has been considered analogous to a cleavage failure. The theory behind the cleavage fracture surface calculations is discussed in Appendix A. The basis for the analogy between intergranular fracture and failure by cleavage is their essentially brittle nature. The comparison is therefore a limited one, since as discussed earlier, intergranular failure does not always occur by a purely brittle fracture mechanism. Since there is not much known of intergranular failure in compression, this approximation of the intergranular fracture surface is only valid in tension.

In summary, there are at least three questions of major significance that must be answered before fracture

mechanisms can be fully understood. How and why does decohesion at the grain boundaries occur, and what is the exact role of precipitates, PFZ's and other microstructural characteristics. Secondly, does shear deformation encourage void nucleation within the sheared region or, finally, is shear localization promoted by voiding. This study does not attempt to answer these queries, but rather examines fracture from the more global viewpoint of fracture maps.

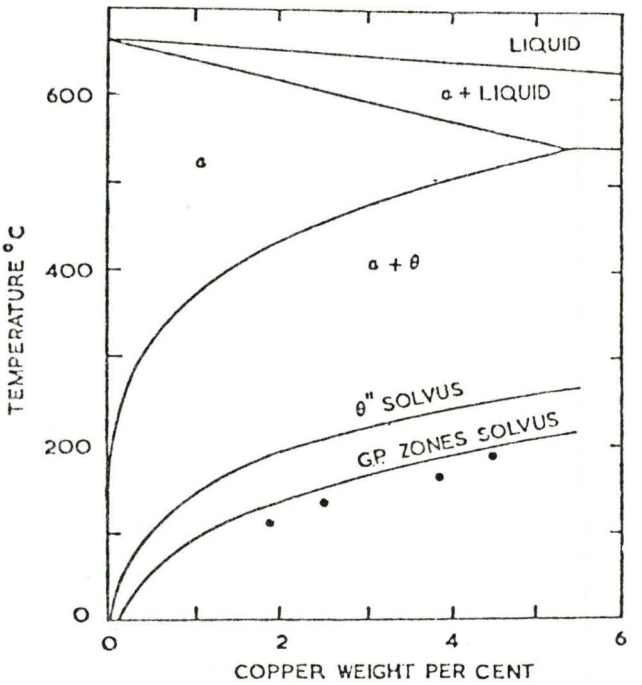

FIGURE 2.1 Al-Cu Phase Diagram

The phase diagram for the Al-Cu system showing the metastable phase boundaries for G.P. zones and θ ". (From Kelly and Nicholson, 1963)

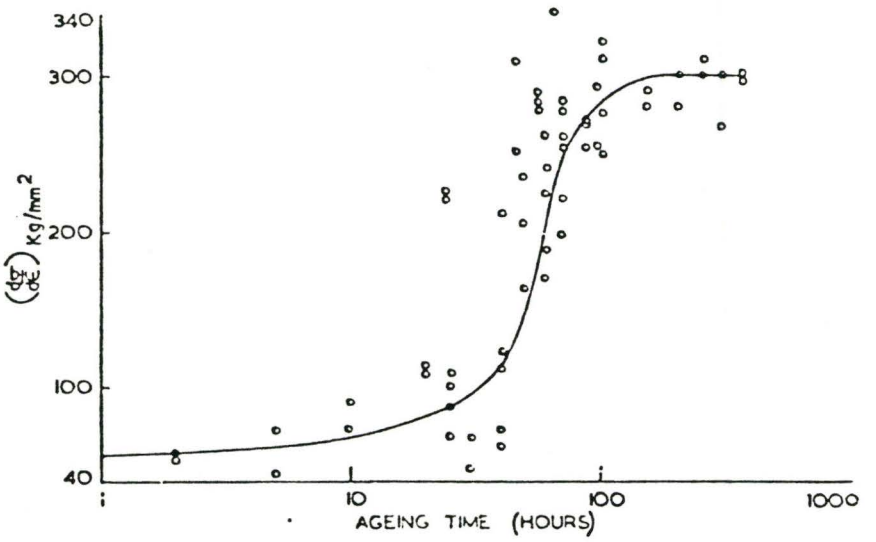

FIGURE 2.2 Initial Work Hardening Rate versus Ageing Time

Plot of rate of work hardening at 2 per cent elongation for Al 1.6 per cent Cu crystals aged at 190°C. (From Kelly and Nicholson, 1963)

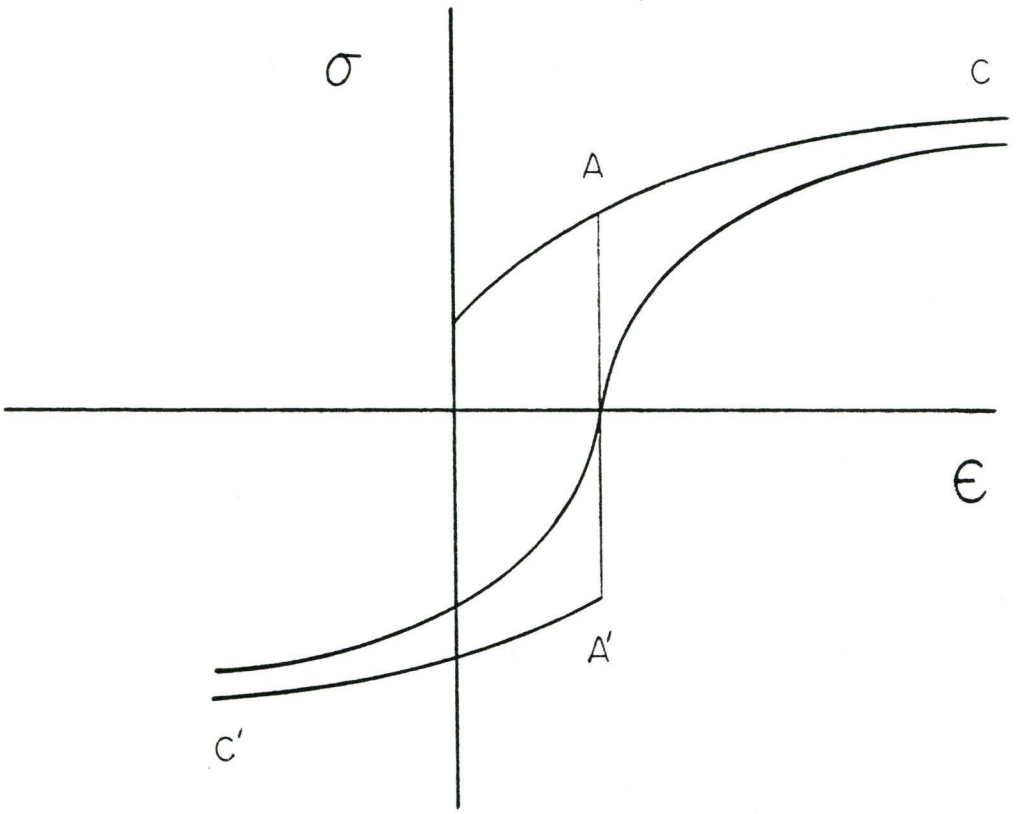

FIGURE 2.3 The Bauschinger Effect

The above schematic clearly illustrates both transient and permanent softening after strain reversal.

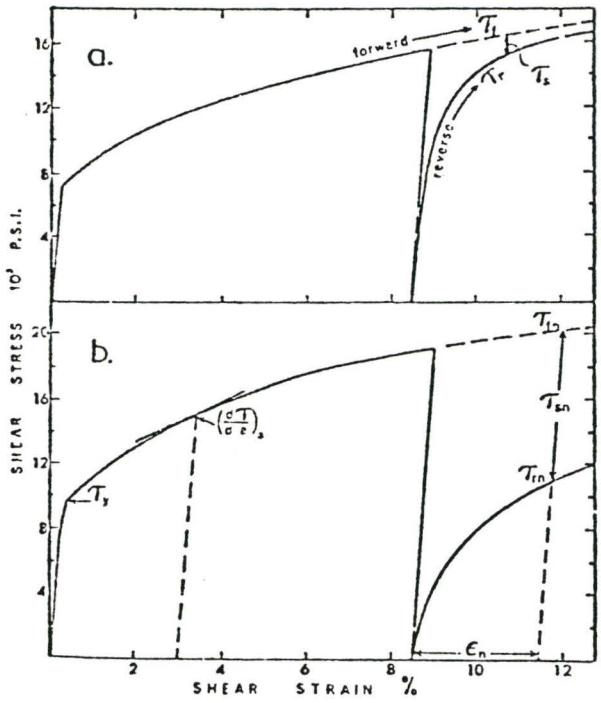

FIGURE 2.4 The Bauschinger Effect in Al 4 wt% Cu

Comparison of the Bauschinger effect in the same material but different heat treatments
(a) shearable particles
(b) non-shearable particles

Courtesy of Wilson (1965)

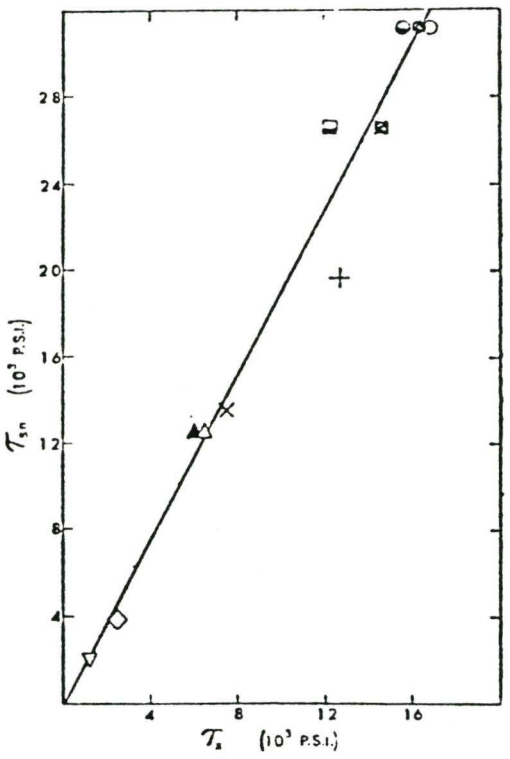

FIGURE 2.5 Magnitude of Back Stress versus Permanent Softening

The above values were recorded by Wilson (1965) for several different Al alloys.

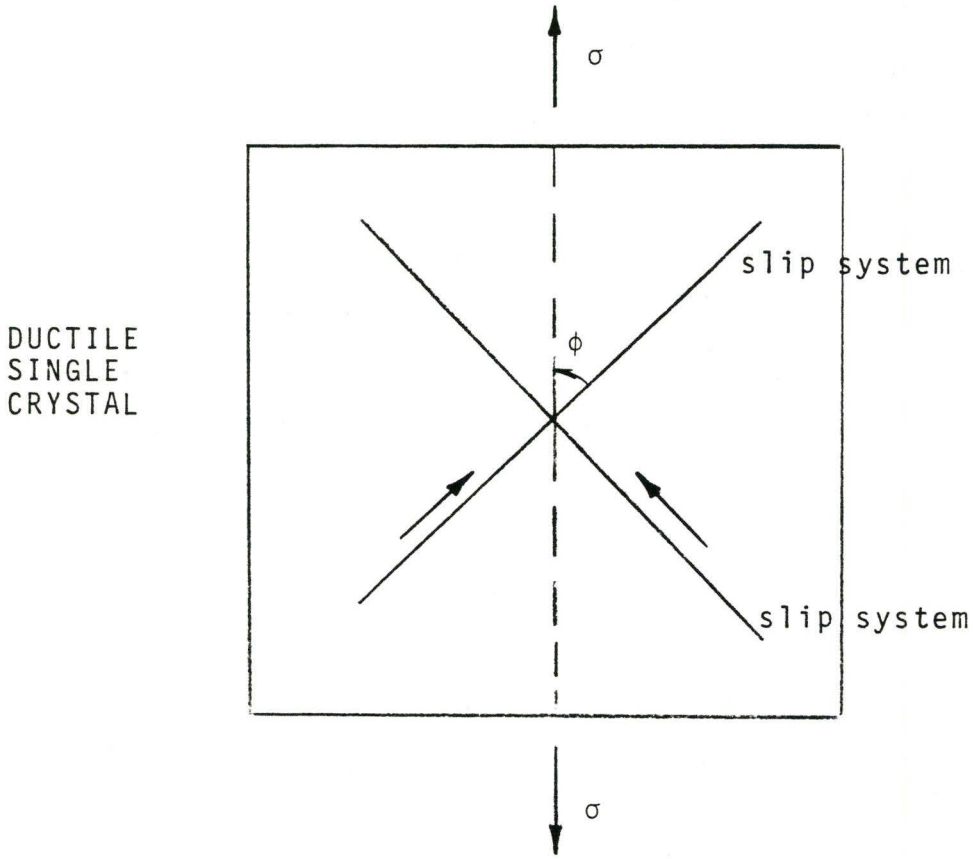

h, h_1 : elements of hardening matrix where $h_{11} = h_{22} = h$ and $h_{12} = h_{21} = h_1$

q : h/h_1

ϕ : angle between slip system and tensile axis

θ : angle between the shear band of equation [2.18] and the tensile axis.

FIGURE 2.6 Definitions of Terms Used in Equation [2.18]

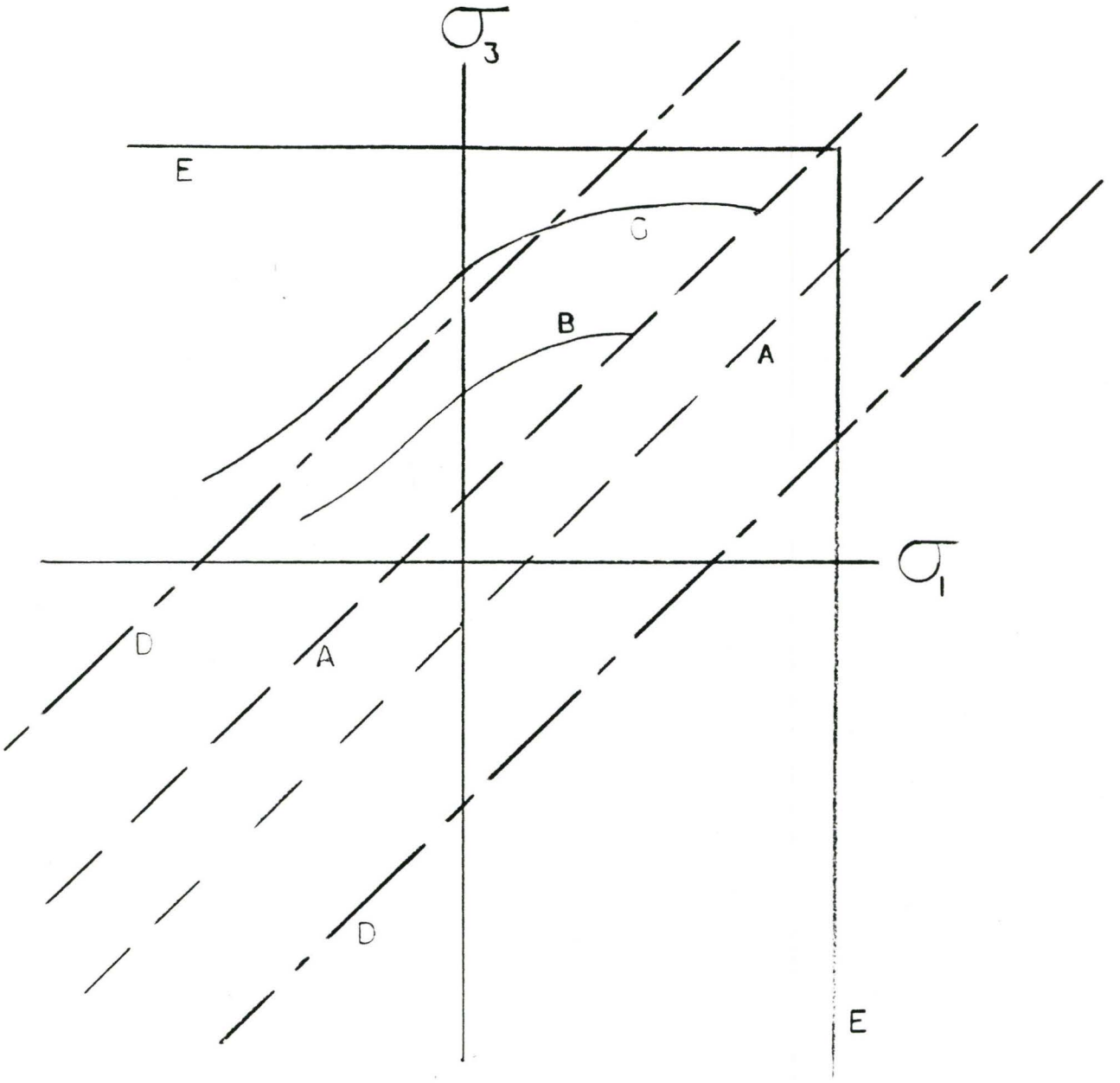

FIGURE 2.7 Schematic Example of an Axisymmetric Fracture Map

A: yield surface, von Mises criterion
B: void nucleation
C: ductile fracture
D: shear fracture, critical stress criterion
E: cleavage fracture

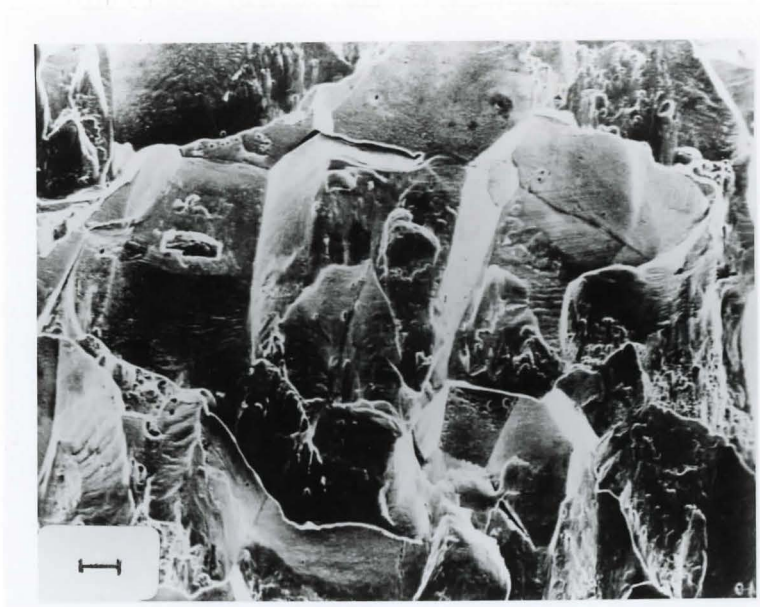

FIGURE 2.8 Intergranular Fracture

Magnification : 200 x (25μ marker)
The fracture surface exhibits areas of clean brittle fracture along the grain boundary and areas which have failed in the fibrous ductile mode.

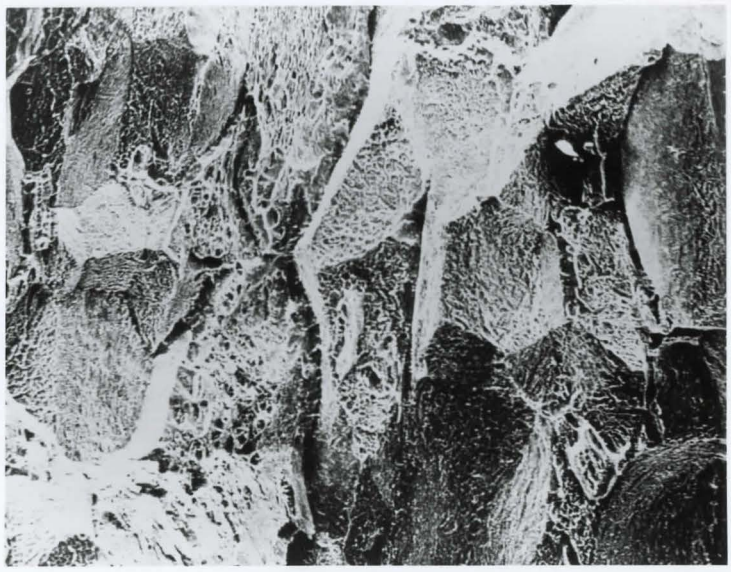

FIGURE 2.9 Intergranular Fracture

Magnification: 100 x
The fracture has followed an intergranular path but there is a significant amount of localized deformation throughout the whole surface.

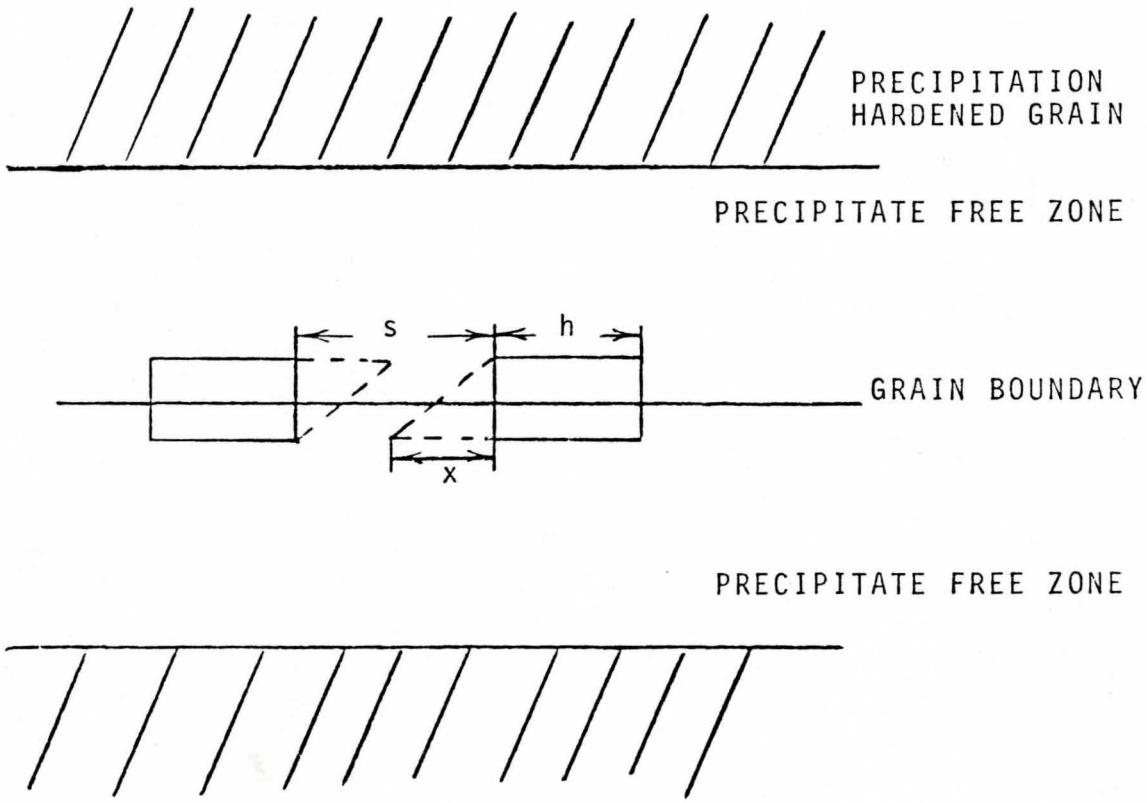

FIGURE 2.10 Mechanism of Grain Boundary Crack Initiation

A schematic diagram illustrating the process of grain boundary fracture initiation. (Embury and Nes, 1975)

CHAPTER 3

EXPERIMENTAL PROCEDURE

3.1 Material

In this study a comparison was made of the dependence of mechanical properties on strain path for Al and an Al-3.6% Cu alloy. The compositions (wt %) of the two materials used in the study are given in the table below.

	Cu	Fe	Mg	Si	Al
Al (pure)	.002	.001	<.001	.004	remainder
Al-Cu alloy	3.62	.002	<.001	.002	remainder

The Al 3.6% Cu alloy was received in the form of hot rolled plate, 2.5×10^{-1} m wide and approximately 1.4×10^{-2} m thick. In order to break down the as-cast structure and provide a uniform grain size the plate was reduced 22% in thickness, to 1.1×10^{-2} m, by rolling at room temperature prior to annealing. The pure aluminum received was also in plate form but had already been hot rolled. All machining of the test pieces, Al and Al-Cu alike, was done prior to any heat treatment. Test pieces were made for tension, compression and two stage tension. The original dimensions of the test specimens are shown in Figure 3.1. For compression testing, instead of the conventional cylindrical test pieces, cubes

approximately $5x10^{-7}$ m^3 were machined to facilitate changes in strain path. Aluminum test pieces were similar to the Al-Cu test pieces except that the cubes for compression testing were made slightly larger ($1.7x10^{-6}$ m^3).

In order to ensure recrystallization, the aluminum test pieces were initially heat treated at 540^oC for half an hour. It was found that this led to excessive grain growth and a non-uniform grain structure. Thus, a lower temperature, 300^oC, was chosen, and the heat treatment was repeated. This gave an average grain size, of $1.4x10^{-3}$ m, suitable for the dimensions of the test piece used.

For the Al-Cu alloy it was necessary to find a solution treatment which would not only permit the dissolution of $CuAl_2$ in the Al matrix but also allow recrystallization to occur. 540^oC for half an hour, followed by a room temperature water quench was found to yield a solid solution of uniform grain size without permitting too much grain growth. Since the material was completely recrystallized to an equiaxed structure during this solution treatment, it was assumed that the texture was random and thus, the orientation of the test pieces relative to the initial rolling direction was not considered to be a major influence on the test results. The average grain size of the solid solution was $7x10^{-4}$ m after recrystallization. After quenching, all test pieces were stored in the freezer compartment of an

ordinary refrigerator at -10°C.

The different heat treatments used in the course of this study are listed in Table 3.1 below.

TABLE 3.1 Heat Treatments

Material	T(^{o}C)	Time	Cooling Procedure
Aluminum	300°C	30 min.	water quenched
Al 3.6% Cu	540°C	30 min.	water quenched
Al 3.6% Cu	540°C 130°C	30 min. 4 days	water quenched air cooled
Al 3.6% Cu	540°C 200°C	30 min. 4 days	water quenched air cooled

3.2 Mechanical Testing

Tensile samples were deformed to fracture, at room temperature, using a 10,000 pound Instron testing machine with an FR load cell. The cross head speed was .02 inches per minute (5.1×10^{-4} metres per minute). This rate was chosen to permit photography of the test piece during the test. The choice of strain rate was not dictated by material property considerations since the properties of aluminum alloys experiencing continuous flow are not strongly strain rate dependent at room temperature (Tegart, 19).
The chart recorder and load cell were calibrated before each set of tests. From these tests the true stress-true strain curve, the yield and fracture stresses in tension and mode of fracture were determined.

The calculations of true stress and true strain prior to necking were made using information obtained directly from the load-elongation curve plotted by the Instron chart recorder. Total plastic strain calculated using the chart was consistent with direct measurements of the test piece before and after each test. Due to the continuous yielding exhibited by Al alloys yield stress values quoted in this work are proof stresses, calculated at .2% elongation (see Figure 3.2).

The true stress and true plastic strain, if calculated directly from the load elongation chart, will give the mean tensile stress over the cross section of the sample. However, after the onset of necking due to the variation of stress across the sample, the mean tensile stress is greater than the true uniaxial tension at the minimum section.

Bridgman proposed a correction factor, $\frac{1}{(1+\frac{2R}{a})\ln(1+\frac{a}{2R})}$, that would convert the mean stress to the true axial stress. The correction factor is based on an estimate of the radial stresses caused by necking. It depends on the parameter a/R, a being the minimum radius of the sample and R being the radius of curvature of the neck. In other words, the shape of the neck contour and its effect on the stress distribution across the sample's cross section are assumed to be independent of the material.

This conclusion is supported by evidence given by

Bridgman. Bridgman plotted a/R as a function of $\log_e A_o/A$ for several materials including several steels and brasses in Figure 3.3. The curves for each material were similar. For the purpose of this study it has been assumed that the necking behaviour for Al, and Al-Cu are similar to those given by Bridgman. The error of this assumption is considerably smaller than the error in direct measurements of R from the sample profile. There are two reasons for this; necking is not that extensive in the samples under study and, when necking does occur the shape of the neck may be quite irregular (see Figure 3.4).

The minimum diameter at the neck was measured from photographs taken during the tensile test. From this measured value of d_i, $\log A_o/A$ can be determined, since it is assumed that the volume of the sample remains constant throughout the test. For each value of $\log_e A_o/A$, a/R was extrapolated from Bridgman's curve (1943). This was then used to calculate the correction factor. The mean stress was then calculated using the measured area at the neck, and converted to true tension for flow by the use of equation [3.1].

$$\frac{\sigma}{\sigma_{ave}} = \frac{1}{(1 + \frac{2R}{a})\ n(1 + \frac{a}{2R})} \qquad [3.1]$$

Trozera (1963) has confirmed that this method of using the Bridgman technique compares favourably with results obtained

for a Type 1100 aluminum alloy from direct measurements of the sample. The fracture stress was calculated in the same manner. The value obtained compared well with that one based on the radius at the neck measured directly from the sample after fracture had occurred.

Compression tests were conducted using the same Instron testing machine and load cell. The deformation rate used in compression was .05 inches per minute (1.27×10^{-3} metres per minute). Four test pieces of each material were compressed in the A direction only. Each set of samples was compressed to a different final value of strain. The samples were compressed in steps of approximately 10-15% strain. Before each step the two faces to be compressed were lubricated with a coating of Teflon spray. Teflon tape was found to be the best lubricant for the pure aluminum.

Another set of samples was compressed to approximately 15% strain in the A direction. The cubes were then machined so that the B faces were flat, normal to the A direction and parallel to each other. The compression was continued another 15% strain in the B direction. This procedure was repeated in the C direction. Whenever the compression test was interrupted the sample was relubricated as in the unidirectional tests. In all compression tests it is important to determine if any barrelling or non-

uniform deformation occurs. In the present work it was found that the cubes of pure aluminum were distorted at much lower strains than those of Al-Cu. For this reason the aluminum was compressed in steps of 5-7% strain. The sides of the test pieces were machined after each step so that they would be flat and parallel to each other. It is because of the steps of strain being smaller for the pure Al and therefore more machining being necessary, that a larger sample size was needed. Lubricant was applied after each step.

It was necessary to determine whether or not this described procedure was affecting the test results. In order to do so, three sets of the four materials were compressed to a total strain of 45% strain in the A direction. The first set received only one coat of lubricant throughout the entire test. A second set of tests was conducted during which the load was released several times and lubricant was reapplied before reloading. The third set of test pieces were compressed uniaxially in steps of 15% strain, interrupted by the machining of first the B and then by the machining of the C faces. The results are compared in Figure 3.5. No significant differences were found. However, the use of lubricant did diminish distortion of the cubes.

Despite the use of lubricant it is impossible to totally eliminate friction between the sample surfaces and

the compression platens. To determine how significant the effect of friction was, the tensile test results were compared to the compression test results. The stress levels are within 10% of each other up to a strain of $\varepsilon = .22$.

An additional set of compression tests were conducted using the conventional cylindrical test pieces with a height to diameter ratio of 1.5. These were compressed at room temperature using a hydraulic press in an attempt to find the fracture behaviour in compression. No lubricant was used, but the effects of barrelling were minimized by remachining the samples several times during the compression test (Kuhn and Lee, (1971), Lee and Kuhn, (1973)).

The tests measuring strain path changes in tension mentioned earlier, consisted of machining a sample as shown in Figure 3.6, heat treating it and then pulling it to its maximum uniform strain. A second test piece was then machined from the gauge length of the first sample, normal to the original tensile axis (Figure 3.7). This sample was then pulled in tension to fracture and the yield and fracture stresses were noted.

3.3 Metallography

Samples were prepared for metallography using normal polishing procedure. First the sample was mounted in bake-

lite and then polished down to 600 grit silicon carbide paper. Then polishing was continued first with 6 micron diamond paste and then with 1 micron paste. A rotopol polishing machine was then used to complete the polishing using 0.3 micron alumina powder and water as a lubricant.

The etchant used depends on what aspect of the microstructure is of interest. In this case Keller's etchant was used for the Al-Cu samples. This etchant preferentially reveals the grain boundaries. Keller's etchant consists of:

- HF (48%) .5 mℓ
- HCl (conc) 1.5 mℓ
- HNO_3 (conc) 2.5 mℓ
- water 95 mℓ

3.4 Scanning Electron Microscopy

The SEM was used to observe the fracture surfaces of each material after it was pulled in tension. A microscope was used. The tip of the fractured sample was cut from the bulk of the test piece so that it could fit into the microscope. No other sample preparation was involved. Pictures were taken of each surface. The other half of each of the fractured tensile test pieces was cut in half lengthwise and mounted in bakelite. This inner surface was polished for metallographic observation in the manner already described and then etched. These samples were also observed

with the SEM. The results are discussed later.

3.5 Transmission Electron Microscopy

Samples used in the TEM must be thin foil sections of the material so as to permit the electrons to pass through. To prepare the material the following thinning procedure was followed.

The samples were initially in the form of compressed cubes. These cubes were sliced using a spark cutter so as to limit the amount of damage to the microstructure during cutting. A spark cutter consists of a slowly moving continuous Mo wire, .76 μm in diameter. A voltage is applied between the wire and the sample, kerosene is used as a coolant. Slices were cut about .015 inches thick (3.8×10^{-4}m). All slices were polished on both sides using 600 grit paper to remove kerosene and dirt accummulated during the slicing procedure. After polishing the slices were between .006 and .010 inches ($1.5 - 2.5 \times 10^{-4}$ m) thick. Discs 3×10^{-3}m in diameter were cut from the slices using a stainless steel punch.

The electropolishing was carried out in a standard Tenupol electropolishing device. The electrolyte was a mixture of 65% methanol and 35% nitric acid. After polishing the discs were washed in water, in methanol, and then carefully dried. Whenever thin foils were not being examined

with the TEM they were stored in the freezer as before.

The transmission electron microscope used was a Philips EM 300, 100 Kv microscope, with a single tilt specimen holder.

3.6 Computer Work

An Apple II Plus mini-computer was used for calculations of stress strain curves and work hardening rates, plotting of stress strain curves, work hardening rate versus strain curves, yield surfaces and fracture surfaces. Floppy discs were used to store data from the mechanical testing.

Programs written to perform the above are listed in the appendix.

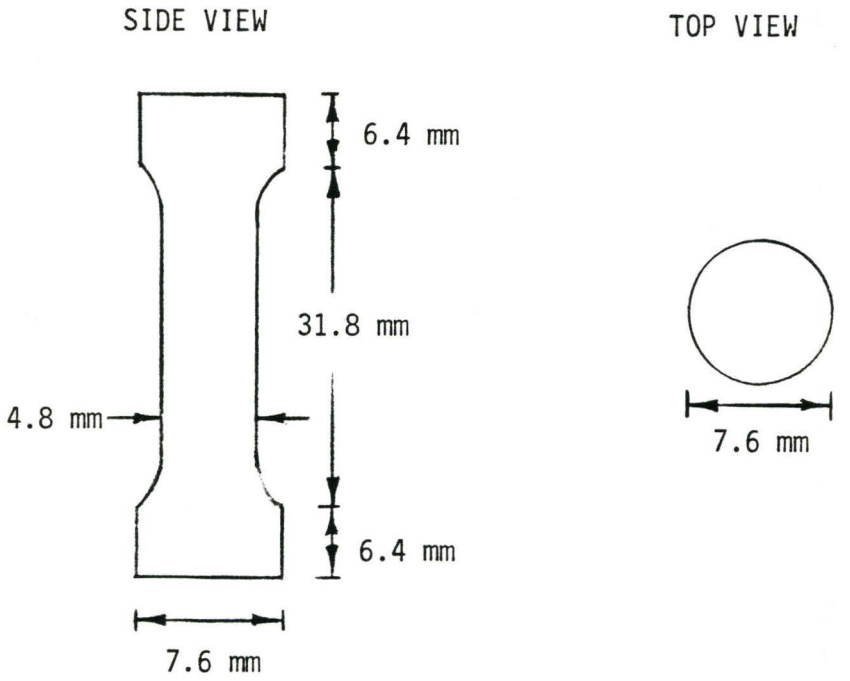

(a)

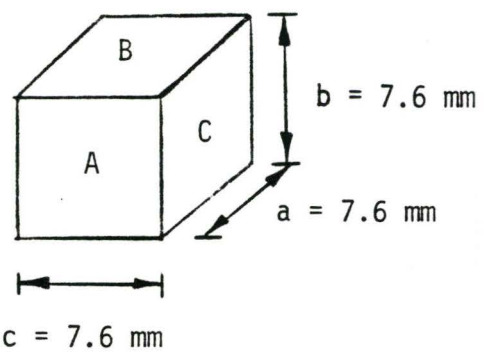

(b)

FIGURE 3.1 Test Specimen Dimensions

(a) uniaxial tension
(b) uniaxial compression and change in strain path tests

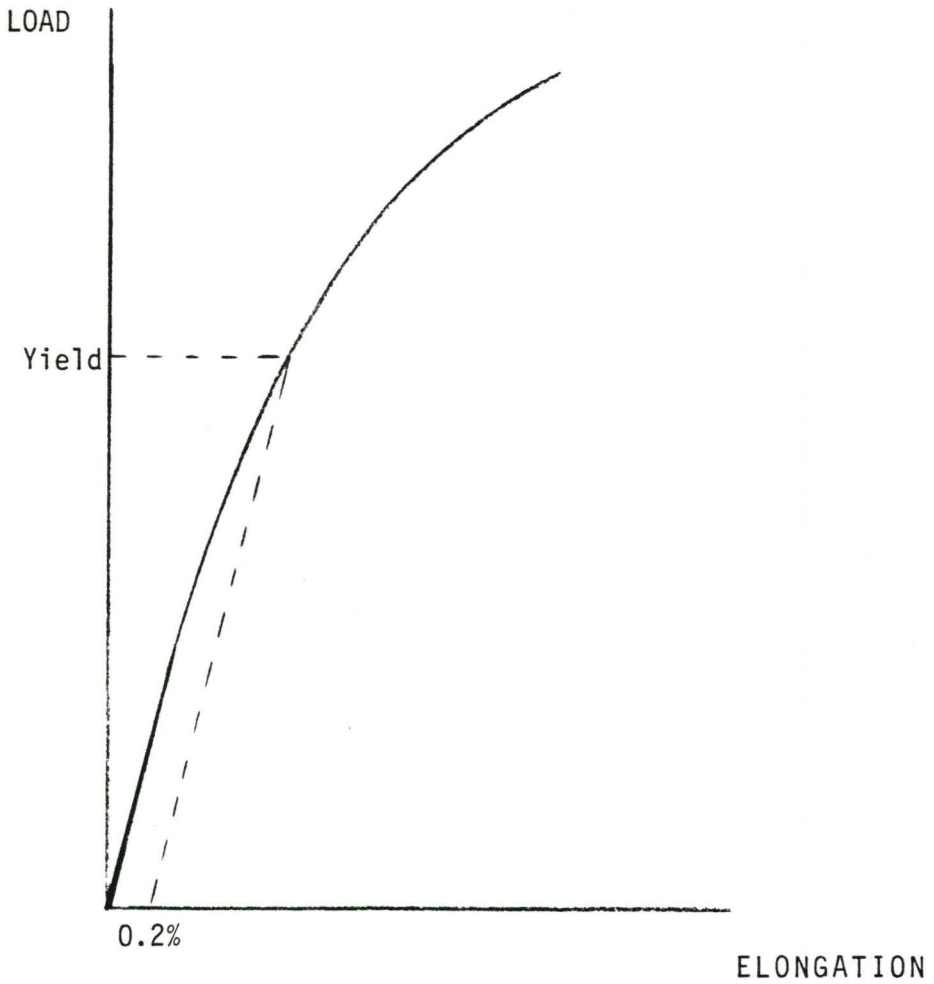

FIGURE 3.2 Definition of Yield Stress

The schematic illustrates how the yield stress, or 0.2% proof stress, was determined for each test conducted in the present study.

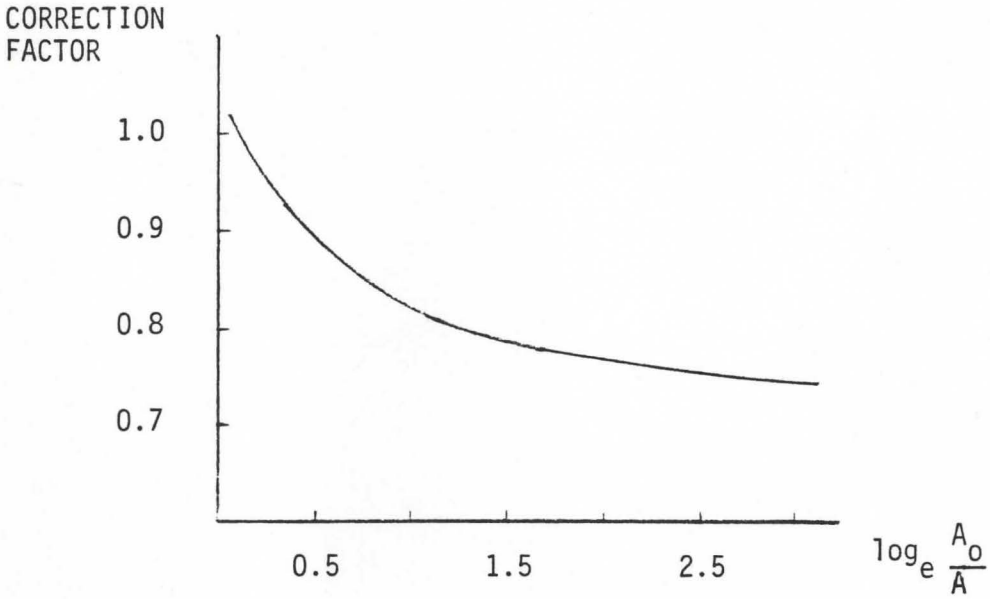

FIGURE 3.3 $\frac{a}{R}$ versus $\log_e \frac{A_o}{A}$

Courtesy of P.W. Bridgman (1943)

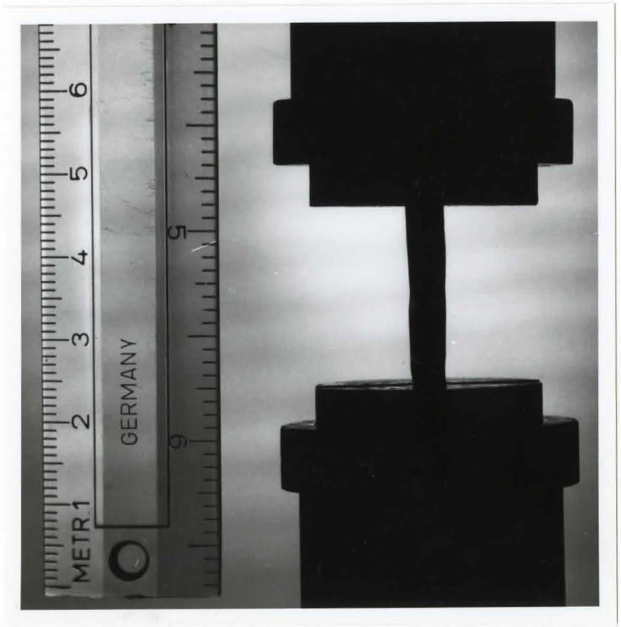

FIGURE 3.4 Typical Silhouette of Pure Aluminum Neck During a Tensile Test

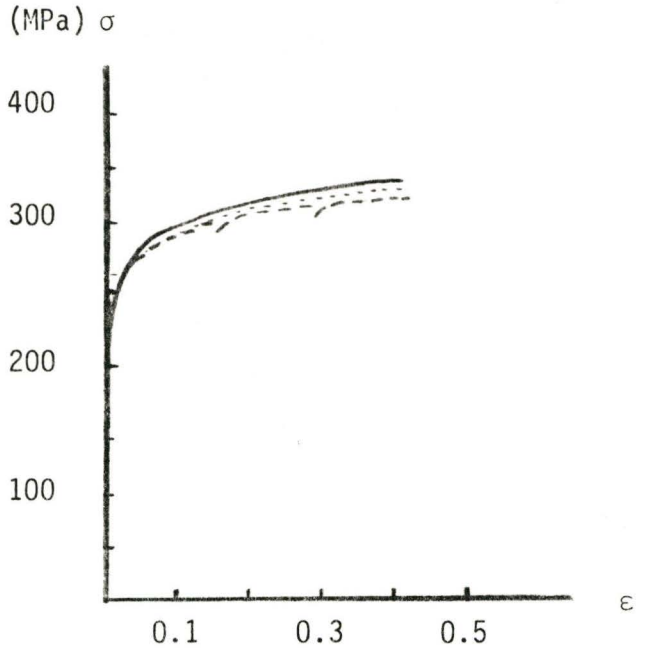

FIGURE 3.5 Comparison of Different Compression Testing Procedures

A ——— - no remachining of sample
- single application of lubricant
- no interruptions during the test

A1-A2-A3 ····· - no remachining of sample
- 3 applications of lubricant, therefore 3 interruptions:A1, A2, and A3

AA ----- - 2 or 3 applications of lubricant during the first 15% strain
- after 15% strain in the A direction, the B and C faces were remachined perpendicular to the A face

AB ----- - relubricated as above
- compressed in the A direction
- after another 15% strain in the A direction the B and C faces were again machined perpendicular to the A faces

AC ----- - relubricated as above
- compressed in the A direction a final 15% strain (cumulative strain in the A direction: 45%)

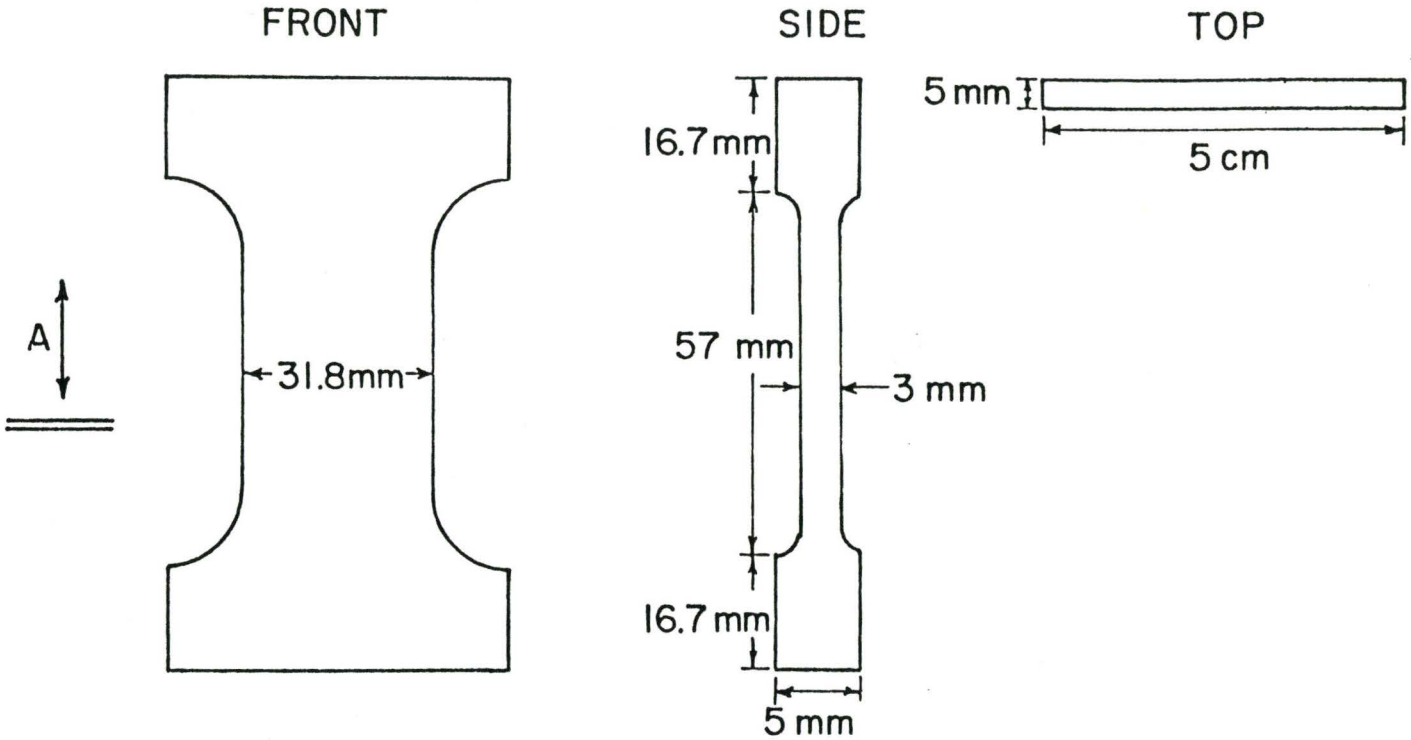

FIGURE 3.6 Two Stage Tensile Test: Stage I

Stage I: Apply 5% prestrain in the A direction as shown above. This test was conducted with specimens in the peak and over aged conditions.

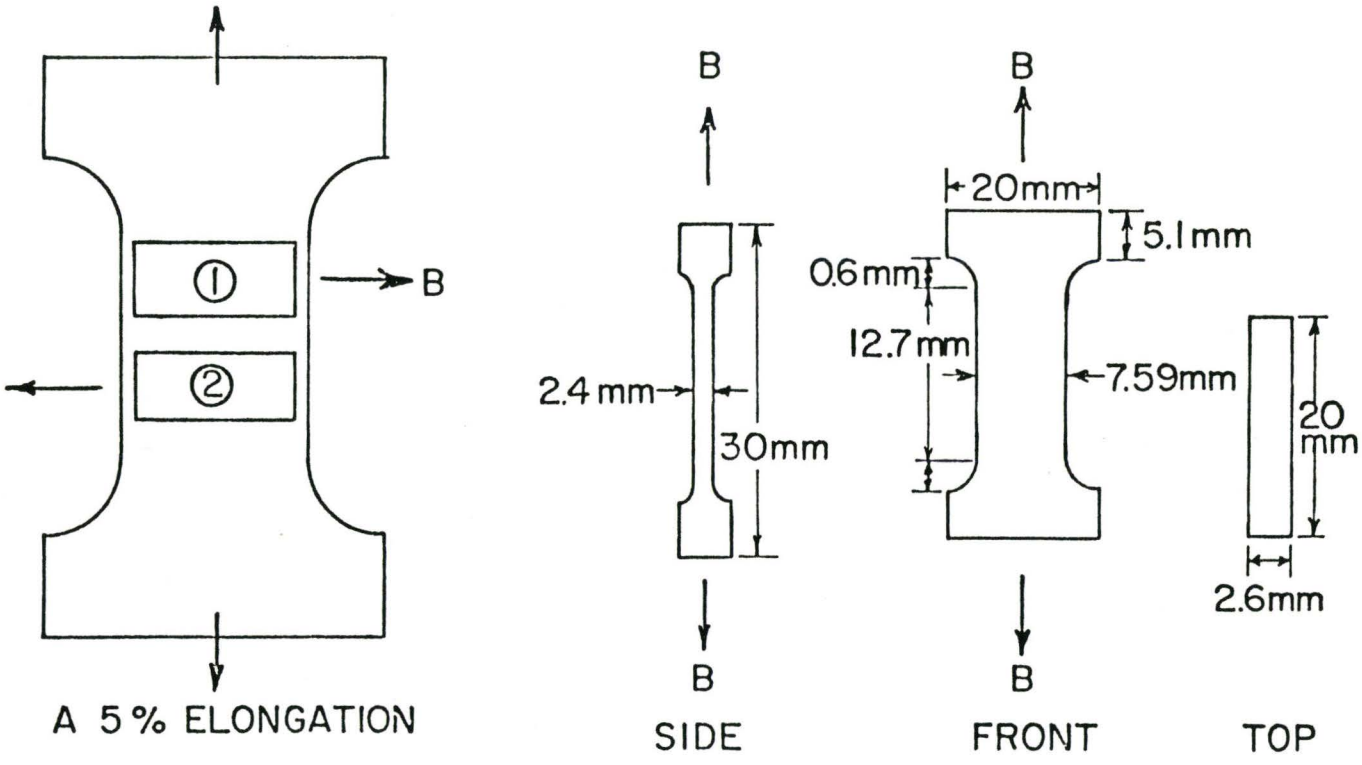

FIGURE 3.7 Two Stage Tensile Test: Stage II

Stage II: pull the specimen in the B direction until it fractures.

CHAPTER 4
RESULTS

The previous chapter was a description of the tests performed, and the procedures followed, to determine both the basic stress strain response and the effect of a change in strain path during plastic deformation for a variety of materials. The results of these experiments are presented in this chapter, and will be discussed in detail in Chapter 5. For clarity, the mechanical property data will be presented first followed by a description of the microstructural features.

4.1 Basic Mechanical Properties

As mentioned in Chapter 3 the initial tests conducted were tensile tests, the purpose of which was to determine the mechanical properties of each material. The tensile stress strain curves of each of the four materials being studied are shown in Figure 4.1. Important material properties, such as yield stress, fracture stress, strain to fracture, etc., are given in Table 4.1.

It is important to note that the general shape of the stress strain curve is the same in tension and compression for each of the four materials. Figure 4.2 compares the curves

for the solid solution alloy obtained in tension and compression. The effects of friction during compression testing appear to have been successfully minimized.

TABLE 4.1 Material Tensile Properties

Material	σ_y (MPa)	θ_o at ε = .05 (MPa)	ε_{fr}	σ_{fr} (MPa)
Al	55	300	2.6	215
Solid Solution Al 3.6% Cu	130	1100	0.91	390
Peak aged Al 3.6% Cu	190	1100	0.32	410
Overaged Al 3.6% Cu	160	1450	0.71	380

4.2 Work Hardening Characteristics

The stress strain curve can be divided into two regions; initial, purely elastic behaviour, followed by elastic-plastic deformation. Within the plastic region it is easiest to categorize the material's work hardening characteristics by considering them at low and high strains separately.

It is usual to represent the work hardening of a material by considering the instantaneous rate of hardening

$\frac{\partial\sigma}{\partial\varepsilon}$, here defined as θ, and following its development with respect to strain. θ vs. ε has been plotted for each material in Figure 4.3, θ vs. σ in Figure 4.4.

It is evident from Figure 4.1 that at low strains ($\varepsilon \leq 0.05$) the overaged Al-Cu exhibits the highest average work hardening rate, and pure aluminum the lowest. The solid solution condition of Al 3.6% Cu has an initial work hardening rate much greater than that of Al; θ_o = 1100 MPa as opposed to θ_o = 300 MPa (values taken at ε = 5%). The initial work hardening rate of the peak aged material is of the same order of magnitude as, though less than, that of the overaged material; θ_o = 1100 MPa and θ_o = 1450 MPa respectively. At high strains the work hardening rate of aluminum decreases steadily until it reaches a value of approximately 15 MPa at $\varepsilon \cong 0.6$. It maintains this same value until fracture occurs at ε = 2.61.

From a strain of 0.60 until fracture, the solid solution material also maintains a relatively constant work hardening rate, $\sim$50 MPa. This is higher than θ in the same strain region of Al. This value compares favourably with results obtained by Dew Hughes and Robertson (1960). They report a work hardening rate of approximately 100 MPa at ε = 0.40 in an Al 4% Cu solution treated single crystal.

The peak aged material maintains a high work hardening rate (θ > 100 MPa at ε = 0.30) until fracture. Price and Kelly (1964) conducted tensile tests, at room temperature, on

Al 3.7 wt % Cu single crystals. After solution treatment the material was aged for two days at 165°C. The sample at a strain of 0.20 , had a work hardening rate of 290 MPa, consistent with the results of this study. At a similarstrain the work hardening rate of the overaged material has greatly decreased from its initially high value i.e. $\theta < 100$ MPa at $\varepsilon = 0.30$.

Sections 4.1 and 4.2 have summarized the basic mechanical properties of the four materials tested for this study. The following describes the results of compression tests during which the strain path direction was rotated 90° after 15% plastic strain.

4.3 Change in Strain Path

The results of the change in strain path experiments, described in Chapter 3, are presented in Figures 4.5 to 4.8. Though the change in strain path is one of 90° not 180°, the data has been presented in Table 4.2 in the same manner as that used for Bauschinger type tension-compression tests. The table gives the yield stress in each subsequent direction, and the "back stresses" $\sigma_b^{-A:-B}$ and $\sigma_b^{-B:-C}$ as a percentage of total work hardening for each material.

Neither the pure aluminum, the Al 3.6% Cu solid solution nor the peak aged condition show any marked evidence of permanent softening or "back stress" build-up after 15% strain

TABLE 4.2 Compressive Yield and 'Back' Stresses

Material in Compression	σ_y^{-A} (MPa)	σ_y^{-B} (MPa)	σ_y^{-C} (MPa)	$\sigma_b^{-A:-B}$ (MPa)	$\sigma_b^{-A:-B}$ / wk hdg (%)	Increment of Strain
Pure Aluminum	62	79	84	1.1	6%	15%
Al 3.6% Cu Solid Solution	160	315	350	12.5	7.1%	15%
Al 3.6% Cu Peak Aged	210	370	410	16.5	8.4%	15%
Al 3.6% Cu Overaged	160	200	220	60	38%	15%

in the A direction. A drop in flow stress is noted after the B to C direction change in the solid solution condition, but not in the peak aged condition. The solid solution shows, after cumulative strains of 15% in the A and then the B directions, a small drop in flow stress in the subsequent compressive C direction. This yield drop could be due to an effect of texture or, damage accumulation in compression.

The overaged material exhibits a large drop in flow stress after both the A to B and B to C changes in direction. In addition a significant permanent softening is evident. A strain of approximately $\varepsilon = .10$ in the B direction is necessary to reach σ^A_{final} and similarly a strain of about $\varepsilon = 0.10$ in the C direction before σ^B_{final} is reached.

The response of the overaged material to a 90° change

in strain direction is similar to that seen in the same material after a strain path reversal (Moan,1977). A decrease in the flow stress of a work hardening material due to strain path reversal is a form of the Bauschinger effect. The Bauschinger effect has been well documented for a number of materials including Al-Cu. The data of Moan (1977) for over-aged Al-Cu is compared with the results of this study in Table 4.3 below.

Table 4.3 'Back' Stress Values for the Bauschinger Effect and for the Present Study

α Angle of Change in Strain Path (degrees)	σ_b (MPa)	$\frac{\sigma_b}{\text{wk hdg}}$ (%)	Amount of Prestrain (%)
-A:-B 90°	60	38%	15%
+A:-A 180°	71 (inferred)	45%	15%

Table 4.3 shows that though the effect is similar for $\alpha = 180^o$ and $\alpha = 90^o$, there is a smaller drop in flow stress (i.e. a smaller "back stress") for $\alpha = 90^o$. The degree of permanent softening is also less for $\alpha = 90^o$ but is still present. This suggests that there is a relation between the magnitude of back stress and the angle α between

directions A and B. More data for other stress states and strain path changes is necessary to determine the nature of this relationship.

To confirm the results obtained in compression, a two stage tensile test was designed and performed. The details of the experiment were described in Chapter 3. The results are similar to those obtained in compression. Table 4.4 compares measured values of "back stress" accumulation in tension and compression.

TABLE 4.4 'Back' Stress Values from Two Stage Tensile Tests

Material	Direction	σ_b (MPa)	$\frac{\sigma_b}{wk\ hdg}$
Peak Aged Al 3.6% Cu	5% prestrain two stage tensile	5.5	4.4%
Peak Aged	15% prestrain compression	16	8.4%
Overaged Al 3.6% Cu	5% prestrain two stage tensile	19	20%
Overaged Al 3.6% Cu	15% prestrain compression	60	38%

4.4 Fracture

In the tensile tests performed the fracture behaviour of each of the materials was also observed. The results of

the fractographic observations are presented in this section. The essential form of each of the tensile, true stress-true strain curves has already been summarized (Figure 4.1). Each fracture has been characterized by its value of strain to failure, true axial stress at fracture, radial stress component at fracture plus the dominant mode of fracture observed. This data is presented in tabular form below (Table 4.5).

TABLE 4.5 Fracture Data

Material	$\varepsilon_{fracture}$ (true)	$\sigma_{fracture}$ (corrected) (MPa)	σ^{max}_{radial} (MPa)	predominant features of fracture surface
Al	2.6	215	82	fibrous ductile
Al 3.6% Cu Solid Solution	0.91	390	81	fibrous ductile
Al 3.6% Cu	0.32	410	~0	intergranular plus shear
two stage tensile	ε_A = .05		—	
	ε_f^B = .13	380		intergranular plus shear
Al 3.6% Cu	0.71	380	70	intergranular (dimpled)
two stage tensile	ε_A = .05		—	
	ε_f^B = .23	330		intergranular (dimpled)

Fracture modes are often mixed, as in the case of the peak aged material which shows regions of both intergranular and shear failure. Hence a detailed study, using Scanning Electron Microscopy (SEM) was necessary in order to characterize the dominant failure mode of each material (at room temperature), and to quantify the scale of the observed fractographic features. These were then compared with the appropriate features of the microstructure, mechanisms of deformation and mechanical properties of the material. The fractographic data are presented in Figures 4.9 to 4.12. The failure mode of each material was derived from both SEM studies and optical metallography of a central section cut parallel to the tensile axis.

The fractographic features from the two stage tensile tests were similar to those of the uniaxial tests. However, it must be noted that after 5% strain in the A direction the tensile fracture stress and strain in the B direction are significantly lower than in the A direction (see Table 4.5). This is true for both of the materials tested.

4.5 Microscopy

Thin foils of each of the four materials under study were examined with the Transmission Electron Microscope (TEM). Their microstructures were observed prior to deformation and after a series of different uniaxial strains. The purpose of

this was to permit the observation of the development of the microstructure as strain accumulates. A summary of the samples prepared and their figure numbers are given in Table 4.6. In each case the plane of the foil was parallel to the direction of compression.

TABLE 4.6 Micrograph Figures

Material	ε_A					$\varepsilon_A + \varepsilon_B$
	0.	0.18	0.38	0.46	0.45	0.45 + 0.45
Al	—	—	4.23	—	4.25	4.26
Solid Solution	—	—	—	—	4.35	4.36
Peak Aged	4.41	—	4.43	—	4.45	4.46
Overaged	4.51	4.52	—	4.54	4.55	4.56

Figures 4.41 and 4.51 show the typical microstructure of the peak and over aged materials of this study prior to any deformation. The average precipitate size in the peak aged material is 0.01-0.02μ, in the overaged condition it is approximately 0.9μ. The average interparticle distance is 0.02μ and 0.5μ respectively.

The monotonic development of the dislocation substructure of pure aluminum has been studied and reviewed in great detail (Chandra, 1980). Thus the present study does not attempt to do so. Figures 4.23 and 4.25 show the change in microstructure with an increase of uniaxial strain in poly-

crystalline aluminum. Not until a strain of at least ε_A=-0.38 is reached is there any significant preferential orientation of the cellular structure with respect to the compression axis. At a strain of ε_A = -0.45 the average length of the cells perpendicular to the compression axis is 2.9μ, the width parallel to the compression direction is 1.1μ.

It is very difficult to resolve any changes in the substructure of the solid solution at low strains. However the deformation appears to be fairly homogeneous, and even at relatively low strains the material has a high dislocation loop and dipole density. At a strain of ε_A = -0.45 (Figure 4.35) an interesting feature was observed. Bands of inhomogeneous deformation have formed. There is a slight misorientation across these bands, however it was not measured in this study. Similar bands were observed by Nourbakhsh et al (1980) in Al 4 wt% Cu rolled to 40% reduction. Nourbakhsh et al (1980) state that they are likely to correspond to slip bands on the basis that they change direction at grain boundaries. No grain boundaries were located in the foils observed in this study therefore the orientation of these bands with respect to the matrix was determined by selected area diffraction. The results confirm that the lines observed are indeed slip bands parallel to {111} along the (110) and $(0\bar{1}1)$ directions. At higher strains , ε_A > -0.45 (Figure 4.35), the secondary slip bands are more evident, always shearing

the primary slip bands at the same angle. The primary slip band spacing is 1.80μ, the spacing of the secondary slip bands is 0.72μ. At a strain of ε_A = -0.45 plus ε_B = -0.45 (Figure 4.36) the shear strain of the primary bands caused by the secondary bands is quite pronounced.

The microstructure of the peak aged material develops in a way similar to that of the solid solution. At a strain of ε_A = -0.38 the primary bands predominate (Figure 4.43). At a cumulative strain of -0.90 the primary slip bands are 2.5μ apart and the secondary bands are 1.7μ apart. (These are values averaged from several areas of the foil.) The slip band spacing is two orders of magnitude larger than the average particle spacing in the peak aged material (0.02μ).

Many more measurements are necessary before a detailed comparison of these two microstructures can be made. However several general observations may be made. The slip band spacings are the same order of magnitude in both materials. The primary bands seem to be slightly further apart than the secondary bands. At high strains it is possible to see the shear of the primary slip bands in the peak aged material (Figure 4.46), and in the solid solution (Figure 4.36).

In contrast to that of the peak aged Al-Cu, the substructure and the particle spacing in the overaged material are of the same order of magnitude. In other words, the $CuAl_2$ precipitates may form a portion of the cell walls.

This substructure begins to form at very low strains, $\varepsilon_A = -0.18$ The cell size does not seem to vary with strain in the range of strains included in the present study. However, the density of well developed cells increases with strain. All the cells observed are oriented perpendicular to the strain path direction as shown in Figure 4.55. It was also observed that at the higher values of strain ($\varepsilon_A = -0.46$) the precipitates are distorted. Whether they are bent elastically or plastically deformed (or cut) is not possible to determine without a more detailed study. Most of the distorted precipitates observed are perpendicularly to B, the second compression axis.

Following the microstructural study of the monotonic development of each of the materials, the effects of a 90° change in the direction of imposed compression were examined. In order to simplify the analysis a separate set of cubes were compressed to a strain of $\varepsilon_A = -0.45$ in the A direction followed by a strain of $\varepsilon_B = -0.45$ in the B direction. In each case the plane of the foil was parallel to both the A and the B compression directions. No strain was imposed in the C direction. Typical microstructures of each material are shown in Figures 4.26, 4.36, 4,46 and 4.56.

Figure 4.26 shows pure aluminum after an accumulated strain of $\varepsilon_A = -0.45$ plus $\varepsilon_B = -0.45$. A similar structure to that seen in Figure 4.25 is observed, the only difference being

that it is oriented with respect to the B direction instead of the A. The average width of a cell parallel to B is 0.9μ, the average length to A is 1.9μ.

The solid solution and peak aged conditions do not respond to the change in direction as dramatically as the Al. This is to be expected since the active mode of deformation in these two materials is primarily crystallographic in nature, not macroscopic. Therefore Figure 4.36 and 4.46 show evidence of increased strain only.

In the overaged Al-Cu marked changes occur as a result of changing the strain path direction. A typical area of the material at a strain of ε_A=-0.45 plus ε_B=-0.45 is shown in Figure 4.56. Within the area observed the microstructure is no longer elongated normal to the A compression axis (Figure 4.55). The only visible reminder of the previous 'A' microstructure is the bending of plates parallel to the B direction. It is possible that these bent (or fragmented) precipitates previously formed the cell walls in the A microstructure. These results are in accord with the view that these large particles play an important role in the mechanisms of plastic deformation active in the overaged Al-Cu.

The next two pages form a brief summary of the data presented in this chapter. The results of the microstructural study of each of the four materials will be discussed in relation to their respective work hardening characteristics in Chapter 5.

SUMMARY OF RESULTS

TABLE 4.7

Material	σ_y^{+A} MPa	σ_y^{+B} 5% prestrain MPa	$\sigma_b^{+A:+B}$ wk hdg %	σ_f MPa	ε_f
Aluminum	55	—	—	215	2.6
Solid Solution		—	—	380	0.91
Peak Aged	190	300	4.4%	410	0.32
Over Aged			18%	380	0.71

TABLE 4.8

Material	σ_y^{-A} MPa	σ_y^{-B} prestrain MPa	$\sigma_b^{-A:-B}$ wk hdg %	σ_y^{-C} MPa	$\sigma_b^{-B:-C}$ wk hdg %
Aluminum	62	79	6%	84	7%
Solid Solution	160	315	7.1%	350	5.1%
Peak Aged	210	370	8.4%	410	5.2%
Over Aged	160	200	38%	220	38%

SUMMARY OF RESULTS

The microstructures of each material have been observed primarily at large strains. Pure aluminum has the lowest flow stress and the lowest θ at high strains of all the materials studied. This material also has the most well developed cellular microstructure and the largest λ^S. The physical characteristics of the cells will change as the material deforms. This has not been measured in detail here.

The solid solution of Al 3.6 wt% Cu has the highest work hardening rate at large strains (>100 MPa at $\varepsilon = -0.5$), but also has the least developed microstructure.

Peak aged Al-Cu contains small deformable particles, work hardens at a lower rate than (<100 MPa at $\varepsilon = -0.5$) and has a similarly poorly developed microstructure as the solid solution.

The overaged Al-Cu contains relatively large "non deformable" plates. At large strain, the work hardening rate is similar to that of the pure aluminum. The microstructure is well developed, particles forming part of the cell walls. At strains greater than ε_A=-0.45 some precipitates are cut.

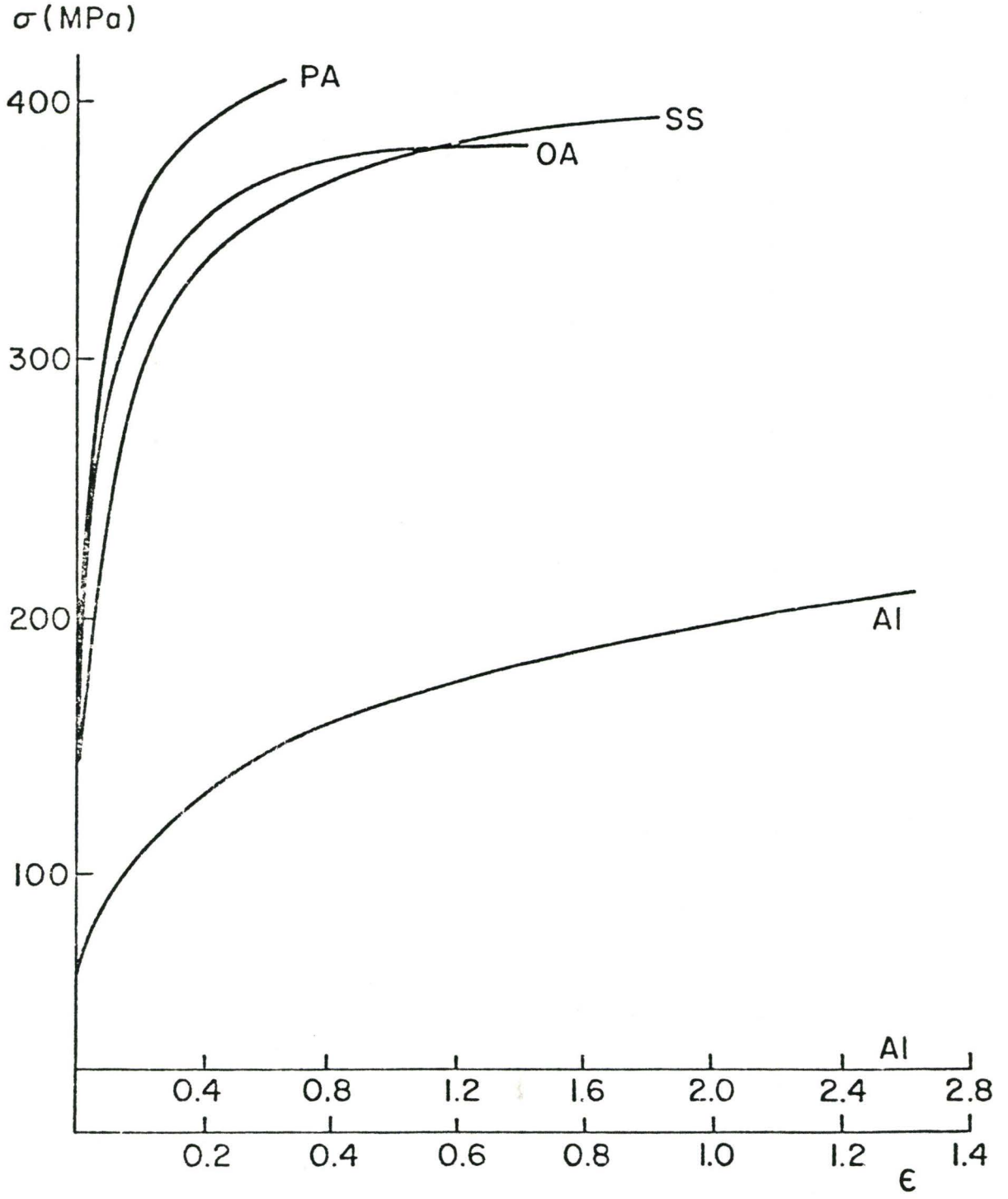

FIGURE 4.1 Tensile Stress versus Strain Curves

Al; Aluminum
SS; Solid solution
PA; Peak aged
OA; Overaged

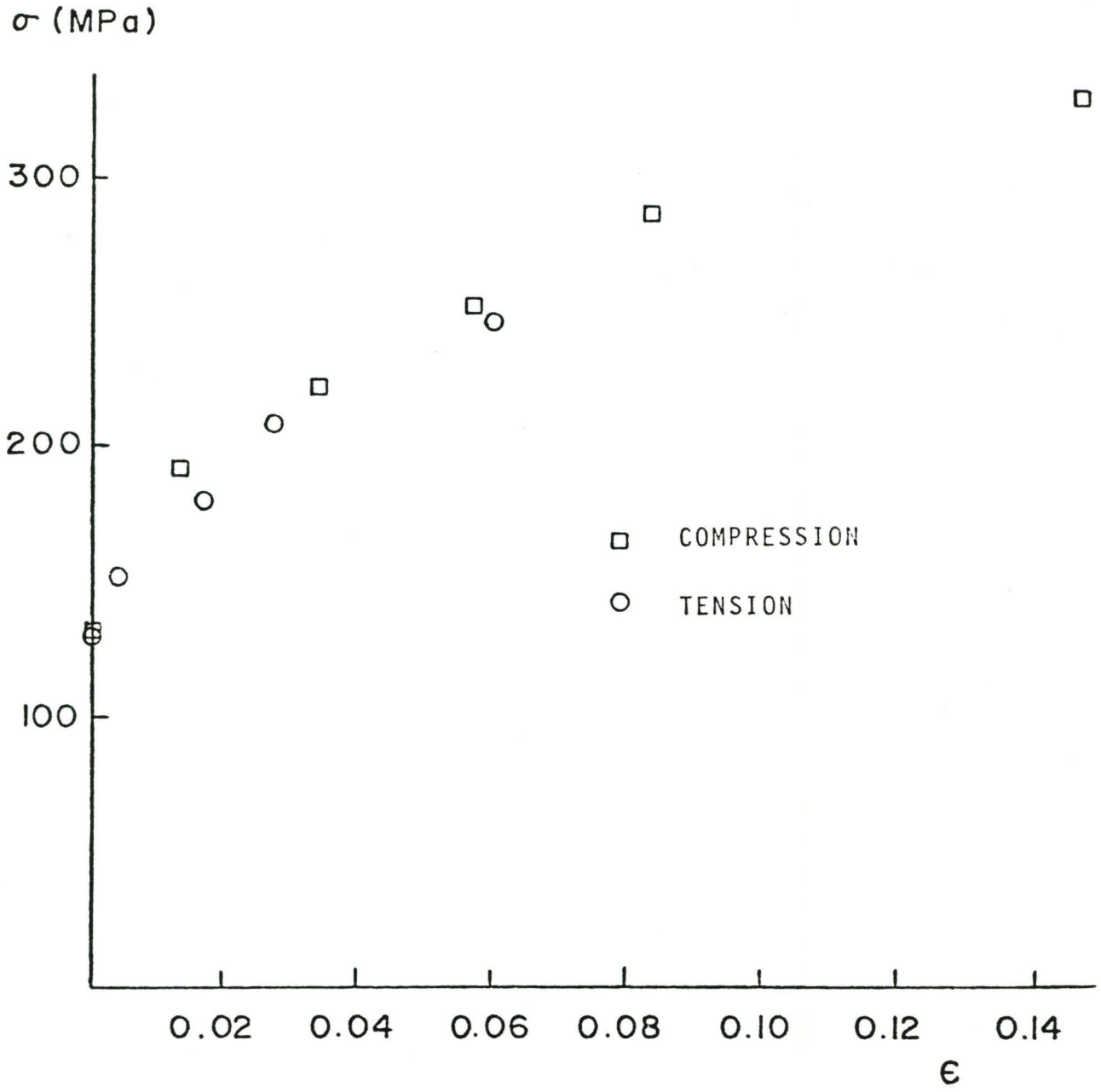

FIGURE 4.2 Comparison of Results in Tension and Compression

The above is a plot of stress versus strain at low strains for Al-Cu in the solid solution condition.

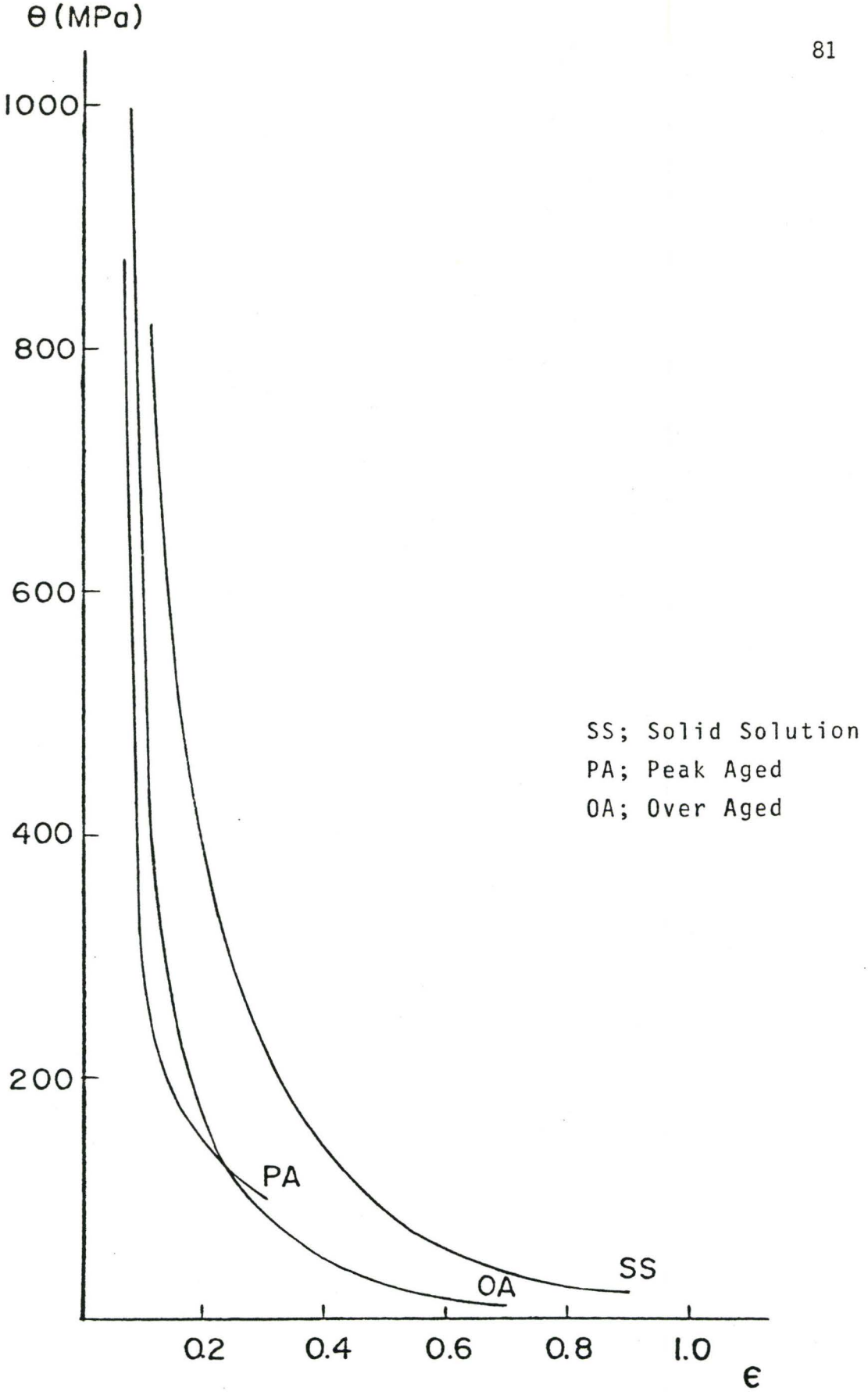

FIGURE 4.3 Work Hardening Rate versus Strain

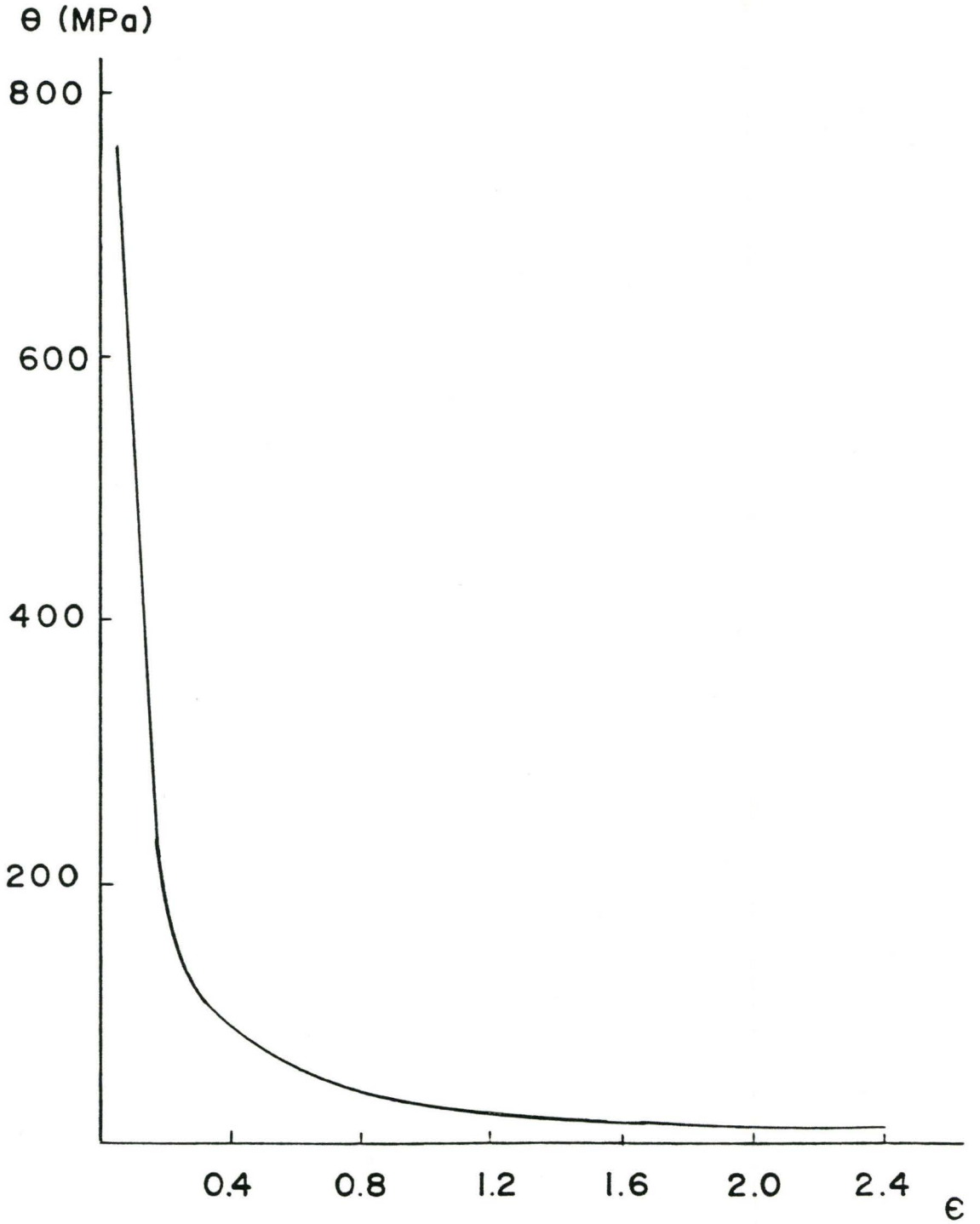

FIGURE 4.3 Work Hardening Rate versus Strain

Aluminum

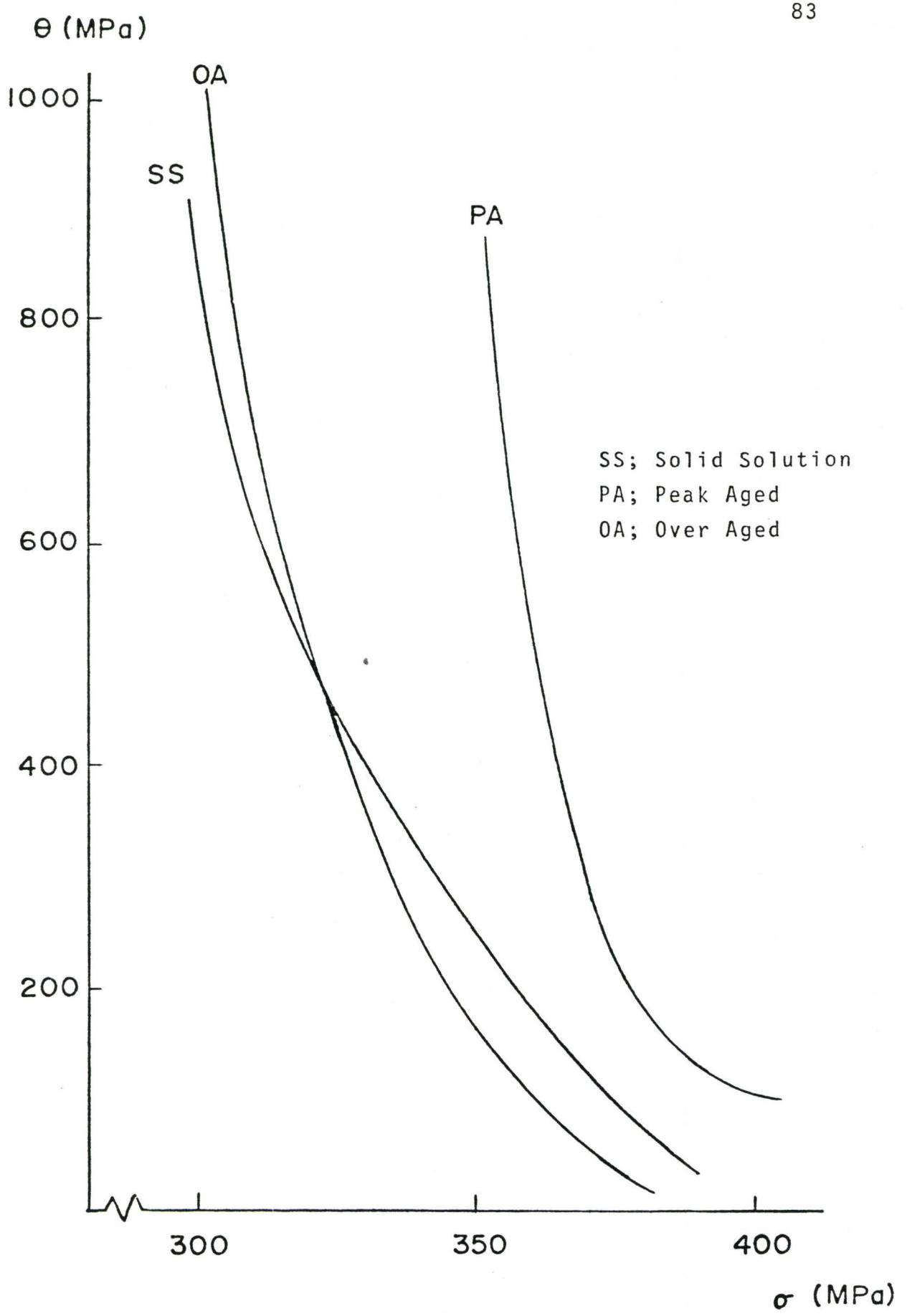

FIGURE 4.4 Work Hardening Rate versus Stress

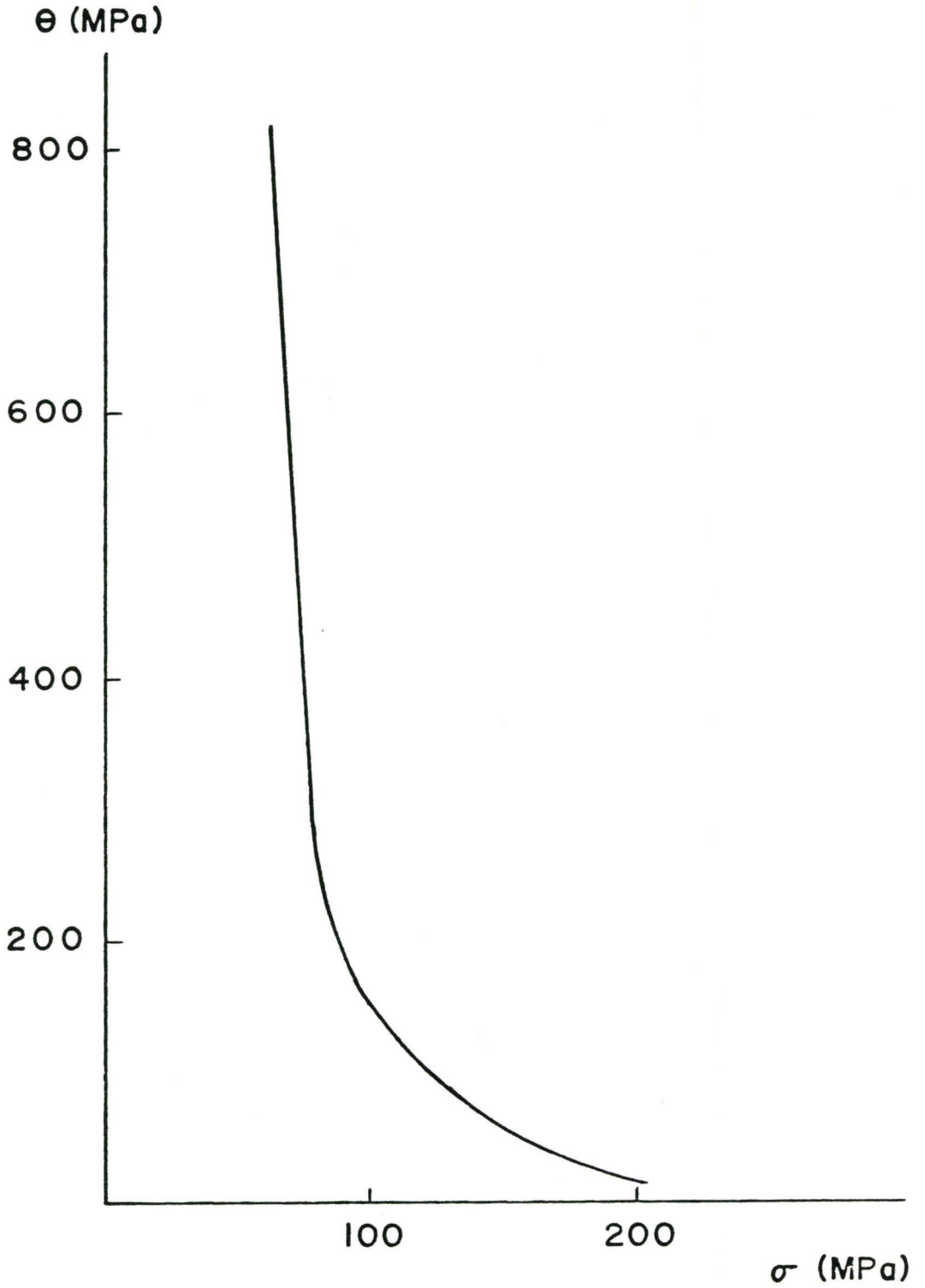

FIGURE 4.4 Work Hardening Rate versus Stress

Aluminum

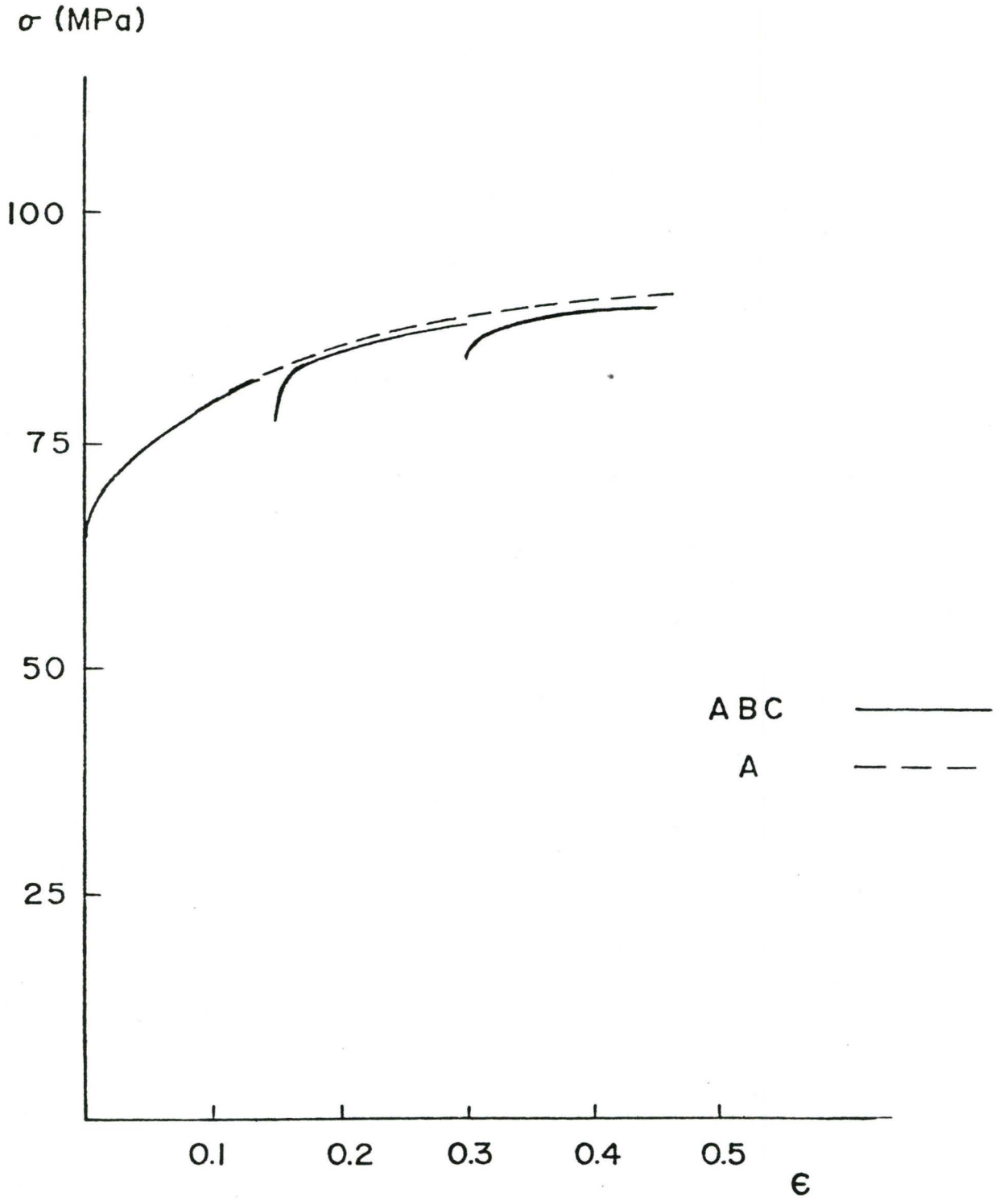

FIGURE 4.5 Stress versus Strain: Pure Aluminum

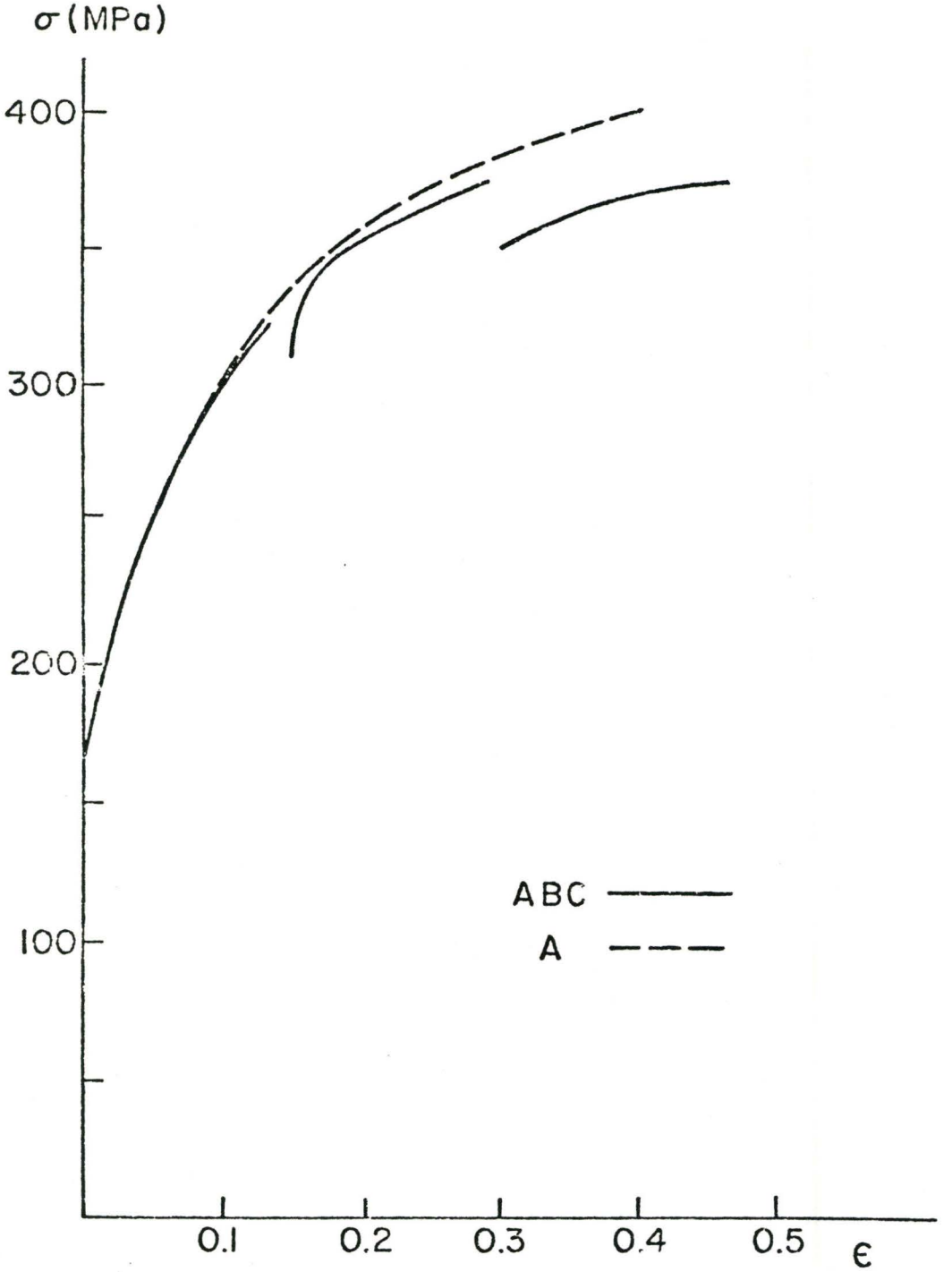

FIGURE 4.6 Stress versus Strain: Al 3.6% Cu Solid Solution

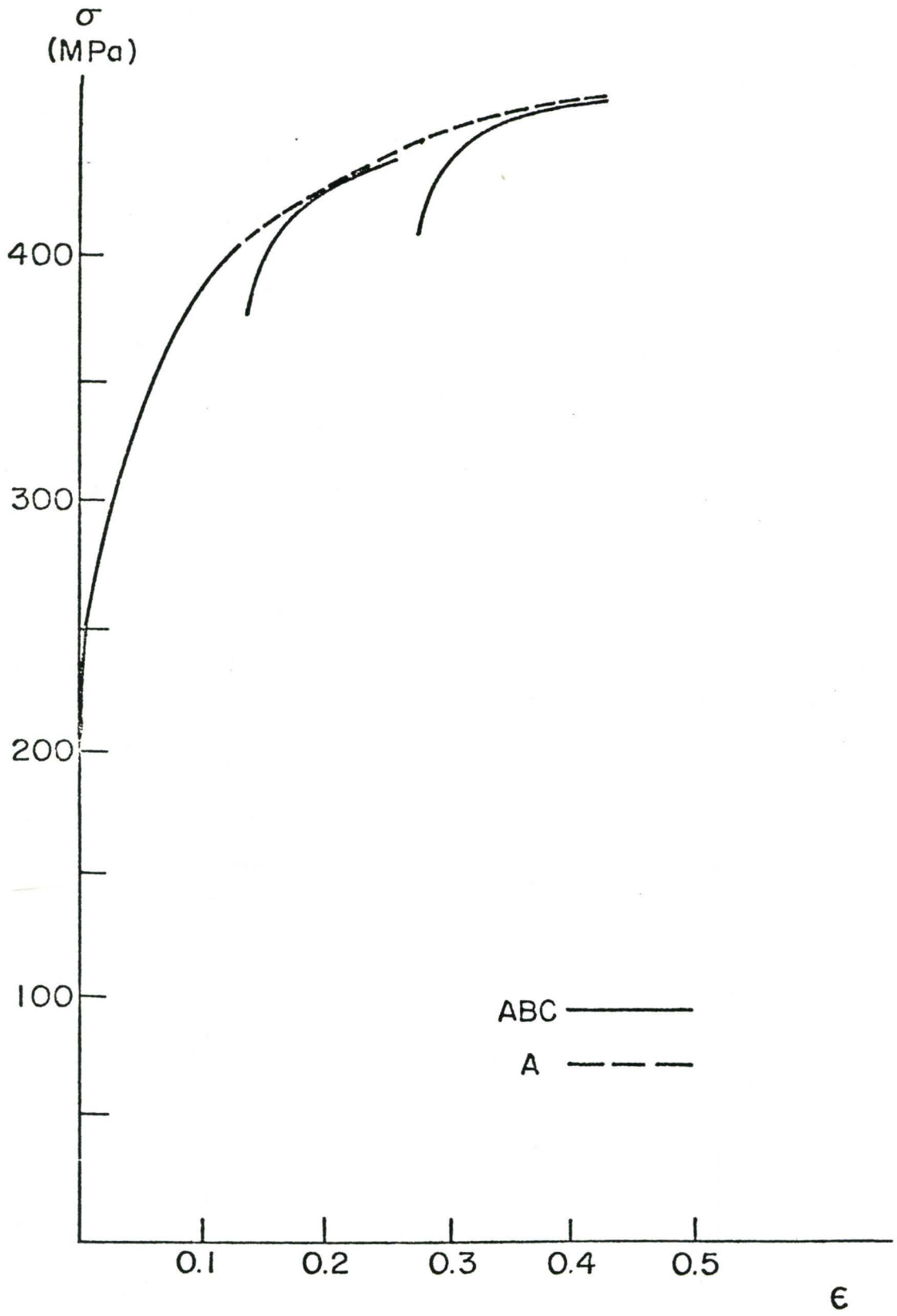

FIGURE 4.7 Stress versus Strain: Al 3.6% Cu
Peak Aged

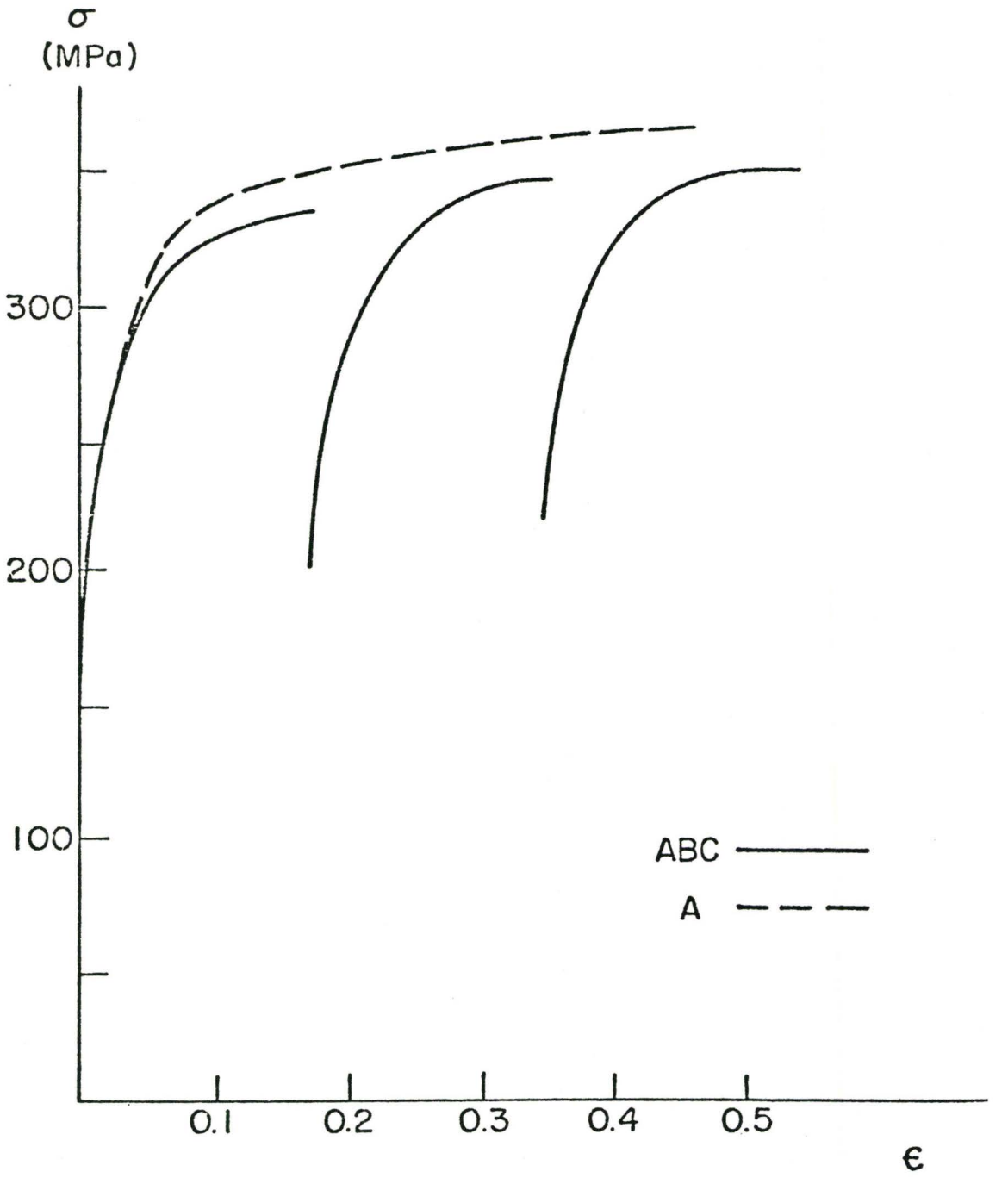

FIGURE 4.8 Stress versus Strain: Al 3.6% Cu Overaged

FIGURE 4.9 Fracture Surface: Aluminum

Pure Aluminum pulled in uniaxial tension at room temperature. Magnification; 25μ marker

FIGURE 4.10 Fracture Surface: Solid Solution

Al 3.6 wt% Cu Solid Solution pulled in uniaxial tension at room temperature.
Magnification; 25μ marker

FIGURE 4.11 Fracture Surface: Peak Aged

Al 3.6 wt% Cu Peak Aged pulled in uniaxial tension at room temperature.
Magnification; 25μ marker

FIGURE 4.12 Fracture Surface: Over Aged

Al 3.6 wt% Cu Over Aged pulled in uniaxial tension at room temperature.
Magnification; 25μ marker

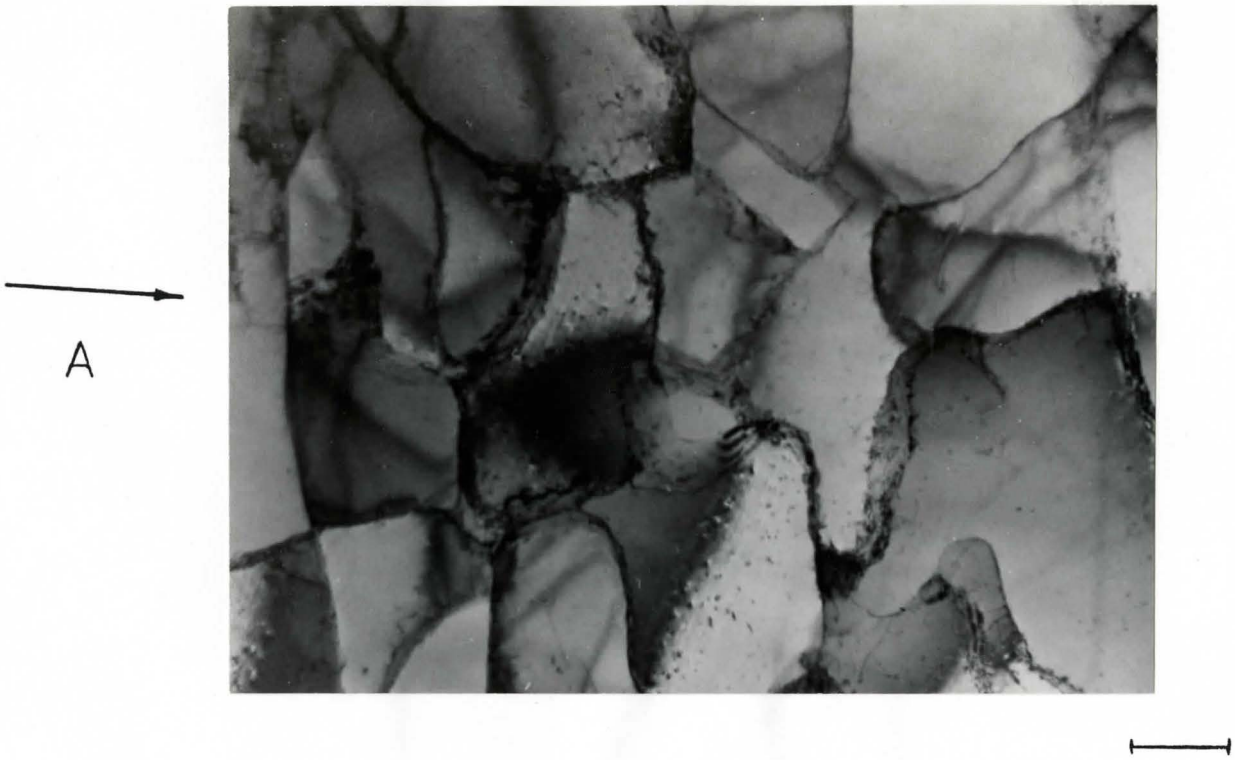

FIGURE 4.23 Pure Aluminum: $\varepsilon_A = 0.38$

Magnification: 26000 x (0.5μ marker)

FIGURE 4.25 Pure Aluminum: $\varepsilon_A = 0.45$

Magnification: 5,900 x (0.5 μ marker)

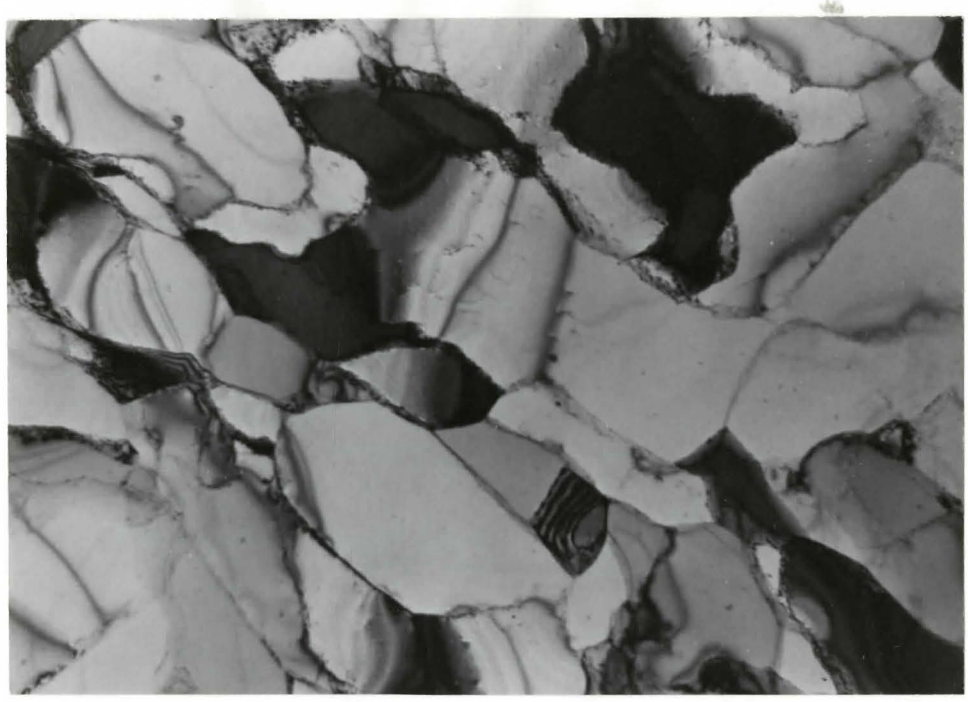

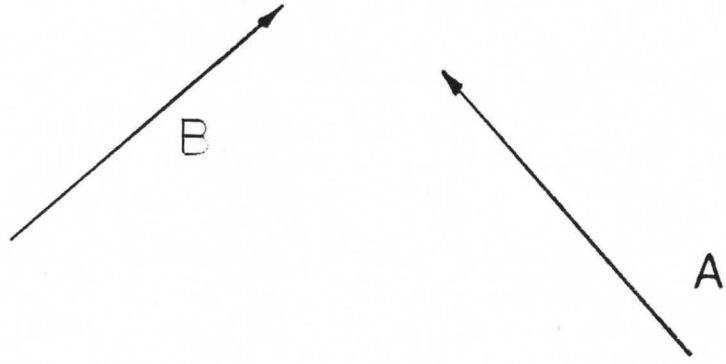

FIGURE 4.26 Pure Aluminum: $\varepsilon_A = 0.45$ plus $\varepsilon_B = 0.45$

Magnification: 15,700 x (0.5μ marker)

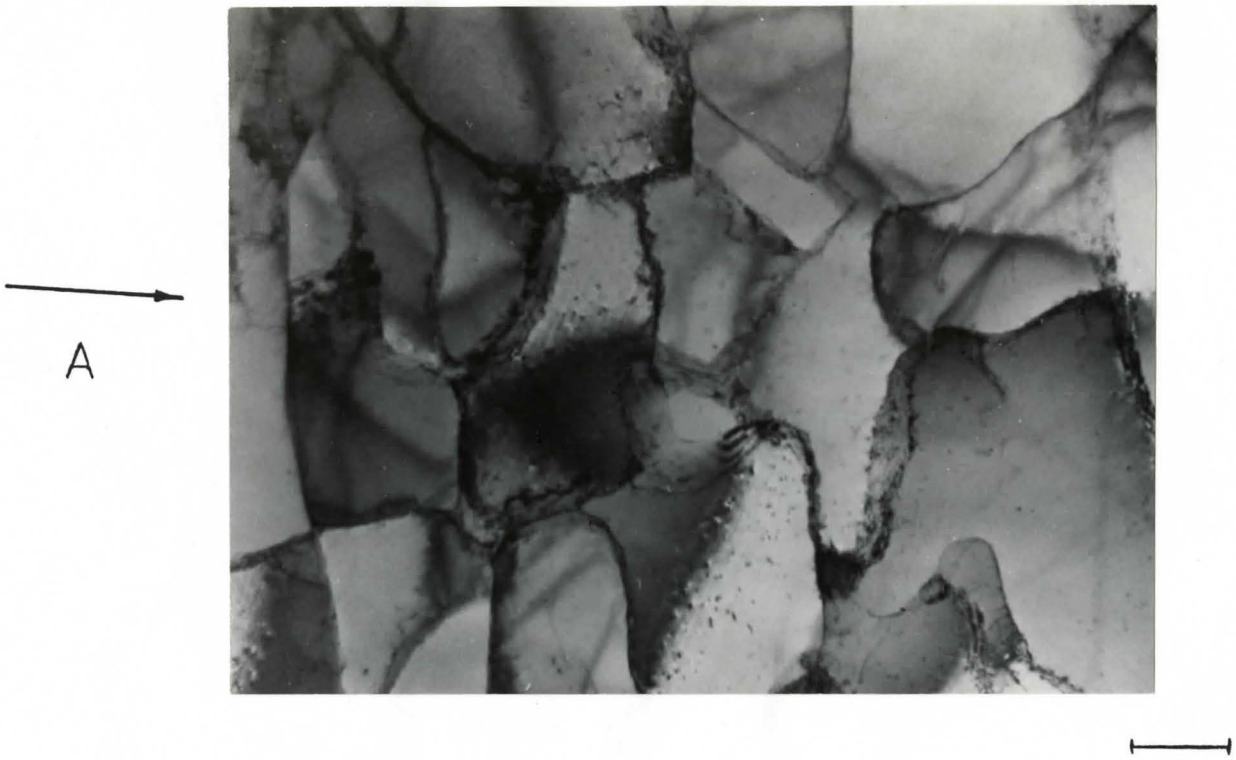

FIGURE 4.23 Pure Aluminum: $\varepsilon_A = 0.38$

Magnification: 26000 x (0.5μ marker)

FIGURE 4.25 Pure Aluminum: $\varepsilon_A = 0.45$

Magnification: 5,900 x (0.5 μ marker)

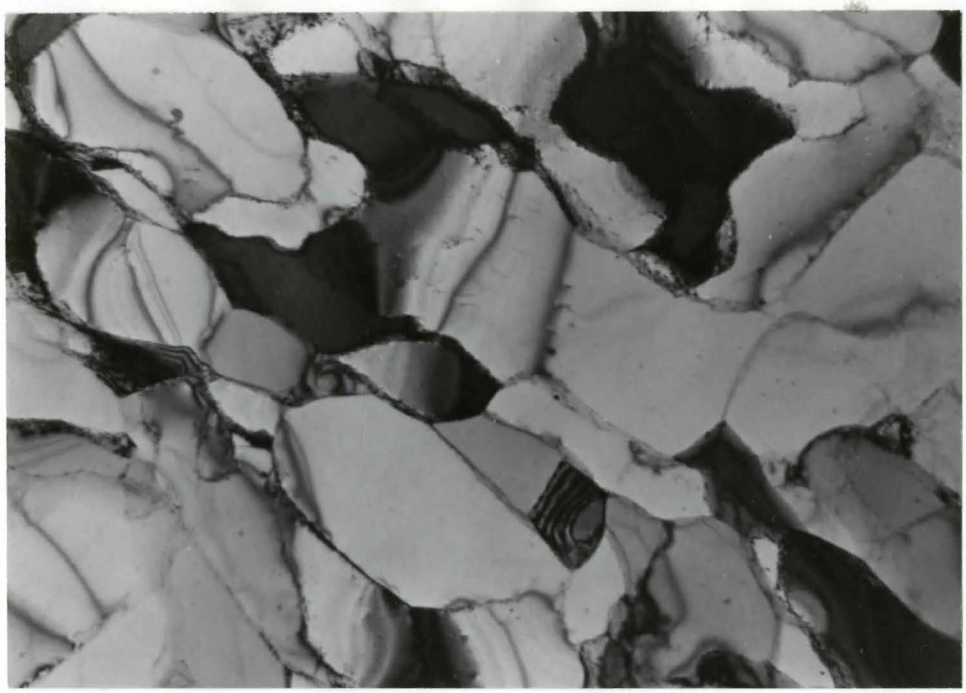

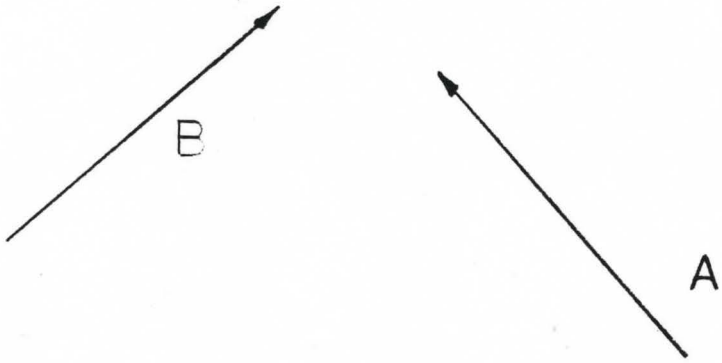

FIGURE 4.26 Pure Aluminum: $\varepsilon_A = 0.45$ plus $\varepsilon_B = 0.45$

Magnification: 15,700 x (0.5μ marker)

FIGURE 4.35 Al-Cu Solid Solution: $\varepsilon_A = 0.45$

Magnification: 15,400 x (0.5μ marker)

FIGURE 4.36 Al-Cu Solid Solution: $\varepsilon_A = 0.45$ plus $\varepsilon_B = 0.45$

Magnification: 24,300 x (0.5μ marker)

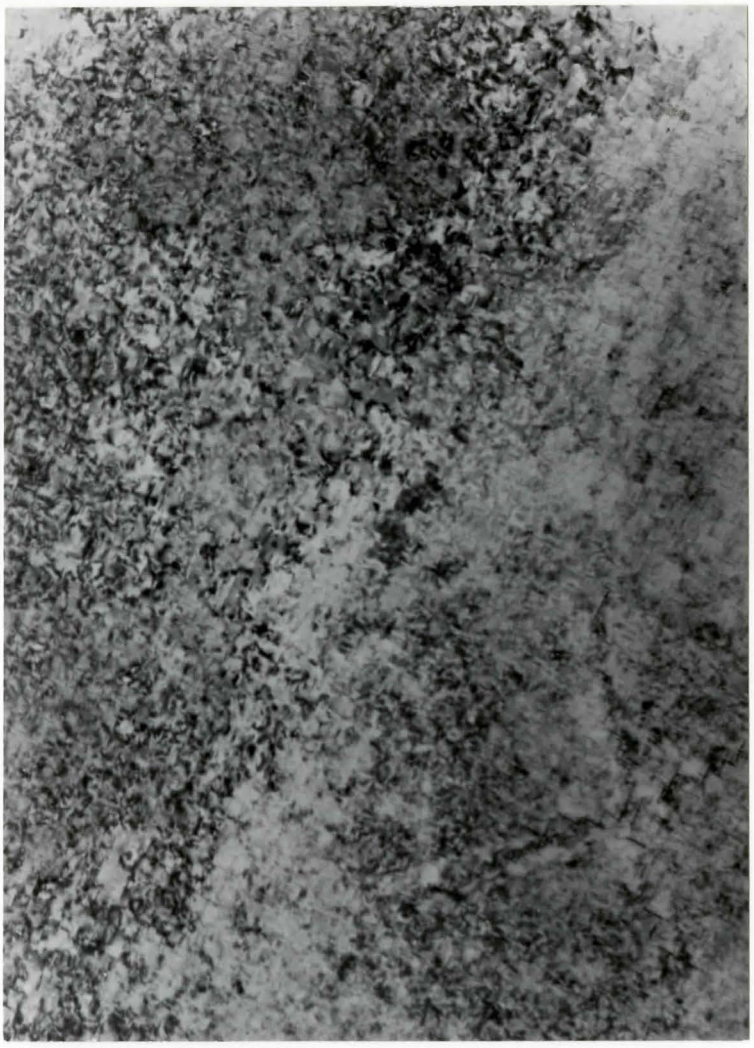

FIGURE 4.41 Peak Aged Al-Cu: Prior to Deformation
Magnification: 68400 x (0.1μ marker)

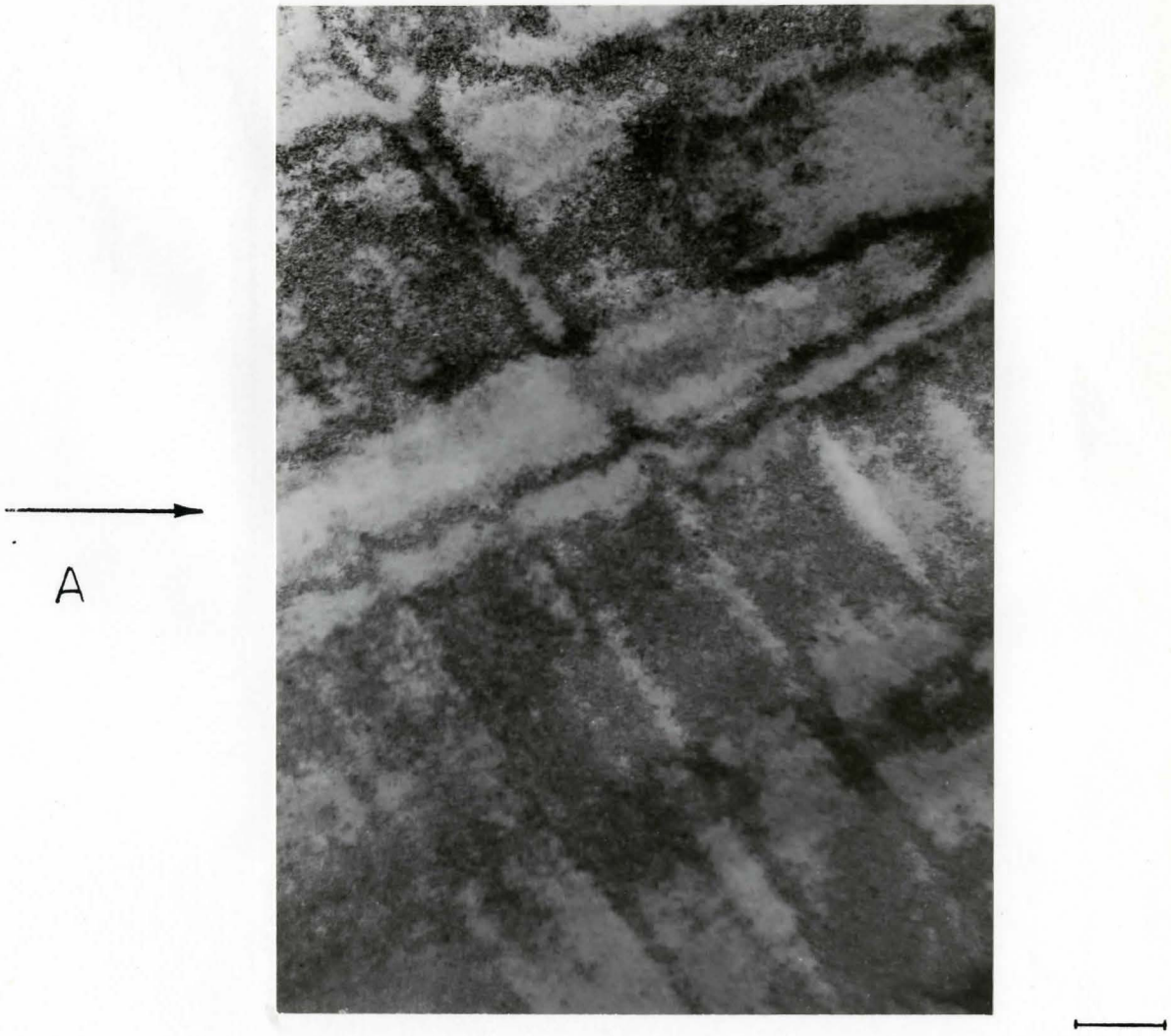

FIGURE 4.43 Peak Aged Al-Cu: $\varepsilon_A = 0.38$

Magnification: 24300 x (0.5μ marker)

FIGURE 4.45 Peak Aged Al-Cu: $\varepsilon_A = 0.45$

Magnification: 75,000 x (0.1μ marker)

FIGURE 4.46 Peak Aged Al-Cu: $\varepsilon_A = 0.45$ plus $\varepsilon_B = 0.45$

Magnification: 15,500 x (0.5μ marker)

FIGURE 4.51 Over Aged Al-Cu: Prior to Deformation
Magnification: 6,700 x (0.5μ marker)

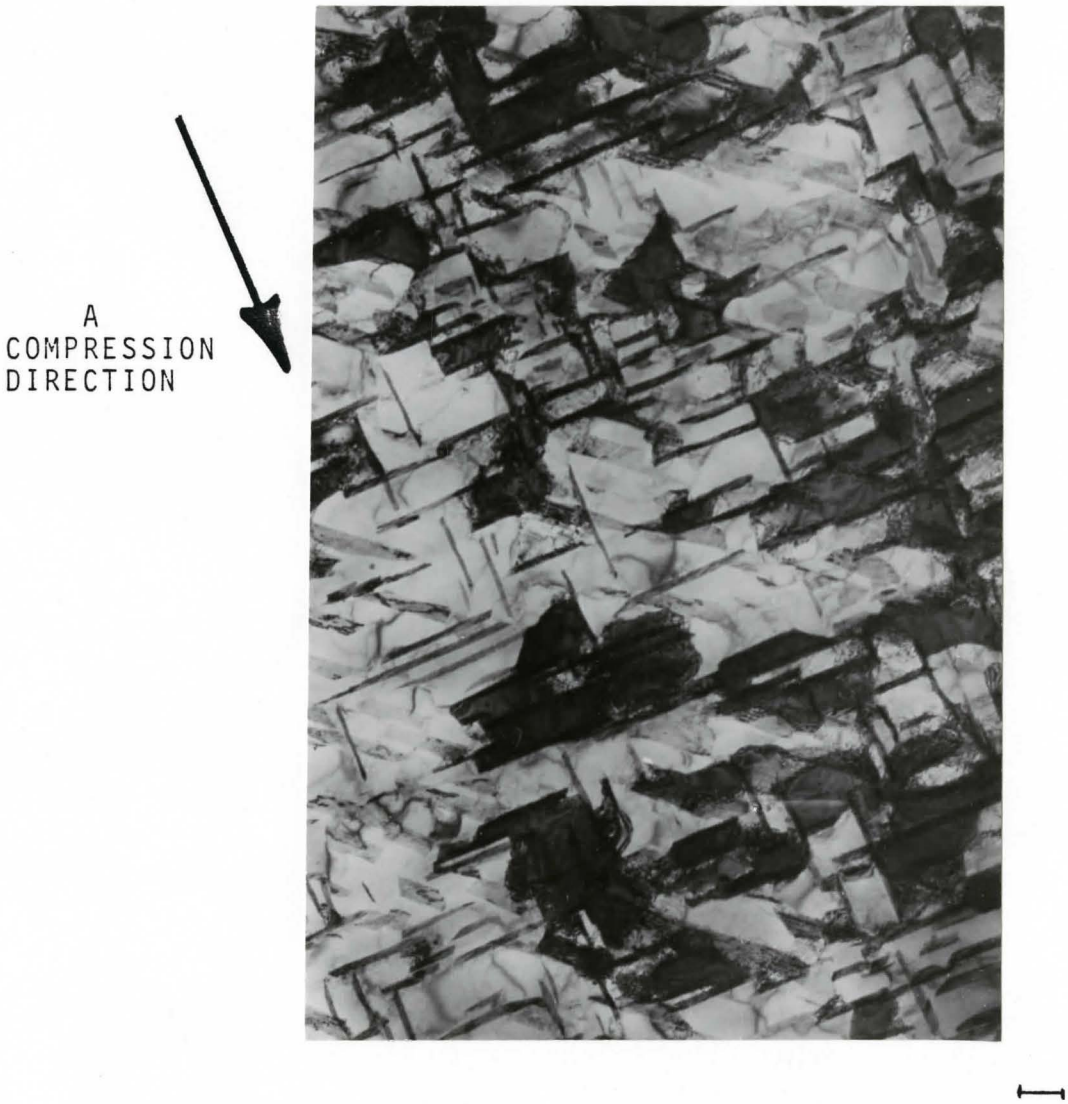

FIGURE 4.52 Over Aged Al-Cu: $\varepsilon_A = 0.18$

Magnification: 12,000 x (0.5μ marker)

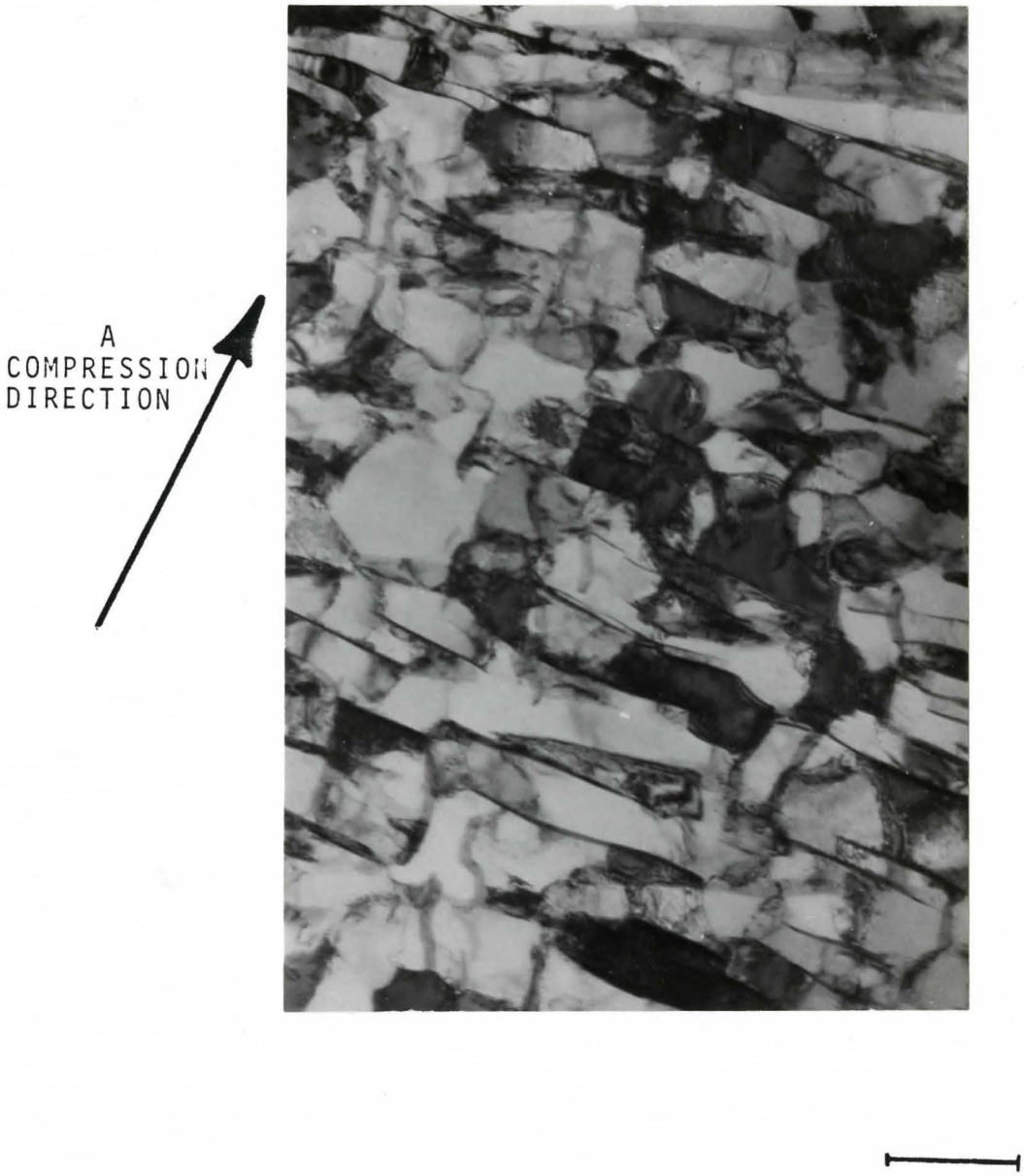

FIGURE 4.54 Over Aged Al-Cu: $\varepsilon_A = 0.54$

Magnification: 37,200 x (0.5μ marker)

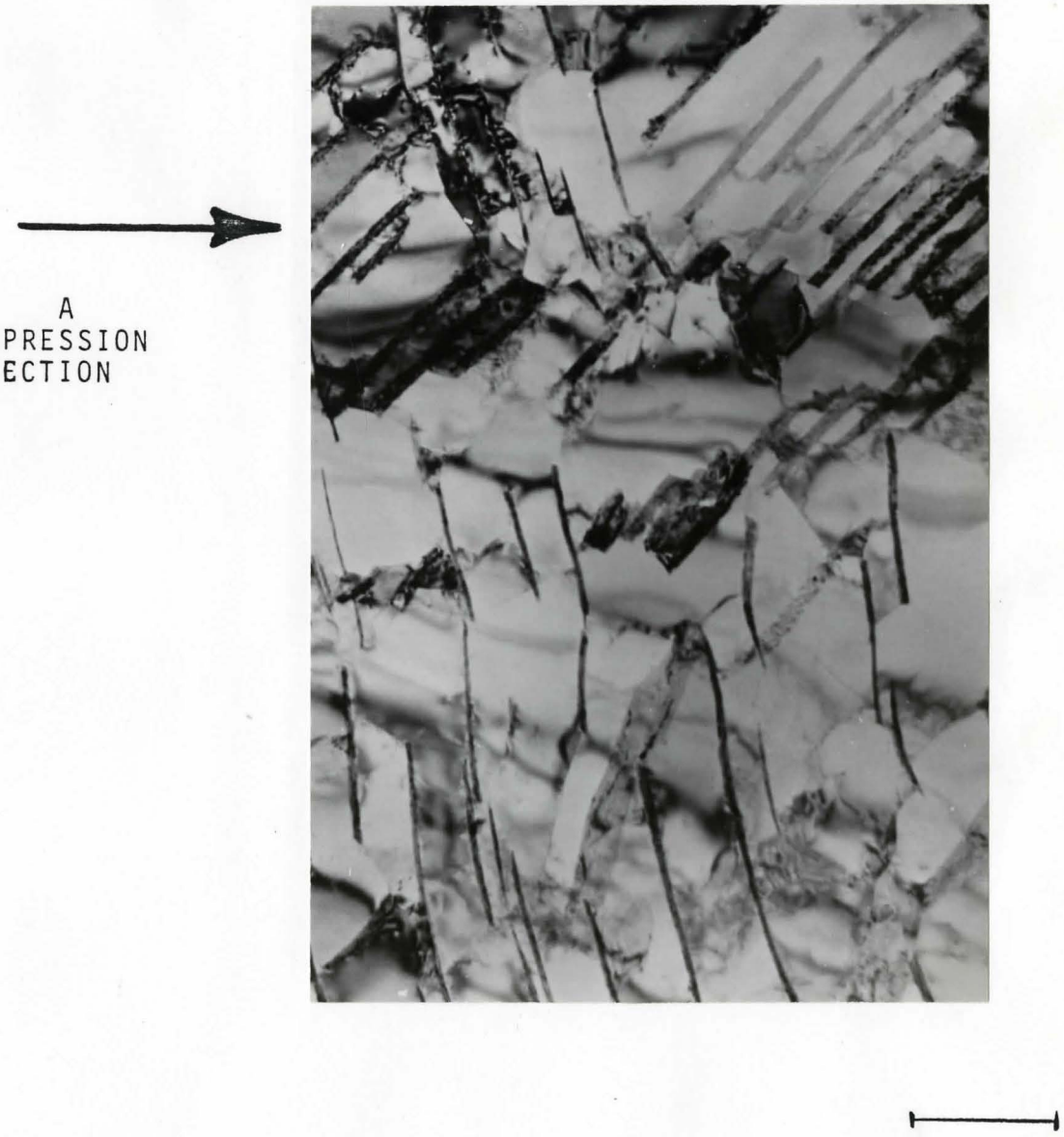

FIGURE 4.55 Over Aged Al: $\varepsilon_A = 0.45$

Magnification: 39,500 x (0.5μ marker)

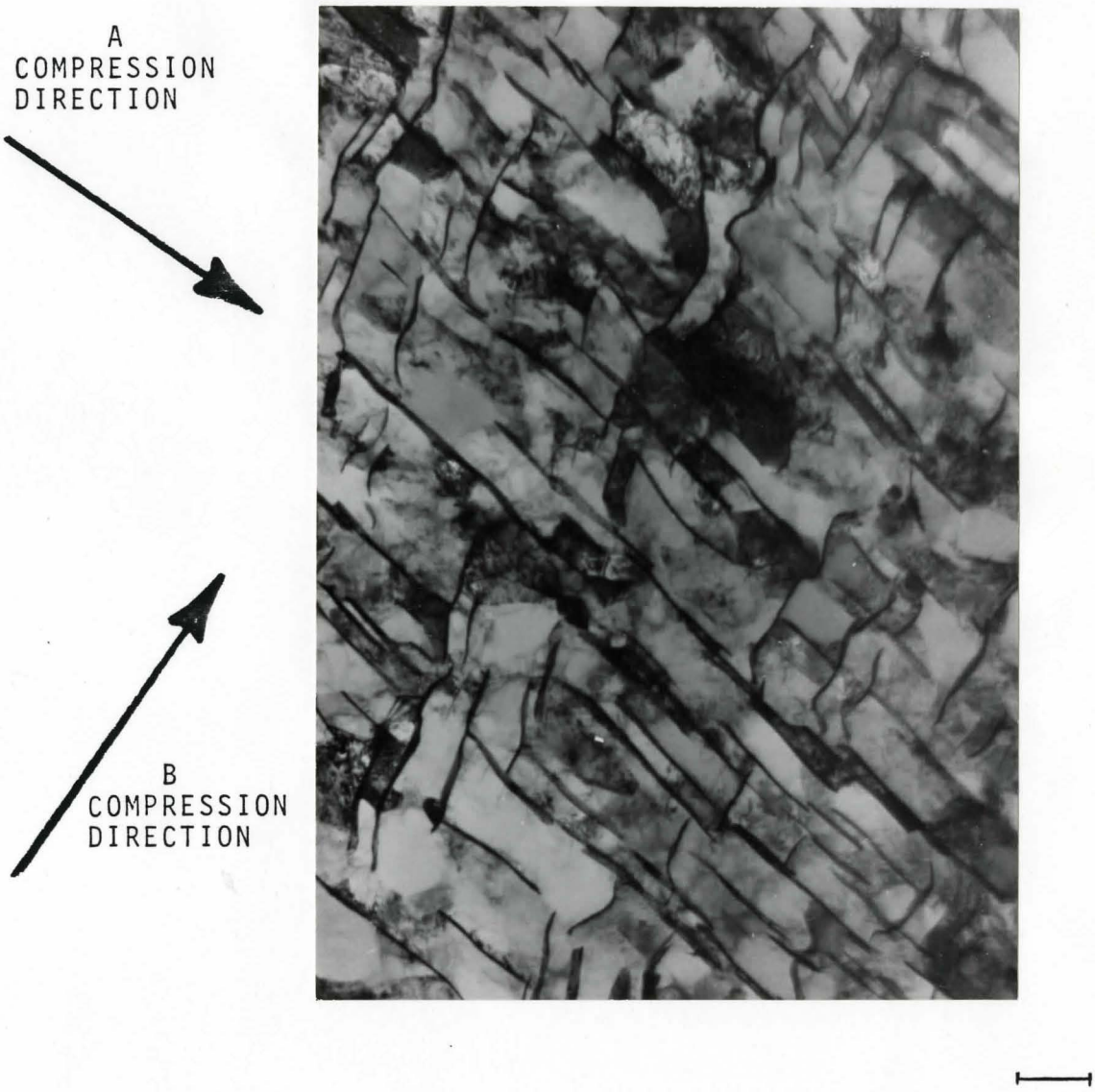

FIGURE 4.56 Over Aged Al-Cu: $\varepsilon_A = 0.45$ plus $\varepsilon_B = 0.45$

Magnification: 21,000 x (0.5μ marker)

FIGURE 4.60 Over aged Al-Cu: $_A$ = 0.54

Magnification:

CHAPTER 5

DISCUSSION

The purpose of the current work was to compare the plastic behaviour of Aluminum with that of Al-Cu subjected to various heat treatments. The work also attempts to characterise the fracture modes, of each of the material conditions under study, in relation to the strain history of the material. This discussion will concentrate on the salient features of the observed plastic behaviour and, for the sake of clarity, will be divided into the following sections.

5.1 Monotonic Loading Behaviour

5.2 Subsequent Yield Surfaces

5.3 Fracture Characteristics

5.4 Fracture Maps

5.1 Monotonic Loading Behaviour

As summarized in Table 4.1, σ_y and the initial work hardening rate reflect the initial microstructural characteristics of the materials under study. The basic characteristics of the initial mechanical behaviour of each material in response to monotonic loading (both in tension and in compression) were presented in detail in Chapter 4. These characteristics will now be discussed in relation to each initial microstructure and the changes in the dislocation

substructures which develop with imposed strain.

The yield strength, or initial flow stress, of a material is the stress which marks the beginning of general plastic deformation, i.e. dislocations begin to move and interact across the total cross section of the material. In a single crystal, the stress at which the material begins to flow can be predicted using models based on the presence of a unique set of obstacles (Brown and Ham, 1971). The models relate the yield strength of the crystal to the scale of and the strength of the obstacle type assumed present. This is a relatively simple mathematical relationship in the case of a single crystal containing a single type of obstacle. In the case of a polycrystalline alloy containing more than one strengthening agent, the required analysis is more complex. The method of adding the effects of the obstacles is not clear. Simple linear additivity can be assumed in order to make an estimate of the yield strength, but the result is only a crude approximation.

An example of this type of linearly additive model is shown in equation [5.1].

$$\sigma_y = \sigma_i + kd^{-\frac{1}{2}} + kc^{\frac{1}{2}} + \frac{\mu b}{\lambda} \qquad [5.1]$$

σ_i is the friction stress opposing dislocation motion, the second term accounts for strengthening due to grain size d. $kc^{\frac{1}{2}}$ includes the effects of the solid solution and $\frac{\mu b}{\lambda}$ is an additional term, for the overaged material, to account for

the presence of large $CuAl_2$ plates.

Pure aluminum has the lowest yield strength of the materials in this study, $\frac{E}{1250}$. For Aluminum, equation [5.1] reduces to $\sigma_y = \sigma_i + kd^{-\frac{1}{2}}$, where d is the initial grain size. k and σ_i may be determined from a plot of σ_y versus $d^{-\frac{1}{2}}$. The role of grain size was not considered in the present study. The results are known; σ_i = 16 MPa for pure aluminum and k = 2.2 MPa $mm^{\frac{1}{2}}$ (Embury, 1971).

The solid solution and overaged materials have similar yield strengths, $\sim\frac{E}{430}$. In the case of the solid solution equation [5.1] can be rewritten $\sigma_y = \sigma_i + kd^{-\frac{1}{2}} + kc^{\frac{1}{2}}$. The overaged material, assuming it contains coarse $CuAl_2$ precipitates only (no shearable zones or solute atoms) will have a yield stress, $\sigma_y = \sigma_i + kd^{-\frac{1}{2}} + \frac{\mu b}{\lambda}$. The relative magnitudes of σ_y for the solid solution and overaged materials depend on the extent of ageing.

The peak aged Al-Cu has the highest yield stress, $\frac{E}{360}$, as expected since it contains the "optimum" distribution of obstacles to dislocation motion. Equation [5.1] for the peak aged material (again assuming no Cu atoms are left in solution) is $\sigma_y = \sigma_i + kd^{-\frac{1}{2}} + \frac{\mu b}{\lambda}$. λ is smaller for the peak aged material than for the overaged. $\sigma_y = \frac{E}{360}$ is consistent with $\frac{E}{350}$ for an Al 3.7 wt% Cu single crystal (solution treated and then aged at 165°C for two days) reported by Price and Kelly (1964).

After yielding the material begins to work harden.

The observed rate of work hardening depends both on the mechanisms of dislocation accumulation and the rate of thermal and dynamic recovery processes which lead to dislocation annihilation. In order to compare rates of hardening it is useful to refer to the measured rates of Stage II hardening, θ_{II}, in the literature. $\theta_{II} = \frac{\mu}{K}$ where $K \cong 300$ for most materials. K is nearly independent of strain rate, temperature and orientation (Kuhlmann-Wilsdorf, 1968).

During Stage II hardening, one assumes that the mechanisms of dynamic recovery are not yet active and the dislocation density is directly proportional to the square of the strain (van den Beukel, 1971). Thus the flow stress varies linearly with strain.

However in aluminum polycrystals tested at room temperature the flow curves are in the Stage III region in which extensive dynamic recovery occurs. In the present work when initial rates of work hardening are compared , the over aged material has the highest work hardening rate at low strain, pure aluminum the lowest, with the solid solution having a value somewhere in between.

The differences in work hardening rates can be related to the differences in the microstructures of each of the materials, since θ is directly related to the rate of dislocation storage. Bergstrom (1969) presented a dislocation model for the stress strain behaviour of α iron in which he determined the dislocation density

as a function of strain. The basis of the model is expressed in equation [5.2] ;

$$\frac{d\rho}{d\varepsilon} = \frac{dc}{d\varepsilon} - \frac{da}{d\varepsilon} = U - \frac{dr}{d\varepsilon} - \frac{da}{d\varepsilon} \qquad [5.2]$$

where U is a measure of the rate at which the density of mobile dislocations is increased by creation and or remobilization, $\frac{dc}{d\varepsilon}$ is the rate of creation of new dislocations, $\frac{dr}{d\varepsilon}$ is the rate of remobilization of immobile dislocations and $\frac{da}{d\varepsilon}$ is the rate of annihilation of mobile and immobile dislocations.

ρ_m is assumed to be constant, and therefore U may also be interpreted as the rate at which dislocations are immobilized and annihilated. U is directly related to the mean free path of the mobile dislocations, s (equation [5.3]).

$$U(\varepsilon) = \frac{v\ \rho_m}{s(\varepsilon)} \qquad [5.3]$$

Thus the strain dependence of s will determine the strain dependence of U. Though s is known to vary with strain, Bergstrom (1969) assumed that s,and therefore U, were strain independent. For the purpose of discussion of the results of the present study it has been assumed that s, the mean free path of a mobile dislocation, is indeed independent of strain. Assuming that the mean free path is proportional to the cell diameter of the microstructure, Bergstrom's model implies that U is smaller for pure aluminum and overaged Al-Cu than

for the peak aged Al-Cu and the solid solution condition.

Bergstrom (1969) assumed that the annihilation of dislocations could occur by the following processes:

- the interaction of two mobile dislocations,

  $\propto \rho_m^2$

- the interaction between a mobile and an immobile dislocation

  $\propto \rho_m \rho_i$

- the interaction of a mobile dislocation with a specimen surface, grain boundary, cell wall or large precipitate.

  $\propto N\rho_m$

$N\rho_m$ will be largest for the aluminum and overaged material thus increasing the rate of annihilation of dislocations in these two materials. This result is consistent with equation [5.3].

It was also assumed that $\frac{dr}{d\varepsilon}$ is directly proportional to the density of immobile dislocations, ρ_i. By combining these terms Bergstrom (1969) obtained an expression for the change in the total dislocation density, ρ, with strain. (Equation [5.4]).

$$\frac{d\rho}{d\varepsilon} = U(\varepsilon) - A - \Omega\rho \qquad [5.4]$$

A and Ω are strain independent constants. Ω represents the probability of remobilization and annihilation of a dislocation by the interaction of a mobile dislocation with an immobile dislocation: $\Omega << 1$.

$A = (\lambda_1 - \lambda_2)\ _m - (\theta_2 N - \theta_1)\ _m{}^*$, where θ_1, θ_2, λ_1, and λ_2 are strain independent constants. This implies that there are the least number of immobile dislocations in the pure aluminum material and the overaged alloy, consistent with the limited microstructural evidence of the present study. Equation [5.4] leads to a stress strain relationship, given in equation [5.5] below.

$$\sigma = \sigma_{io} + \alpha\mu b\{\frac{U - A}{\Omega}(1 - e^{\Omega\varepsilon}) + \rho_o\varepsilon^{\ \Omega\varepsilon}\}^{\frac{1}{2}} \qquad [5.5]$$

It must be noted that the model is restricted because of the number of assumptions made. However, it is still useful in describing the behaviour of a material experiencing homogeneous deformation. The model (Bergstrom, 1969) is based on the average behaviour of large numbers of dislocations. The general implications of the model are consistent with the results of the present study, which includes several materials with very different microstructures. In summary, assuming ρ_m to be constant and the same for each material, ρ_i is found to be greater for the peak aged Al-Cu and the solid solution condition. $\frac{da}{d\varepsilon}$ is said to vary with the density of large precipitates and cell walls such that

---

* N represents a strain independent density of annihilation places other than dislocations, i.e. $CuAl_2$ plates or cell walls.

it is larger for the overaged Al-Cu and the pure aluminum. s, the mean free path of a dislocation, is said to be related to the cell size and U is inversely proportional to s. The present work did not include measurements of dislocation densities; thus no numerical comparison of total dislocation densities in the four materials is possible other than by the comparison of their work hardening characteristics. However Bergstrom and Roberts (1971) found the model to be consistent with the tensile properties of α-iron (polycrystalline).

The materials studied in the present work each contain different types and mixtures of obstacles. The aluminum contains a few large inclusions but no precipitates and few solute atoms. The solid solution contains a few inclusions and a high concentration (3.6 wt%) of solute atoms. The peak aged material contains small metastable precipitates (0.01-0.02μ) and the overaged material contains $CuAl_2$ plates (~1μ) in three different orientations.

As previously discussed each of these types of obstacles affect the initial yield stress. They also affect the work hardening history of the material. The hard "non deforming" $CuAl_2$ precipitates present in the overaged material have the most striking effect on the work hardening history. These plates make the alloy plastically non-homogeneous, by changing the way in which slip is distributed, and dislocations are accumulated throughout the material. In other words, initially no slip occurs within the plates,

thus producing large microscopic gradients of strain in the region of the particles. Dislocations will therefore accumulate for two reasons; geometric compatibility and because they are trapped by one another in a random fashion. The former are referred to as 'geometrically necessary'; the latter are 'statistically stored' (Ashby,1971). It is the geometrically necessary dislocations which primarily account for the higher initial work hardening rate in the overaged material at low strains. This is not true in the peak aged and solid solution materials where no geometrically necessary dislocations are accumulated. In a material containing 'non-deformable' particles approximately one micron apart, $\rho^G = 10^{11} cm/cm^3$ after 10% shear strain is a typical value. In a material containing no 'non-deformable' particles, $\rho^S = 10^{8 \text{ or } 9} cm/cm^3$ after the equivalent amount of strain (Ashby,1971). The two dislocation densities are expressed below in equations [5.6] and [5.7].

$$\rho^G = \frac{1}{\rho} \frac{4\gamma}{b} \qquad [5.6]$$

$$\partial\rho = \frac{1}{\lambda^S} \frac{4\partial\gamma}{b} \qquad [5.7]$$

λ^S is the slip distance. Therefore, at low strains we can approximate the flow stress of the overaged material with the following expression (Ashby, 1971);

$$\sigma = \sigma^o + \alpha\mu\left(\frac{V_f}{2r_o} b\varepsilon\right)^{\frac{1}{2}} \qquad [5.8]$$

Equation [5.8] assumes spherical particles, and no back stress build-up during deformation. Using the following values of each parameter :

σ^o = 158 MPa

α = 0.25

μ = 27600 MPa

V_f = 0.045

ε = 0.025

b = 0.0286

$2r_o$ = 1μ

we get σ = 197 MPa. This is significantly lower than the measured value from these experiments due in part to the elastic back stress and particle shape effect which have both been neglected.

In order to better understand the effects of microstructure on the work hardening behaviour of each of the materials, it is useful to treat the observed work hardening in the following manner,using the treatment developed by Lloyd et al (1978).

The basic premise of the following is that the work hardening rate is related to the rate of accumulation of dislocations minus the rate of annihilation. This can then be expressed in terms of a measurable microstructural feature, the length of dislocation removed per recovery event, L_R, and the relationship between L_R and imposed strain determined. All models of hardening essentially assume that the flow

stress, σ , is directly proportional to the square root of the dislocation density, ρ .

$$\sigma = \alpha\mu b\sqrt{\rho} \qquad [5.9]$$

The other parameters used here are defined below:

L_R - line length of dislocation recovered per recovery event

D - obstacle spacing

$\frac{\partial\sigma}{\partial\varepsilon}$ - this has been previously defined and is not a constant

ρ - total dislocation density

β - arrangement factor, (assumed constant)

α - strength parameter

μ - shear modulus

b - Burger's vector

$\rho\partial\alpha$- number of potential recovery sites.

Using the well established relationship of equation [5.9], we have the following;

$$\frac{\partial\sigma}{\partial\varepsilon} = \alpha\mu b\frac{\partial\sqrt{\rho}}{\partial\varepsilon}$$

$$= \frac{\alpha\mu b}{2\sqrt{\rho}}\frac{\partial\rho}{\partial\varepsilon}$$

and

$$\frac{\partial\rho}{\partial\varepsilon} = \frac{\partial\rho}{\partial\varepsilon}(\text{stored}) - \frac{\partial\rho}{\partial\varepsilon}(\text{recovered}) \qquad [5.10]$$

$$V\partial\rho_{\text{recovered}} = L_R\ \rho\partial a$$

$$\frac{\partial\rho}{\partial\varepsilon} = \frac{\sqrt{\rho}}{\beta b} - \frac{L_R\rho}{b}$$

Therefore,

$$\frac{\partial\sigma}{\partial\varepsilon} = \frac{\alpha\mu b}{2\sqrt{\rho}}\left(\frac{\sqrt{\rho}}{\beta b} - \frac{L_R}{b}\rho\right)$$

which simplifies to,

$$\frac{\partial\sigma}{\partial\varepsilon} = \frac{\alpha\mu b}{2\beta}\left(1 - \frac{\sigma}{\frac{\alpha\mu b}{L_R\beta}}\right) \qquad [\ 5.11\ ]$$

Kocks (1976) assumed that L_R was constant throughout deformation in order to express the above equation [5.11] in the form of equation [5.12].

$$\frac{\partial\sigma}{\partial\varepsilon} = \left(\frac{\partial\sigma}{\partial\varepsilon}\right)_o\left(1 - \frac{\sigma}{\sigma_s}\right) \qquad [\ 5.12\ ]$$

σ_s is the saturation stress at which the hardening rate becomes zero. $\left(\frac{\partial\sigma}{\partial\varepsilon}\right)_o$ from equation [5.12]corresponds to the value of θ at the peak of the $\sigma\theta$ versus σ curve, where Stage III hardening begins. If we plot θ versus σ for Stage III hardening, it takes the form of equation [5.12].

If L_R is assumed to be a constant, directly related to D, the obstacle spacing, then it is possible to treat equation [5.11] in a semi-quantitative way by considering the general shape of each $\frac{\partial\sigma}{\partial\varepsilon}$ versus σ curve presented in figure 4.4, in terms of each microstructure. Table 5.1 contains values of σ_s inferred from figure 4.4.

TABLE 5.1 σ_s Values

Material	D (μ)	σ_s inferred from figure 4.4
Pure aluminum	~1.0	
Al-Cu Solid solution		360 MPa
Al-Cu Peak aged	0.02	380 MPa
Al-Cu Over aged	0.5	330 MPa

σ_s is smaller for materials with the larger values of D. i.e. aluminum and over aged Al-Cu.

However at large strains the value of $\frac{\partial\sigma}{\partial\varepsilon}$ does not decrease to zero, thus the extrapolated values of σ_s shown in Table 5.1 have no physical significance. The departure from linearity and the existence of a linear hardening stage at large strains indicates that L_R is in essence related to the scale of the obstacle structure. In solid solutions L_R is small i.e. the rate of dynamic recovery is low and no cell structure is formed. A similar argument holds for the peak aged material. In the overaged material both the initial dislocation accumulation process and the recovery events must occur in the region of the hard plates of $CuAl_2$.

The reflection of the work hardening behaviour in the microstructural features can now be rationalized. The low work hardening ability of Al exhibited both in monotonic tension and compression is confirmed by the microstructure. The

basic mechanisms active in pure aluminum are dislocation tangling and recovery. The quickly developing cell structure shows that recovery mechanisms are very active.

The solid solution of Cu in Al behaves in a very different manner. The solute atoms are finely dispersed throughout the entire metal matrix and impede dislocation movement, thereby increasing the stress level, $\frac{\partial \rho}{\partial \varepsilon}$ and the work hardening rate relative to pure aluminum. Little recovery occurs even at large strains in the solid solution. As a result, cells do not form easily. This is confirmed by the results in figure 4.3 which show $\theta_{\text{solid solution}}$ is greater than θ_{Al} at high strains. This is consistent with Equation [5.11].

The microstructural development of the peak aged material is similar to that of the solid solution. However in the case of the peak aged material the work hardening rate decreases at higher strains as the zones are cut. $\theta_{\text{peak aged}}$ is larger than $\theta_{\text{over aged}}$ because $\lambda^S > \lambda^G$; the scale of the structure is smaller than the self trapping slip distance for a dislocation.

The over aged material develops a cellular substructure quite readily. This substructure is of the same scale as the interparticle distance. As in the case of the aluminum, $\lambda^G \cong \lambda^S$. In aluminum as strain increases the cell size (and therefore λ^S) decreases (Chandra,1980). In the over aged material as strain increases local stresses are great enough to cause shear of the $CuAl_2$ plates. Therefore as strain in-

creases the ratio of ρ^G to ρ^S decreases and the annihilation processes increase , thereby explaining the low work hardening rate at high strains.

Another effect of the obstacles present which must be considered is how their presence influences the directionality of flow. The results of this study, along with other findings (Wilson, 1965), show that the hard particles have the largest influence on the directionality of flow. The material becomes anisotropic after plastic deformation because of an accumulation of back stress, σ_b, at the obstacles. A term to account for this back stress is added to equation [5.8] (Brown and Stobbs, 1976) in equation [5.13].

$$\sigma = \sigma_o + \alpha\mu\left(\frac{V_f}{2r_o}\,\varepsilon b\right)^{\frac{1}{2}} + 5.4\alpha\mu V_f\left(\frac{b\varepsilon}{2r_o}\right)^{\frac{1}{2}} \qquad [5.13]$$

$$= 158 + 39 + (5.4)(0.25)(27600)(0.045)(0.000715)^{\frac{1}{2}}$$

$$= 158 + 39 + 45$$

$$\sigma = 242 \text{ MPa at } \varepsilon = 0.025$$

Equation [5.13]compares more realistically with the observed values from the present study, $\sigma = 250$ MPa at $\varepsilon = 0.025$, than Ashby's (1971) model since it includes the back stress.

It was noted earlier that the work hardening rate of overaged Al-Cu decreases dramatically at large strains from its initially high value. The explanation given was the activation of recovery mechanisms, $\left(\frac{\partial\sigma}{\partial\varepsilon}\right)_{(-)}$. There is however,

a second reason for the decrease in the overall work hardening rate. $(\frac{\partial\sigma}{\partial\varepsilon})_{total}$ is the sum of a positive work hardening term $(\frac{\partial\sigma}{\partial\varepsilon})_{(+)}$ plus a negative work softening term $(\frac{\partial\sigma}{\partial\varepsilon})_{(-)}$. Equation [5.13] neglects the contribution of recovery mechanisms to the flow stress. The derivative of equation [5.13], [5.13a], should therefore give us an expression for $(\frac{\partial\sigma}{\partial\varepsilon})_{(+)}$.

$$(\frac{\partial\sigma}{\partial\varepsilon})_{(+)} = \alpha\mu(\frac{V_f\ b}{4r_o\varepsilon})^{\frac{1}{2}} + 5.4\alpha\mu V_f(\frac{b}{4r_o\varepsilon})^{\frac{1}{2}} \qquad [5.13a]$$

Accordingly, $(\frac{\partial\sigma}{\partial\varepsilon})_{(+)}$ varies inversely with the square root of strain; as strain increases the positive contribution, due to hard particles, to the total work hardening rate decreases.

The increase in σ_b observed in the overaged material from $\varepsilon_A = -0.15$ to $\varepsilon_A = -0.45$ is not as dramatic as from a prestrain of $\varepsilon_A = -0.0$ to $\varepsilon_A = -0.15$. Moan's data (1977) for the same material shows that $\frac{\sigma_b}{wk\ hdg}$ as a function of prestrain levels off at a prestrain of $\varepsilon \cong 0.1$ to a value of ~50%. The implications of equation [5.13a] are therefore in agreement with these results and those of the present study. $\frac{\sigma_b}{wk\ hdg}$, for the overaged material, at a prestrain of $\varepsilon_A = -0.45$ is 35%, lower than that measured at a prestrain of $\varepsilon_A = -0.15$, 38%.

The effects of the change in strain path on each of the microstructures was presented in Chapter 4. In summary the change had little effect on the solid solution and peak aged microstructures as predicted from their mechanical be-

haviour.

The pure aluminum after $\varepsilon_A = -0.45$ plus $\varepsilon_B = -0.45$ shows a significant reorientation of its cells with respect to the compression axis. Is should be noted that the back stress is observed to increase with the amount of prestrain in polycrystalline Al (Hasegawa et al, 1976).

In the overaged material a definite buckling of some plates was noted (figure 4.60) at the higher strains. Using Euler's principle of a critical buckling stress one notes the following. The stress necessary to buckle the plates will vary inversely with the plate's length to thickness ratio (equation [5.14]).

$$\sigma = \frac{\Pi^2 E}{(\frac{L}{t})^2} \qquad [5.14]$$

It is therefore more likely that the plates will buckle more severely when parallel to the compression axis than when normal to it. This is observed to be true by comparing figures 4.55 and 4.56. The back stress, σ_b, exerted on a single plate can be approximated as $\frac{\sigma_b}{V_f}$. At large strains σ_b is of the order of 100 MPa, therefore $\frac{\sigma_b}{V_f} = 2200$ MPa $= \frac{\mu}{10}$. This is much greater than the probable yield stress of the plate, $\frac{\mu}{50}$. One can conclude then, that the plates have been sheared. It is not known how the shearing of the precipitates, thought to form part of the cell walls, will

affect the further development of the cellular structure in the overaged material. A detailed study of the deformation of these plates is in progress (Verger-Gaugry, 1982).

In summary, after a material such as overaged Al-Cu undergoes a large prestrain followed by a large amount of strain in a second direction, the hard obstacles are greatly modified. The plates have either buckled and/or been sheared. If indeed the local stresses are sufficient to shear the $CuAl_2$ plates, they can no longer be categorized as "non-deformable" obstacles, and therefore equation [5.13] can no longer be applied. Any back stress accumulated at a plate will be relieved when the particle shears. Further implications of the deformation of the large precipitates depend on the nature and quantity of the resulting debris. If the large $CuAl_2$ plates are cut into sufficiently small and numerous pieces, the mechanism for the accumulation of back stress due to hard particles will be completely lost. In essence the material will then behave like a peak aged material. Had there been no change in strain path, it is likely that the particles would eventually have sheared, though at a much higher strain than in the present study. This is confirmed by (Nourbakhsh et al, 1980) who observed the buckling of $CuAl_2$ plates in a similar alloy at strains of 4 - 5.

5.2 Subsequent Yield Surfaces

A variety of maps and diagrams have been used for the representation of both metal forming processes and fracture mechanisms (Embury and Duncan, 1981). Several different systems of axes may be used to construct these maps. The three principal stresses are used as axes in the present study to facilitate the representation of axisymmetric deformation.

The experimental determination of entire yield surfaces subsequent to plastic deformation is difficult (Hecker, 1973). In view of the limited experimental evidence obtained in this study a simple formulation of the yield surface has been chosen rather than exploring the entire surface experimentally. Work hardening rates from monotonic flow, and the measured directionality of the material's flow stress after prestrain, have been used to construct the yield surfaces presented in this section.

The yield surface, based on the von Mises criterion of the material both before and after 15% deformation in compression in the A direction is shown in figures 5.1 to 5.4. The available data has been extended to illustrate the two yield surfaces for multiaxial stress states. The method used to construct the surfaces is described in Appendix A.

The movement of the yield surface of a material exhibiting ideal macroscopic plasticity is usually represented in terms of kinematic and isotropic work hardening

(Saugerud, 1980). Kinematic hardening is basically a translation of the yield surface, and isotropic hardening is a uniform expansion of the surface. The changes in the yield surface after 15% deformation vary from material to material. These changes correlate to differences in the work hardening behaviour and the size of the Bauschinger effect of each material.

The pure aluminum, the Al-Cu solid solution and the peak aged Al-Cu show little or no kinematic hardening. (It must be remembered that this remark is based on only four data points.) The pure aluminum shows little expansion of the yield surface, whereas the peak aged material has experienced a large increase in flow stress, and therefore a greater expansion of its yield surface. These differences in mechanical behaviour are better illustrated by the relative yield surface movement after prestraining (figures 5.1 and 5.4) than by the comparison of stress strain curves (figures 4.5 and 4.8).

There is a third effect involved in the movement of the yield surface of the over aged material. It was noted earlier that after 15% prestrain, the back stress measured by Moan (1977) on stress reversal was larger than the 'back stress' measured in the present study after a 90° change in direction. If it is assumed that the yield surface remains symmetric, the major axis of the yield surface ellipse must elongate to compensate for this difference. As a result, a

slight rotation of the von Mises ellipse, (seen in figure 5.4) occurs.

So far the original yield surface, and the yield surface subsequent to plastic deformation along some known strain path, have been mapped and compared in the σ_1 - σ_2 plane. It has been noted that the presence of hard obstacles, such as large $CuAl_2$ precipitates, influenced the nature of the changes in yield surface as the material was deformed. The effect of the large, hard obstacles can also be explained by the difference in the ratio of kinematic to isotropic hardening in each of the materials. With more experimental information, a more detailed map could be constructed, which might in turn further the understanding of precipitation hardening mechanisms in relation to mechanical anisotropy. Section 5.4 will discuss the implications of these results relative to fracture processes.

5.3 Fracture Characteristics

This section will describe and discuss the fracture data obtained for Al and Al-Cu in the present study. As explained in the literature survey it is of value to try to characterise the operative fracture modes by the use of several parameters. In this way it is possible to classify the fracture modes and make a comparison of the results with the predictions of current theories.

The majority of the fracture data obtained in this study resulted from tensile tests. In cases where extensive

necking occurs during the tensile test, the stress state does not remain one of uniaxial tension. The stress state varies systematically due to the development of an increasing hydrostatic stress in the neck of the sample. Thus, in attempting to characterise a fracture process, it is of value to estimate not only the true axial stress at fracture, but also the radial stress operative at this point. This value is obtained from a knowledge of the shape of the neck at fracture, and the reduction in area at fracture (Dieter, 1976). Table 4.1 contains the calculated values of the above for the materials which experienced necking. In addition to the tensile tests, some compressive tests were performed in order to determine, in an approximate manner, at what stress microcracks were formed in compression. The data are approximate because it is difficult to maintain the stress state of the entire sample in uniaxial compression at large strains due to the effects of barrelling.

Aluminum

Scanning electron microscopy was used to investigate the fracture surface of pure aluminum. In figure 4.8 large voids can be seen to have formed, most probably at the sites of Fe-Si rich inclusions present in the material. Between these deep voids there are areas which suggest that coarse slip has occured during void growth, to cause the final coalescence leading to fracture. Despite the strain to fracture being large, the fracture stress of aluminum is relatively

low. The behaviour of Al, in keeping with many ductile materials, suggests that void growth is a geometrically limited problem and thus the Al fracture is strain controlled.

Aluminum-Copper

The three different ageing treatments of Al-Cu studied show significantly different fracture behaviour. Of the three the solid solution was the most ductile, with a final strain to fracture of 0.91. During the tensile test it necked considerably more than the others, resulting in a maximum radial stress of 81 MPa at the neck, at fracture. Therefore at the time of fracture the specimen was not in a state of uniaxial tension.

The profile of the fracture surface shown in figure 5.5 indicates that the solid solution is a ductile condition. The fracture surface is transgranular and irregular. Some voids, near the fracture are evident. The grains in the necked region have been greatly elongated in the direction of the applied tensile stress.

The longitudinal cross section of the sample (figure 5.5) has an interesting feature. During the course of the sample preparation, the solid solution was slightly aged and, as a result, preferential precipitation has begun along the slip lines. Towards the centre of the sample, there is evidence of slip on two systems, as shown by the cross hatched pattern. The slip line spacing on the fracture surface

(figure 4.10) is approximately three microns. The spacing of the coarse slip appears to be smaller than in the pure aluminum.

Both scanning electron microscopy and metallography show the definite ductile nature of the fracture. Since the material was a solid solution, obstacles other than Al-Cu precipitates must be responsible for the initial void nucleation. The larger voids (figure 4.10) are assumed to be similar to those of the same magnitude in the pure aluminum case. (As mentioned before, these large voids are probably at the sites of Fe-Si rich inclusions.)

Though the fracture of the solid solution is similar in many respects to that of the pure aluminum, it reaches a higher flow stress at a much lower strain. The stress strain curve does not flatten dramatically as in the case of the pure aluminum. The strain distribution to failure differs significantly from the Al. The fracture surface of the solid solution shows regions of shear, and microvoids. One may therefore conclude, that though both fractures are ductile, the failure of the solid solution involves more than one fracture mode.

The peak aged Al-Cu fractured intergranularly at a much lower strain than the solid solution, $\varepsilon = 0.32$. The work hardening rate was initially high. The fracture surface appears to follow an intergranular path, but has progressed at a 35° angle to the tensile axis (figure 5.6). This im-

plies some form of shear linking was involved in the failure process. Figure 4.11 confirms the intergranular nature of the failure. Figure 5.7 shows grain elongation has occurred, though not to as great an extent as in the solid solution case. Some voids, normal to the tensile axis located along the grain boundaries can be seen within the material. From the general shape of the stress strain curve and the fractographic evidence, one can conclude that the fracture was intergranular and "quasi-brittle". Before extensive voiding could occur, the tensile and or shear stress at the grain boundaries exceeded the cohesive forces and the material failed. Some slip line traces are visible on the fracture surface. Their spacing is the finest of all the materials, 1-2 microns, on the grain boundary surface. The presence of finely spaced slip line traces is consistent with the microstructure of the peak aged material.

The overaged Al-Cu fractured at a strain of $\varepsilon = 0.71$, twice that of the peak aged material, but significantly less than that ($\varepsilon = 0.91$) of the solid solution. It is interesting to note that the solid solution and the overaged materials have similar fracture stresses. As can be seen in the micrograph of figure 5.8, the sample volume above the fracture surface is full of very large voids. These, as shown by the SEM photograph, were most probably nucleated by large particles at the grain boundaries. In the metallograph all the voids have formed at the grain boundaries, and not within the

the grains. Some of the voids nearer the fracture surface have begun to coalesce. The voids are at many different angles to the tensile axis, depending on the orientation of the grain boundary, but none are parallel to the tensile axis. This sample did not fail along a plane at 45° to the tensile axis as the peak aged sample did.

As the tensile data predict, this failure cannot be categorized simply as a brittle intergranular fracture. Although it is intergranular in path, the SEM studies (figure 4.12) reveal that the fracture surface is dimpled. The dimple size is of the same order of magnitude as the distance between the precipitates (0.5μ).

Both the peak aged material and the overaged have failed intergranularly. However the degree of local ductility in the two fractures is different. The peak aged material exhibits quasi-brittle facets. The fracture surface of the overaged material contains localised areas of extensive voiding. It should be noted that the fracture stresses for the two materials are similar (380-410MPa).

Neither fracture is truly brittle but involves extensive local plastic deformation. The occurrence of grain boundary fracture is an indication of a stress controlled fracture process. The stress for the decohesion of grain boundaries is achieved by work hardening. Since the fracture surface of the overaged material is predominantly intergranular, the plastic stress to failure is limited by the

grain boundary cohesive strength. The joining of boundary microcracks may have involved extensive shear. One may however assume that the fracture mechanism leading to the failure of the overaged material was stress controlled.

Dimples, similar to those mentioned previously, were observed on the fracture surfaces of both the peak and over aged materials after the two stage tensile test (figure 5.9). It was suggested earlier that both fractures occur by a stress controlled failure mechanism. There is evidence of some cumulative damage at the grain boundaries having occurred prior to failure. The detailed microstructural events leading up to the failure are not clear. It was observed that for the two stage tensile test the fracture stress is lower and the dimples more prevalent, in both materials. A quantitative interpretation of these data is difficult due to the difference in stress state of the sample in the two stage, as opposed to the uniaxial tensile test.

5.4 Fracture Maps

Mapping is a useful way to represent fracture mechanisms as well as other deformation processes. Several different types of fracture maps were described in Chapter 2. Of these only one type was used in the present study. Though the axisymmetric map is better suited for illustrating fracture processes, the purpose here is to show the significance of the movement of yield surfaces with respect to fracture.

Thus the plane stress type map was used.

It is possible to represent the fracture processes for both ductile and brittle failures on a fracture map. The fracture criterion used in this study for the intergranular fracture of the peak and overaged materials assumes brittle failure by cleavage. Obviously this "brittle" fracture criterion (presented in Appendix A) is not suitable for either the solid solution or the pure aluminum since both fractures were ductile.

Any type of brittle fracture surface, based on a critical stress criterion, is simple to map in this way. The critical stress may be determined experimentally for various stress states or calculated from theory. However, ductile fracture is not as simple to represent in this manner since it involves several processes. For instance, to illustrate the fibrous ductile fracture mechanism, the following surfaces may be included on the same map: surfaces representing yield, void nucleation and void linkage (LeRoy et al, 1981).

Although there have been a number of recent models proposed for shear localisation (Anand and Spitzig, 1982 and Pierce et al , 1982), they are not simple to represent on a failure map. Thus in the current work, the shear failure is represented as a critical shear stress and hence a line parallel to the yield surface (figure 2.7).

Only two fracture surfaces, based on tensile test results, are included in this study: the peak and over aged materials, both of which failed intergranularly. Though it

is evident from the fractography already discussed that the two fractures are very different, the same (cleavage) fracture criterion was used to construct both fracture surfaces on the plane stress type map. These are shown in figures 5.3 and 5.4 along with the initial and subsequent yield surfaces.

An attempt was made to determine the stress at which the material fractured in compression, and the mode of failure in compression as opposed to tension. Material and equipment restrictions prevented the attainment of compressive failure. However at a strain of $\varepsilon = -1.6$, a few small microcracks were visible in the peak aged Al-Cu (see figure 5.10). It is not possible to draw any major conclusions from these results, since the material may not have been in pure compression and the microcracks may well have nucleated at a lower strain than -1.6. Since compressive fracture is not the major area of interest of this study, the experiment was not pursued. It is evident that this type of mapping combined with experimental results can be of great use in the study of fracture mechanisms in compression as well as in tension.

In section 5.2 stress maps (in plane stress) illustrating the effects of strain history on material behaviour were presented. The yield surface movements are now discussed in relation to the material's brittle fracture surface. Figure 5.4 serves as a good example of the possibi-

lities of this mapping technique. By changing the direction of imposed strain the yield surface of the overaged material is shifted away from the low tensile fracture stress in the A direction. If deformation had been continued in the A direction instead of the B direction the yield surface would have reached the fracture surface at a lower strain, and thus failed. In other words these maps could be of great use in determining the optimum strain path to follow during metal working procedures. Of course, the mapping of deformation paths will be a much more powerful tool when the entire yield surface can be determined accurately for any strain history, by calculation instead of experimentation.

The representation of the effects of temperature, hydrostatic pressure, and other system parameters on the fracture behaviour of a material is also possible. For instance, as hydrostatic pressure is increased, the measured fracture stress for peak aged Al-Cu changes. With an imposed hydrostatic pressure of 70 MPa the peak aged material fails intergranularly at a stress of 528 MPa. This is higher than that measured in uniaxial tension, 408 MPa. If the hydrostatic pressure is increased further the fracture mode changes dramatically (Teirlinck, 1982). The hydrostatic pressure suppresses microcracking at the grain boundaries and the fracture becomes more ductile. Therefore not only does the fracture stress change, the fracture mode that causes actual failure will change for different stress states. The

mode of failure will depend on which fracture surface has the lowest stress for a particular stress state, and on how the stress state does or does not change as deformation proceeds. Eventually it should be possible to model a fracture surface for each separate type of failure throughout all the stress states. With this information one could predict the type of failure and the stress at which it would occur.

Differences in a material's properties, such as grain size, can also be effectively illustrated with this type of map. It is well known that the grain size, for instance, of a material will alter the fracture stress. Evensen et al (1975) reported the fracture stress for an Al-Mg alloy, which failed intergranularly for several different grain sizes. These are included in Table 5.2 for Al- 0.63 wt% Mg - 0.39 wt% Si.

TABLE 5.2 Fracture Stress Variation with Grain Size

Grain Size (m)	Peak Aged (MPa)	Over Aged (MPa)
0.0011	290	275
0.0004	340	280
0.0002	390 (extrapolated)	285

The fracture path is intergranular for all of the above conditions. Figure 5.11 illustrates the fracture stress (assuming fracture by cleavage) of the peak aged material for

each grain size in Table 5.2. Though not true in this case, the fracture mode may also change as the grain size of the material is altered.

It is clear that these maps have the potential of being a powerful tool in the field of metal working. At this time it is not yet possible to predict accurately the effects of all the parameters discussed, only to document experimental observations. Extensive documentation of both yield and fracture surfaces, combined with a good understanding of the material's microstructure are necessary in order to develop this type of map into a practical tool.

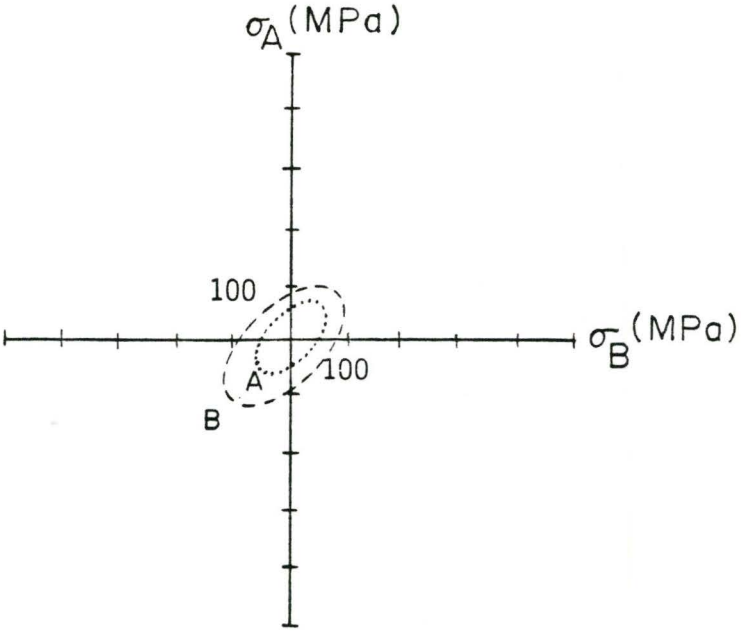

FIGURE 5.1 Yield Surface Movement: Aluminum

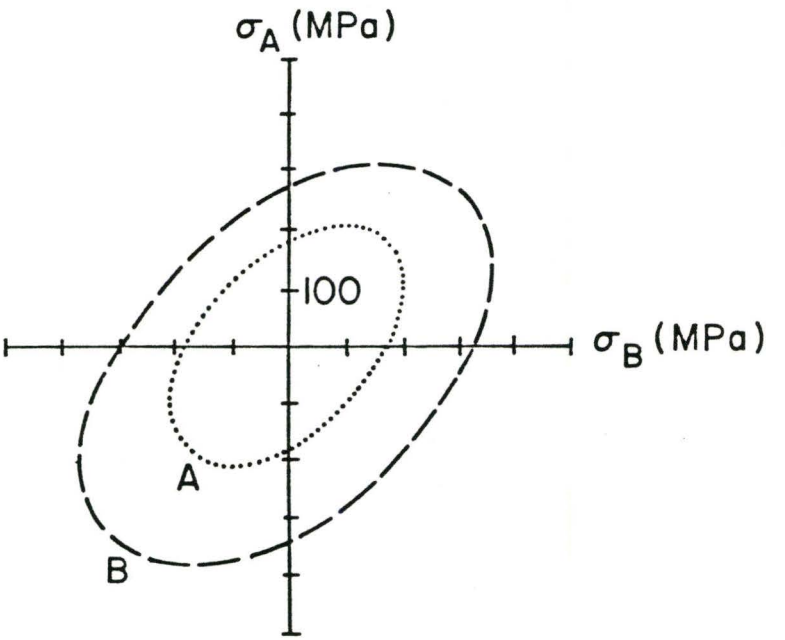

FIGURE 5.2 Yield Surface Movement: Al-Cu Solid Solution

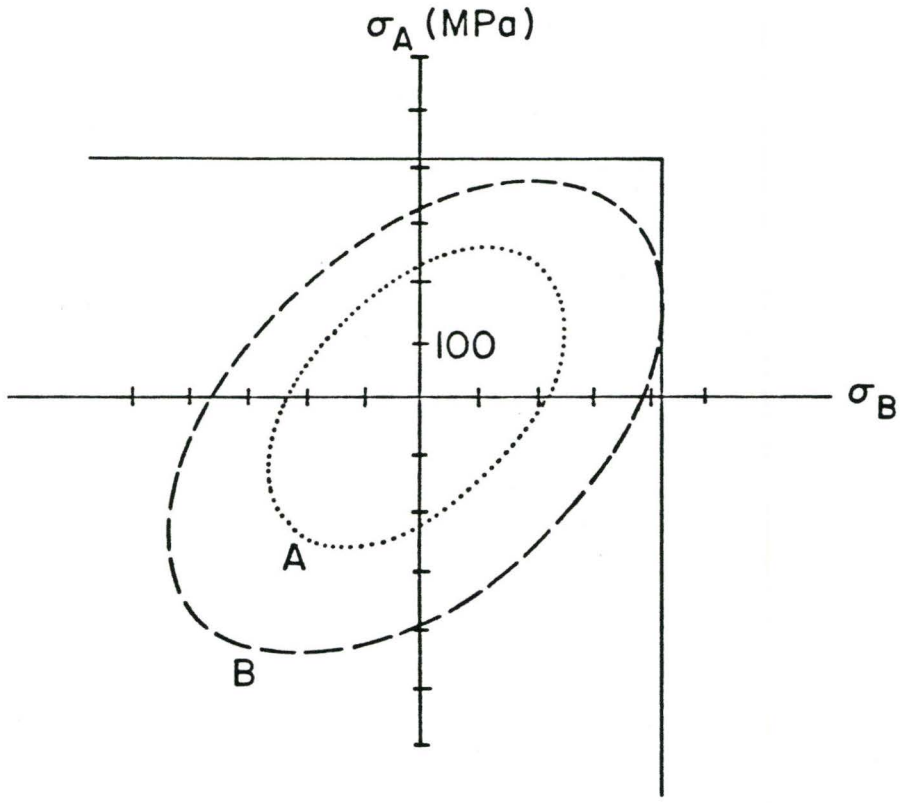

FIGURE 5.3 Yield Surface Movement: Peak Aged Al-Cu

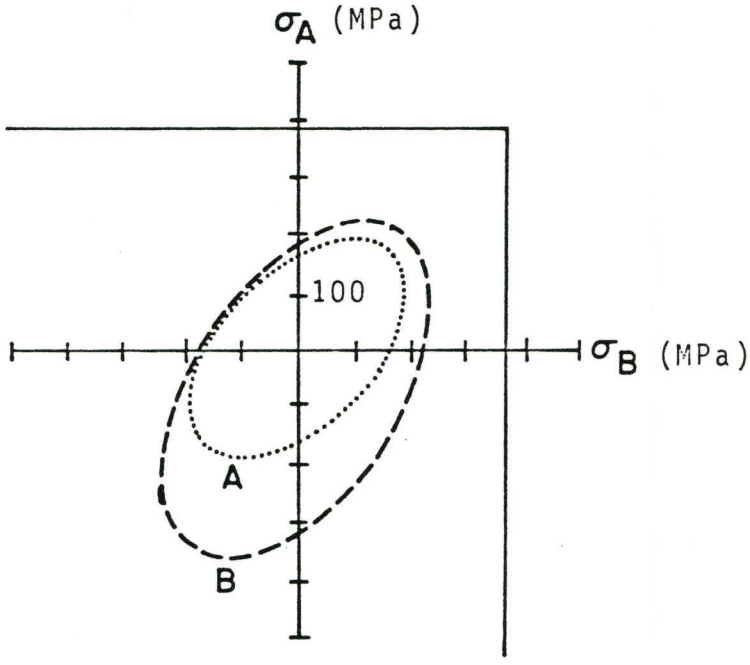

FIGURE 5.4 Yield Surface Movement: Over Aged Al-Cu

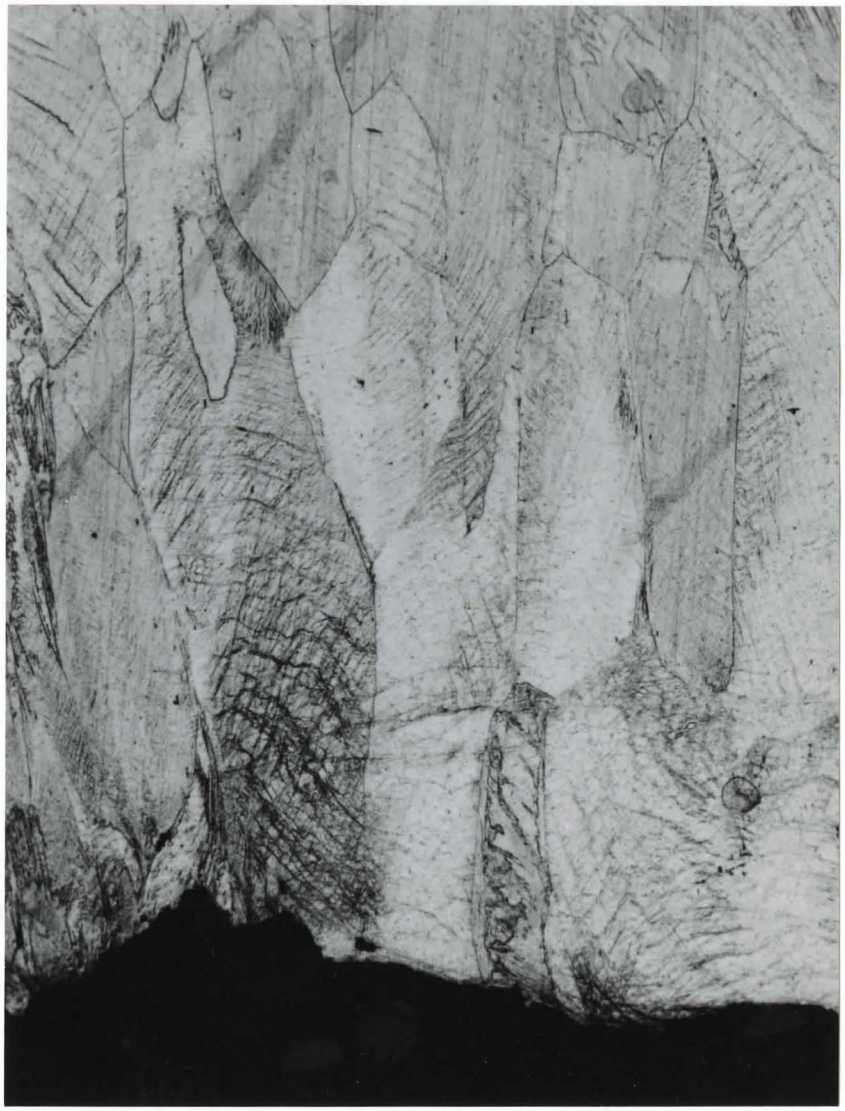

TENSILE
AXIS

FIGURE 5.5 Fracture Profile of Al-Cu Solid Solution

The above is a longitudinal cross section of a tensile specimen after fracture. The sample was etched with Keller's reagent. Magnification: 55 x

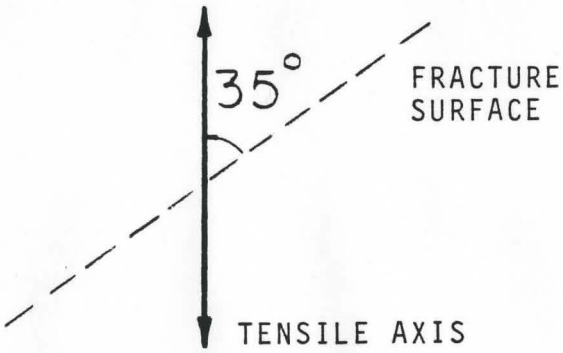

FIGURE 5.6 Fracture Profile of Peak Aged Al-Cu

The above is a longitudinal cross section of a tensile specimen after fracture. The sample was etched with Keller's rea gent. Note the angle between the fracture profile and the tensile axis. Magnification: 60 x

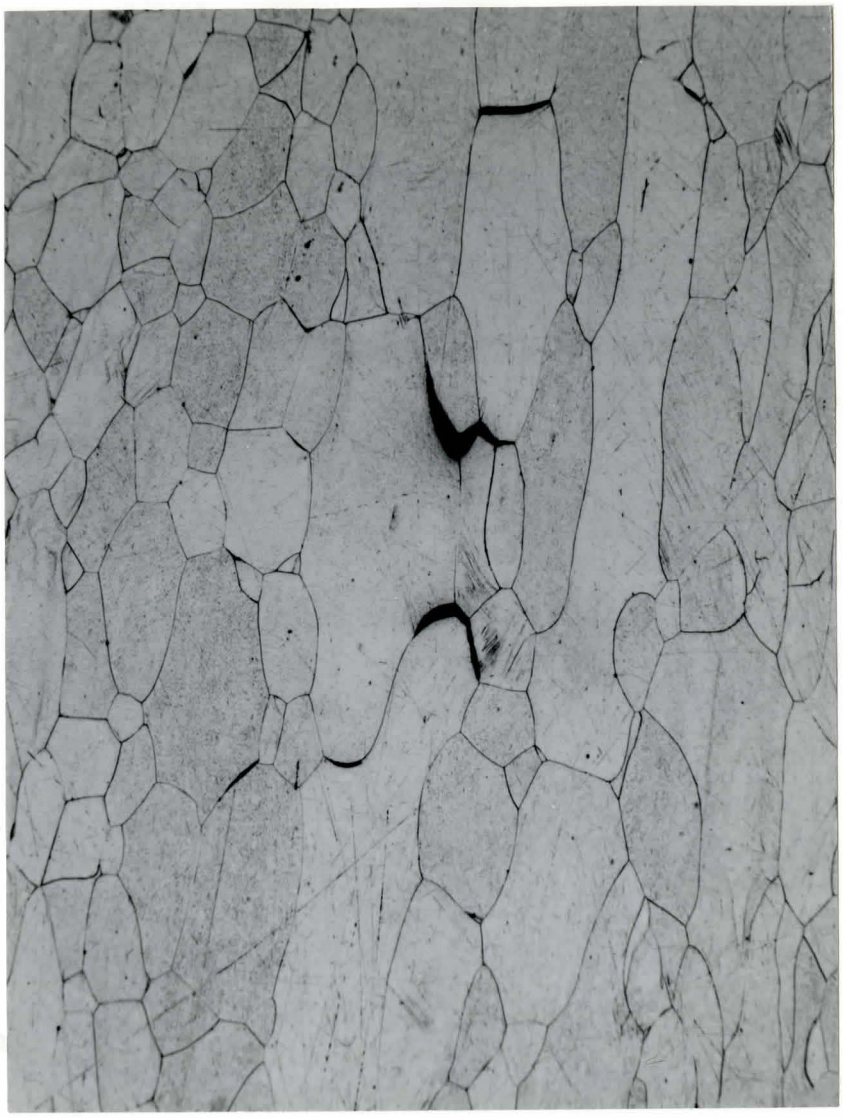

TENSILE
AXIS

FIGURE 5.7 Central Cross Section of the Fractured Peak Aged Al-Cu

The same sample as in figure 5.6. The above area is further up the guage length of the specimen.
Magnification: 120 x

TENSILE
AXIS

FIGURE 5.8 Fracture Profile of Over Aged Al-Cu

The above is a longitudinal cross section of a tensile specimen after fracture. The sample was etched with Keller's reagent.
Magnification: 55 x

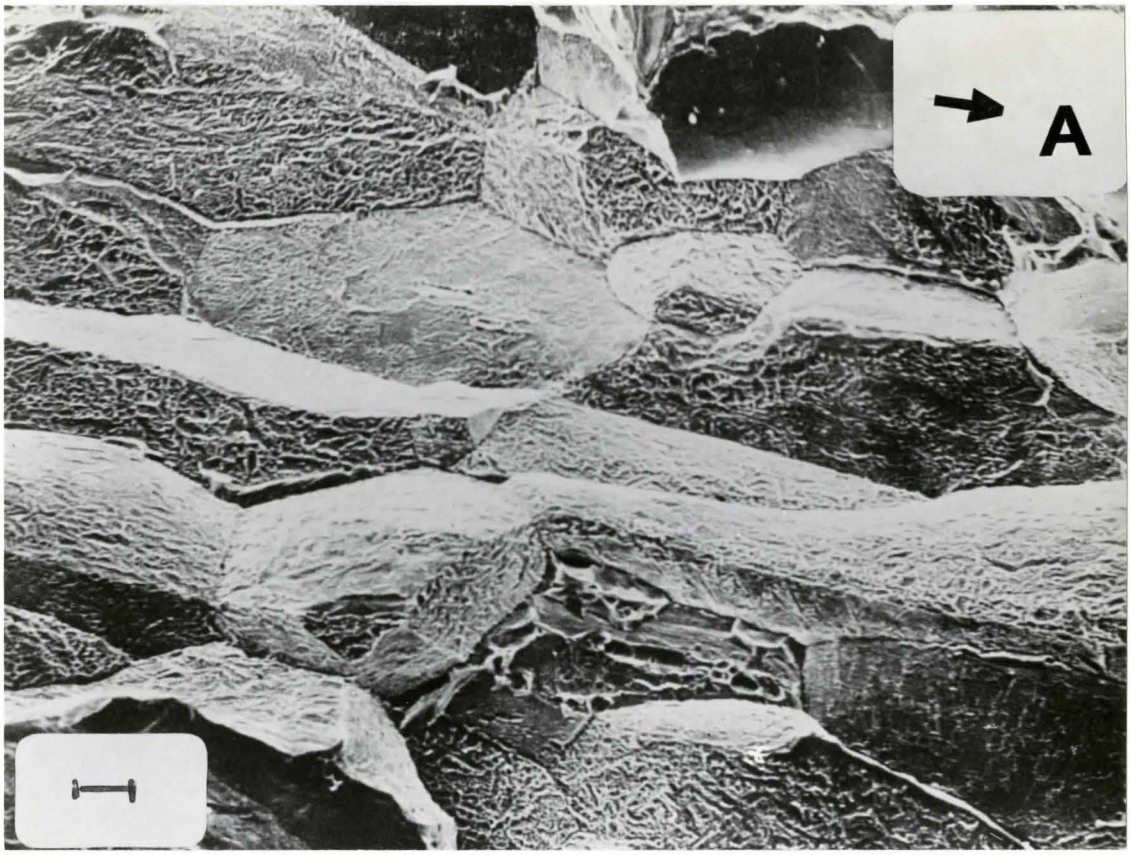

FIGURE 5.9 Fracture Surface of Peak Aged Al-Cu: Two Stage Tensile Test

A scanning electron micrograph of peak aged aluminum-copper pulled in the A direction, 5% strain, and then in the B direction until fracture.
Magnification: 320 x (25 μ)

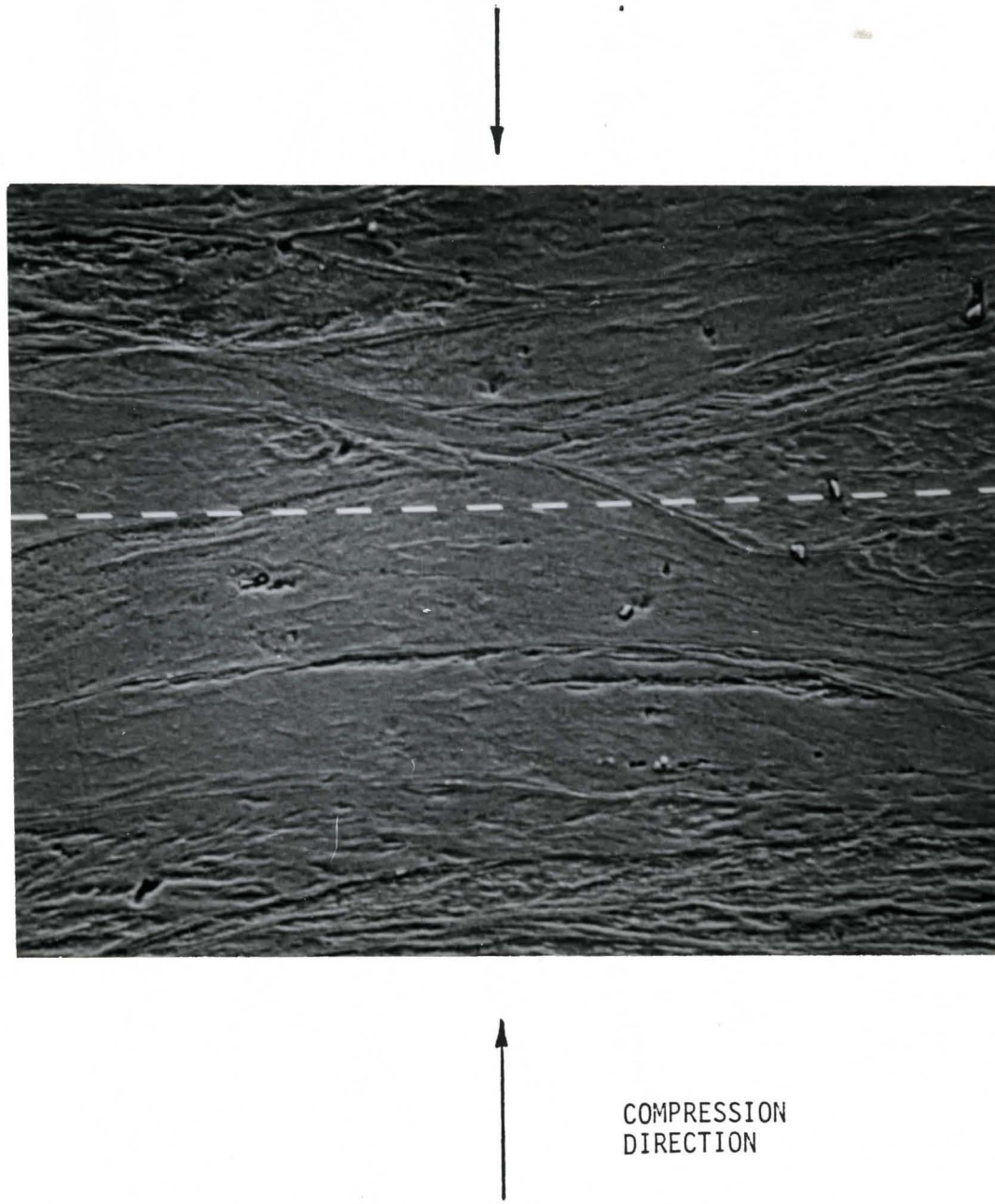

FIGURE 5.10 Microcracks in Compressed, Peak Aged Al-Cu

A central cross section of the specimen at a strain of $\varepsilon = -1.6$. The specimen was polished and then etched with Keller's reagent.
Magnification: 480 x (10 μ marker)

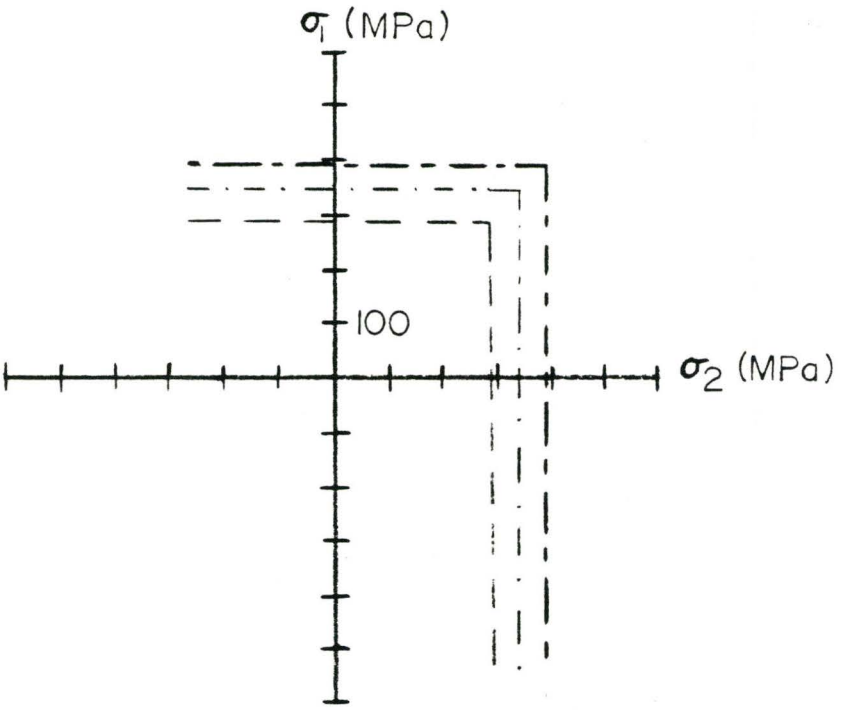

GRAIN SIZE: 0.0002 m

GRAIN SIZE: 0.0004 m

GRAIN SIZE: 0.0011 m

FIGURE 5.11 The Effect of Grain Size on the Fracture Surface of an Al-Mg-Si Alloy. (Plane Stress)

Plot of the cleavage fracture surface of an Al 0.63 wt% Mg 0.39 wt% Si alloy, for three different grain sizes. The above was plotted using fracture data from Evensen et al (1975).

CONCLUSIONS

The observations made in the present study lead to the following conclusions.

(1) The effect of a change in strain path is largest in the overaged Al-Cu alloy. This implies that the large particles present in the overaged material play a significant role in the accumulation of 'back' stress.

(2) The same Bauschinger type effect is observed in tension and in compression tests. σ_b/wk hdg is slightly smaller for a 90° change in strain path than for a 180° change in strain path.

(3) The work hardening rate at large strains is low for the materials (overaged Al-Cu and pure aluminum) with the furthest developed microstructures. The work hardening rate is higher at large strains for the solid solution and peak aged materials. These alloys have developped no signs of a cellular microstructure at strains of $\varepsilon = 1$.

(4) The work hardening behaviour can also be related to the mean free path of an average dislocation, s. s is large for Al, and the overaged material and small for the other two.

(5) The cellular structure formed in the overaged material is of the same scale as the interparticle distance. The particles seem to form part of the cell walls.

(6) The microstructure and stress state greatly affect the fracture mechanism(s) which leads to failure.

(7) The use of plane stress maps to illustrate the movement of the yield surface with respect to the fracture surfaces is potentially a very powerful tool.

REFERENCES

Anand L. and Spitzig W.A., (1982), Acta Met., 30, p 553

Asaro R.J., (1979), Acta Met., 27, p 445

Asaro R.J. and Rice J.R., (1977), J. Mech. Phys. Solids, 25, p 309

Ashby M.F., (1971), Strengthening Methods in Crystals, A.Kelly and R.B. Nicholson editors, Elsevier Publishing Co.

Ashby M.F., Gandhi C. and Taplin D.M.R., (1979),Acta Met., 27, p699

Ashby M.F., and Gandhi C., (1979), Acta Met., 27, Overview 5.

Ashby M.F., (1982), unpublished seminar presentation at McMaster University

Ashby M.F. and Embury J.D., (1981), Cambridge University Research Report

Bergstrom Y., (1969), Mat. Sci. and Eng., 5, p193

Bergstrom Y. and Roberts W., (1971), Acta Met., 19, ; 815

Bridgman P.W., (1943), Trans. of ASM, 32, p 553

Brown L.M. and Embury J.D., (1973), Proc. of 3rd Int. Conference on the Strength of Metals, Cambridge, p 164

Brown L.M. and Ham R.K., (1971), Strengthening Methods in Crystals, A. Kelly and R.B. Nicholson editors, Elsevier Publishing Co.

Brown L.M. and Stobbs W.M., (1976), Phil. Mag., 34, p 351

Chung N., Embury J.D., Evensen J.D., Hoagland R.G., and Sargent C.M., (1977), Acta Met., 25, p 377

Chandra H., (1980), Phd Thesis, McMaster University

Cockcroft M.G., (1967), Ductility, p 199, ASM Seminar

Dew-Hughes D., and Robertson W.D., (1960), Acta Met., 8, p 156

Dieter G.E., (1976), Mechanical Metallurgy, Second Edition, McGraw Hill Publishers

Embury J.D., (1971), Strengthening Methods in Crystals, A. Kelly and R.B. Nicholson editors, Elsevier Publishing Co., p 331

Embury J.D. and Duncan J.L., (1981), Ann. Rev. Mater. Sci. and Eng., 18, p505

Embury J.D. and Nes Erik, (1974), Sonderdruck aus Zeitschrift Metallkunde Band, 65, p 545

Evensen J.D., Ryum N., and Embury J.D., (1975), Mat. Sci. and Eng., 18, p 221

French I.E. and Weinrich P.F., (1975), Met. Trans. A, 6A, p 1165

French I.E. and Weinrich P.F., (1979), Met. Trans. A, 10A, p 297

Calvet J., Jacquet P., and Guinier A., (1938), Academie des Sciences, 206, p 1972

Guinier A., (1942), J. Physique, 8, p 122

Gurson A.L., (1977), Adv. in Res. on the Strength and Fract. of Mater.; Int. Conf. on Fract., Pergamon Press, v2A, p357.

Hasegawa T., Yakou T., Shimizu M., and Karashima S., (1976), Trans. J.I.M., 17, p 414

Hecker S.S., (1973), Metall. Trans., 4, p 985

Kelly A. and Nicholson R.B., (1963), Precipitation Hardening, Prog. in Mat. Sci., Pergamon Press

Kocks U.F.,(1976), J. Eng. Mater. Technology, Trans ASME, 98, Ser. H, no. 2, p 97

Kocks U.F.,(1977), Int. Conference on the Strength of Metals and Alloys, 4th Proc., Nancy

Kuhlmann-Wilsdorf D., (1968), Work Hardening, J.P. Hirth and J. Weertman editors, Gordon and Breach, New York, p 97-139

Kuhn H.A. and Lee P.W., (1971), Met. Trans., 2, p 3197

Lee P.W. and Kuhn H.A., (1973), Met. Trans., 4, p969

LeRoy G. and Embury J.D., (1977), Report #115, McMaster University

LeRoy G., Embury J.D., Edwards G., and Ashby M.F., (1981), Acta Met., 29, p 1509

Lloyd D.J. and Kenny D., (1980), Acta Met., 28, p 639

Lloyd D.J. and Sang B.D., (1977), Scripta Met., 11, p 301

Lloyd D.J., Sang B.D., Embury J.D., Wycliffe P. and LeRoy G., (1978), Mat. Sci. and Eng., 36, p 35

Lorimer G.W., (1976), Precipitation in Aluminum Alloys K. Russell and H. Aaronson editors

McClintock F.A., (1968), J of App. Mech., 6, p363

Moan G.D., (1977), Phd Thesis, McMaster University

Murrell S.A.F., (1963), Rock Mechanics, C. Fairhurst editor, Proc. 5th Symposium Rock Mech., New York, Pergamon Press p 563

Murrell S.A.F., (1965), Geophys. J.R. Astron. Soc., 10, p 231

Nourbakhsh S. and Nutting J.,(1980), Acta Met., 28, p 357

Orowan E., (1954), Dislocations in Metals, AIME

Pierce D., Asaro R.J., and Needleman A., (1982), Acta Met., 30, p 1087

Preston G.D., (1938), Phil. Mag. and J. Science, 26, p 855

Price R.J. and Kelly A., (1964), Acta Met., 12, p 159

Rice J.R., and Tracey D.M., (1969), J. Mech. Phys. Solids, 17, p 201

Ryder D.A. and Smale A., (1963), Fracture of Solids, Wiley, p 237

Saugerud O.T., (1980), Report UR-80-08, University of Trodheim, p 26

Seah M.P., (1981), Acta Met., 28, p 955

Silcock J.M., Heal T.J., and Hardy H.K., (1954), J. Inst. Met., 82, p 238

Speich G.R., (1977), Proc. of AIME Symposium on Toughness Characterization and Specifications for HSLA and Structural Steels

Tanaka K. and Spretnak J., (1973), Metall. Trans., 4, p 443

Teirlinck D., (1982), unpublished data

Thomason P.F., (1968), Inst. J. Mech. Sci., 10, p 501

Trozera J., (1963), Trans. of the ASM, 56, p 781

van den Beukel A., (1979), Scripta Met., 13, p 83

Verger-Gaugry J.L., (1982), private discussion

Washburn J. and Murty G., (1965), J. Appl. Phys., 37, p 2511

Wilson D.V., (1965), Acta Met., 13, p 807

Zener C.M., (1947), ASM Seminar, 29th National Metal Congress and Exposition, Chicago

APPENDIX

A short summary of the method used by Ashby and Embury (1981) to contruct yield and fracture surfaces for brittle solids is given. The computer program used to generate these surfaces is presented at the end of the appendix. The surfaces are plotted in terms of the principal stresses σ_1, σ_2 and σ_3. Diagrams used for this study were drawn in two dimensions only. For the purpose of illustrating the effects of change in strain path on the yield strength of the material, σ_1 and σ_3 were chosen as axes, $\sigma_2 = 0$. This is termed plane stress. The diagram can also be constructed for the case of axisymmetry. For axisymmetry $\sigma_2 = \sigma_3$, therefore it is still possible to draw the diagram in two dimensions, σ_1 and σ_3 being the two chosen axes.

Yield Surface

The von Mises yield criterion was used to plot the yield surface. The condition for yielding is therefore;

$$2\sigma_y^2 = (\sigma_1 - \sigma_2)^2 + (\sigma_2 - \sigma_3)^2 + (\sigma_3 - \sigma_1)^2$$

for $\sigma_2 = 0$; $\quad \sigma_y^2 = \sigma_3^2 + \sigma_1^2 - \sigma_1\sigma_3$ (A1)

for $\sigma_2 = \sigma_3$; $\quad \sigma_y^2 = (\sigma_1 - \sigma_3)^2$

where σ_y is the yield strength of the material.

Several deformation theories describing a unique relationship between stress and total strain have been proposed over the past few years. As computer capabilities increase so does the complexity of these mathematical models of the dynamic processes involved as a material is plastically deformed. Two such examples, isotropic and kinematic work hardening rules, are briefly described below.

Isotropic work hardening, the homogeneous expansion of the yield surface, can be expressed in terms of stress and strain;

$$\frac{\sigma_y}{\sigma_o} = 1 + \left(\frac{\bar{\varepsilon}}{\varepsilon_o}\right)^n \qquad \text{(A2)}$$

where $\frac{9}{2}\varepsilon^2 = (\varepsilon_1 - \varepsilon_2)^2 + (\varepsilon_2 - \varepsilon_3)^2 + (\varepsilon_3 - \varepsilon_1)^2$ (A3)

Kinematic hardening is described by a translation of the yield surface;

$$\sigma_y = \frac{3}{2}\left[(\sigma_{ij} - s_{ji})(\sigma_{ji} - s_{ij})\right]^{1/2} \qquad \text{(A4)}$$

Isotropic work hardening cannot account for the role of obstacles, such as $CuAl_2$, present in the material. Alone, kinematic hardening can account for back stress due to obstacles but cannot properly account for the increase in flow stress due to matrix hardening. Together they are a far more powerful tool.

The immediate purpose of this study was not to gen-

erate a new deformation theory. Equations (A2) and (A4) were not used, but their basic principles, combined with experimental data, were.

Prior to plastic deformation, the material was assumed to be isotropic. The intial yield surface was plotted, inferred from experimental results for four stress states; pure tension and pure compression, in the rolling direction and one of its orthogonals. The yield stress, prior to any plastic deformation, was the same for all four stress states. The initial yield surface for all four materials was plotted in this manner.

Each material was deformed in the A direction to a plastic strain of 15%. In the case of the overaged Al 3.6% Cu, the subsequent yield surface was no longer that of an isotropic material. The elliptical form of the initial von Mises yield surface is maintained. A combination of kinematic hardening and isotropic hardening is implied by this new yield surface (Figure A).

It must be remembered that this diagram was constructed solely on the basis of the available data, and does not represent a series of experiments exploring the subsequent yield surface. The following procedure was used to estimate the new yield surface. The computer program was modified to draw both the initial and subsequent surface on the same diagram.

The initial surface is calculated by the computer based on input for a single stress state. The other points shown in Figure A, σ_o^{-A}, σ_o^{B}, and σ_o^{-B} were measured to confirm that the material was indeed initially isotropic.

After 15% plastic strain in the negative A direction, the yield stress was measured in the negative A (σ_y^{-A}) and negative B (σ_y^{-B}) directions. It was possible to infer the yield strength in the positive A direction (σ_y^{+A}) from Moan (1977). Moan conducted a detailed investigation of the Bauschinger effect in Al 3.6% Cu as a solid solution and in the overaged condition. His plot of the ratio of back stress to total work hardening, as a function of prior strain was used to calculate σ_y^{+A}. Definitions of the symbols used are shown in Figure B. As the Bauschinger effect arises from the polarization of the flow behaviour due to the particles, it can be assumed, on a macroscopic level, that the Bauschinger effect is the same for compression-tension as for tension-compression. Equation (A5) was therefore used to calculate σ_y^{+A}:

$$\sigma_b^{-A:+A} = \sigma_b^{+A:-A} = \frac{1}{2}(\sigma_{final}^{+A} - \sigma_y^{-A})$$

$$\frac{\sigma_b^{-A:+A}}{wk\ hdg} = \frac{1}{2}\left(\frac{\sigma_{final}^{-A} - \sigma_y^{\pm A}}{\sigma_{final}^{-A} - \sigma_o^{-A}}\right) \qquad (A5)$$

The value of the new yield strength for three stress

states is now known. It was also assumed that the new yield surface would be symmetric, i.e. $\sigma_y^{-B} = \sigma_y^{+B}$.

Two modifications of the computer program were made so that the surface would fit the four known values of the yield stress. The data suggests that $\sigma_b^{-A:-B} < \sigma_b^{-A:+A}$, in other words x > y, shown in Figure A. This is introduced into the computer program as a proportionality constant, P. The second modification to the program was the shift, along the σ_A axis, of the center of the ellipse. This is due to the back stress that was built up in the A direction.

Fracture Surfaces

The fracture surfaces constructed for the schematics used in this study are based on Murrell's (1963, 1965) extension of Griffith's fracture criterion for failure by cleavage, in brittle materials. Griffith's hypothesis was that the fracture was caused by the stress concentrations at the tips of small cracks in the material. The cracks considered by Griffith were two dimensional flat elliptical cracks. The criterion is expressed in terms of the principal stresses,

$$\begin{aligned} (\sigma_1 - \sigma_3)^2 &= 8T_o(\sigma_1 + \sigma_3) \quad &\text{for } \sigma_1 + 3\sigma_3 > 0 \\ \sigma_3 &= -T_o \quad &\text{for } \sigma_1 + 3\sigma_3 < 0 \end{aligned} \tag{A6}$$

where T_o is the strength of the material in uniaxial tension. If the sample is in uniaxial compression $C_o = 8T_o$. There-

fore the criterion implies that the material is eight times stronger in compression than in tension.

Murrell extended Griffith's fracture surface to three dimensions, and expressed the criterion in terms of σ_1, σ_2, and σ_3 (equation (A7)).

$$(\sigma_1-\sigma_2)^2 + (\sigma_2-\sigma_3)^2 + (\sigma_3-\sigma_1)^2 = 24T_o(\sigma_1+\sigma_2+\sigma_3) \quad \text{(A7)}$$

or: $$\sigma_3^2 - \sigma_1\sigma_3 + \sigma_1^2 = 24T_o(\sigma_1 + \sigma_3) \quad \text{for } \sigma_2 = 0$$

or: $$(\sigma_3-\sigma_1)^2 = 12T_o(\sigma_1+\sigma_3) \quad \text{for } \sigma_2 = \sigma_3$$

It follows from (A7) that $C_o = 12T_o$. The theory is in reasonable agreement with Murrell's experimental results for cleavage in brittle rocks (Murrell, 1963).

An analogy has been made, for the purpose of illustration, between fracture by cleavage and intergranular fracture. This is justified by their typically brittle natures, i.e. the limited amount of localized plastic flow which occurs in both cases. The method of calculation and the program for constructing the fracture surface was taken from Ashby and Embury (1981). It has been used for only two of the materials; the peak aged and the overaged Al 3.6% Cu. The fracture surface of the overaged material is an approximate representation since, as discussed, in the text, the fracture surface of the test piece possibly indicates a ductile fracture mechanism. The fracture of

pure Al and the solid solution of Al 3.6% Cu were both distinctly ductile in nature, and therefore were not included.

The fracture surface was calculated for plane stress and was included on the map illustrating the effects of change in strain path during plastic deformation. It was assumed that all loading of the sample was proportional and monotonic.

A second map was constructed, using the same criterion, for axisymmetry. This type of map is best suited for illustrating the mechanisms involved in fracture and how they interact. One might include on the same map the initial yield surface, the surface representing the initiation of void nucleation and the shear failure surface. Data from this study permit the construction of only the initial yield and final (brittle) fracture surfaces.

```
10  REM  ---------- ---------- ---------- ---------- ----------
11  REM  ***     PLANE  STRESS  FRACTURE  MAP        ***
12  REM  ----------------------MARCH  1981----------------------
20 D$ =  CHR$ (4)
50  REM  SELECT PRINTER PLOT (PL=1) OR MONITOR PLOT (PL=0)
51 PL  = 1
52  REM  SELECT THE RATIO OF S2  AT S1=0 TO S1 AT S2= BACK   STRESS.
53 P(1) = 1
54 P(2) = .857
60  REM  SELECT NUMBER OF CALCULATION STEPS
65 ST = 80
70  REM  SET THE FINAL STRESS VALUE AFTER THE PRESTRAIN IN THE A DIRE
     .
75 S.S = 320
78  REM  SET MAX STRESS FOR PLOT
79 SMAX = 500
80  REM  SET YIELD STRESSES (Y1). ALLOWED STRESS IN TENSION  (SS ) AN
     F BACK STRESS    (BS).
85 Y1(1) = 179
86 Y1(2) = 315
87 Y1(3) = 349
90 SS  = 0
91 BS(1) = 0
92 BS(2) = 34.5
100  DIM S1(ST,2),S2(ST,2),E1(ST,2),E2(ST,2)
140  PRINT
141  PRINT
150  PRINT "*****************************************"
151  PRINT "**                                     **"
152  PRINT "**      CHECK PLOTTING PARAMETERS      **"
153  PRINT "**                                     **"
154  PRINT "*****************************************"
155  PRINT
156  PRINT "PL  = "PL "      ST = "ST"      SMAX = "SMAX
160  PRINT
161  PRINT "INITIAL YIELD IN THE A DIRECTION:"Y1(1)
162  PRINT "FINAL  STRESS IN THE A DIRECTION:"FS
163  PRINT
164  PRINT "SUBSEQUENT YIELD IN THE B DIRECTION:"Y1(2)
165  PRINT
166  PRINT "P(1)="P(1)"     P(2)="P(2)
167  PRINT
168  PRINT "FRACTURE STRESS IN TENSION:"SS " MPA"
169  PRINT
170  PRINT "BACK STRESS DUE TO THE BF:"BS(2)" MPA"
171  PRINT
172  PRINT "*****************************************"
173  PRINT "**       IF NOT OK.  TYPE  RAD         **"
174  PRINT "**           THEN EDIT 50-90           **"
180  PRINT "*****************************************"
181  INPUT D$
182  IF D$ = "RAD" THEN  LIST 45,90
183  IF D$ = "RAD" THEN 490
```

```
200  REM  ------------------------------------------
201  REM                 MAIN  PROGRAM
202  REM  ------------------------------------------
230  FOR I = 1 TO ST
240 C = 0.28318 * I / ST
260 FTA =  TAN (C)
270 ALPHA =  SQR (1 - FTA + FTA * 2)
272  IF C > 1.570796 AND C < 4.712389 THEN ALPHA =  - ALPHA
275 BETA =  - (1 + FTA) / 3
300  REM  ------------------------------------------
301  REM              CALCULATIONS FOR YIELD
302  REM  ------------------------------------------
303  FOR J = 1 TO 2
305 S1(I,J) = Y1(J) / ALPHA
315 S3(I,J) = P(J) * FTA * S1(I,J)
350  REM  ------------------------------------------
351  REM              CALCULATIONS FOR CLEAVAGE
352  REM  ------------------------------------------
355 C1(I,J) = 36 * SCL  * BETA / (ALPHA * 2)
360 C3(I,J) = FTA * C1(I,J)
363  IF C1(I,J) >  - 5 * SCL  AND C3(I,J) > 0 THEN C3(I,J) = SCL
364  IF C3(I,J) >  - 5 * SCL  AND C1(I,J) > 0 THEN C1(I,J) = SCL
365  IF C1(I,J) > SCL  THEN C1(I,J) = SCL
370  IF C3(I,J) > SCL  THEN C3(I,J) = SCL
375  IF C > 0 AND C < 1.57 THEN C1(I,J) = SCL
380  IF C > 0 AND C < 1.57 THEN C3(I,J) = SCL
385  NEXT J
450  NEXT I
460  GOSUB 505
470  IF PL  > 0 THEN  GOSUB 853
490  END
501  REM  ------------------------------------------
502  REM        SUBROUTINE TO PLOT MAP
503  REM  ------------------------------------------
505  IF PL  > 0 THEN  PRINT D$:"PR#1"
506  PRINT
507  PRINT "-------------------------------------------------------------------
508  PRINT "*** PLANE STRESS MAP ***       MARCH 1981                    FRMAP1
509  PRINT "-------------------------------------------------------------------
510  PRINT
511  PRINT "YIELD STRESS IN THE A DIRECTION="Y1(1)
512  PRINT
513  PRINT "YIELD STRESS IN THE B DIRECTION="Y1(2)
514  PRINT
515  PRINT "YIELD STRESS IN THE C DIRECTION="Y1(3)
516  PRINT
517  PRINT "CLEAVAGE STRESS="SCL
518  PRINT
520  PRINT "STRESS AXIS RUNS FROM -"SMAX" TO "SMAX"      "ST" STEPS"
525  PRINT
526  PRINT
530  IF PL  > 0 THEN  PRINT D$:"PR#0"
```

```
540  PRINT
550  HGR2
560  HCOLOR= 3
570  HPLOT 139.0 TO 139.191
580  HPLOT 0.95 TO 279.95
590 A = 5
600  FOR I =  - A TO A
610  HPLOT 139 + 95 * I / A.93 TO 139 + 95 * I / A.97
620  HPLOT 137.95 * (1 + I / A) TO 141.95 * (1 + I / A)
625  NEXT I
627  FOR J = 1 TO 2
630 A0 = 139 + (Y1(J) / SMAX) * 95
631 B0 = 95
635 C0 = 139 - (12 * SCL / SMAX) * 95
636 D0 = 95
640  FOR I = 1 TO ST
650 A = 139 + (S1(I,J) / SMAX) * 95
660 B = 95 - (S3(I,J) / SMAX) * 95 + (BS(J) / SMAX) * 95
670  IF A < 0 THEN A = 0
680  IF B < 0 THEN B = 0
690  IF A > 279 THEN A = 279
700  IF B > 191 THEN B = 191
710  HPLOT (A + A0) / 2,(B + B0) / 2 TO A,B
715 A0 = A
716 B0 = B
750 C = 139 + (C1(I,J) / SMAX) * 95
752 D = 95 - (C3(I,J) / SMAX) * 95
754  IF C < 0 OR D < 0 OR C > 279 OR D > 191 THEN 895
762  HPLOT C,D
764 C0 = C
766 D0 = D
895  NEXT I
897  NEXT J
898  RETURN
950  REM  ------------------------------------------------------
951  REM    SUBROUTINE  FOR  PRINTER  PLOT
952  REM  ------------------------------------------------------
953  PRINT D$;"PR#1"
954  POKE  - 12524.0
956  POKE  - 12525.64
958  POKE  - 12529.255
960  POKE  - 12528.7
962  PRINT  CHR$ (17)
968  LIST 904 - 906
970  PRINT D$;"PR#0"
999  RETURN
```

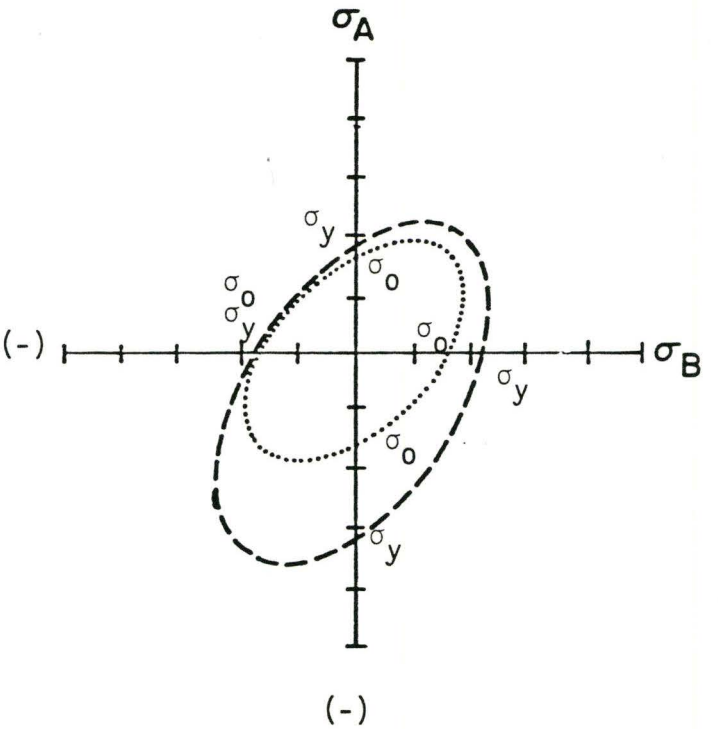

FIGURE A: Yield Surface Movement: Over Aged Al-Cu

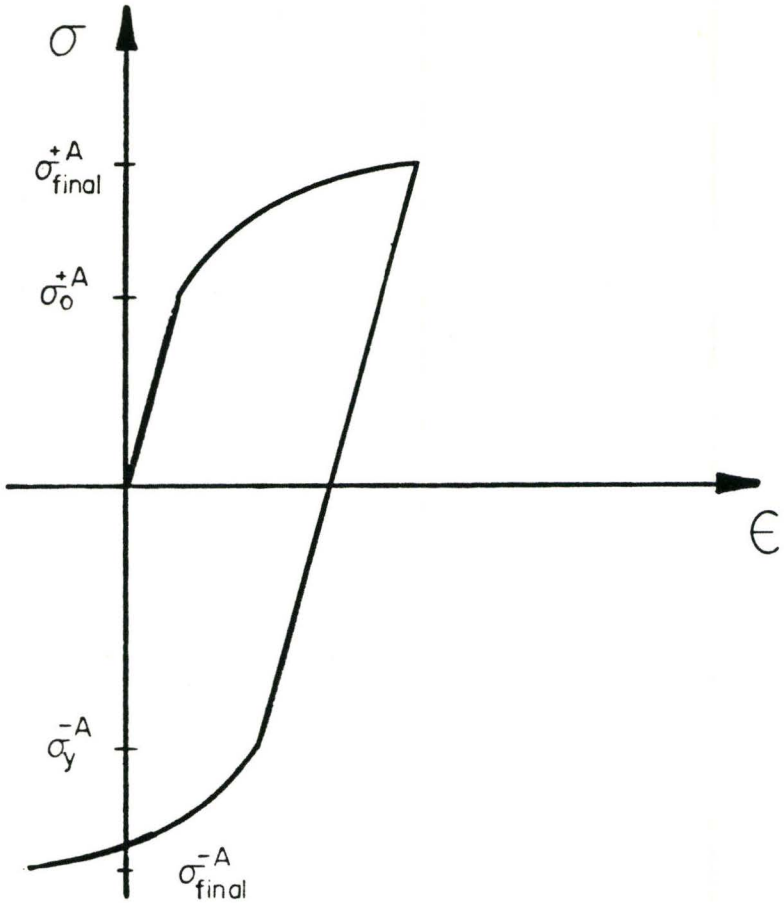

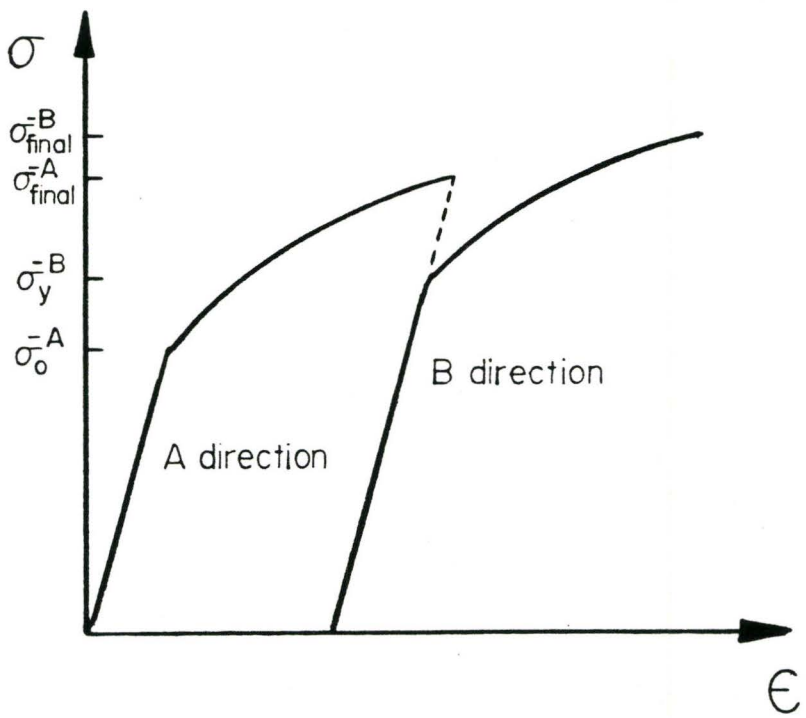

FIGURE B: Definition of Terms